

## **INFORMATION TO USERS**

This manuscript has been reproduced from the microfilm master. UMI films the text directly from the original or copy submitted. Thus, some thesis and dissertation copies are in typewriter face, while others may be from any type of computer printer.

**The quality of this reproduction is dependent upon the quality of the copy submitted.** Broken or indistinct print, colored or poor quality illustrations and photographs, print bleedthrough, substandard margins, and improper alignment can adversely affect reproduction.

In the unlikely event that the author did not send UMI a complete manuscript and there are missing pages, these will be noted. Also, if unauthorized copyright material had to be removed, a note will indicate the deletion.

Oversize materials (e.g., maps, drawings, charts) are reproduced by sectioning the original, beginning at the upper left-hand corner and continuing from left to right in equal sections with small overlaps.

Photographs included in the original manuscript have been reproduced xerographically in this copy. Higher quality 6" x 9" black and white photographic prints are available for any photographs or illustrations appearing in this copy for an additional charge. Contact UMI directly to order.

**Bell & Howell Information and Learning  
300 North Zeeb Road, Ann Arbor, MI 48106-1346 USA  
800-521-0600**

**UMI<sup>®</sup>**



**University of Alberta**

**Experimental determination of the elastic coefficients of  
anisotropic materials with the slant-stack method**

by

**Marko Mah**



A thesis submitted to the Faculty of Graduate Studies and Research in partial  
fulfillment of the requirements for the degree of Master of Science  
in  
Geophysics

**Department of Physics**

Edmonton, Alberta

Fall 1999



National Library  
of Canada

Acquisitions and  
Bibliographic Services

395 Wellington Street  
Ottawa ON K1A 0N4  
Canada

Bibliothèque nationale  
du Canada

Acquisitions et  
services bibliographiques

395, rue Wellington  
Ottawa ON K1A 0N4  
Canada

*Your file Votre référence*

*Our file Notre référence*

The author has granted a non-exclusive licence allowing the National Library of Canada to reproduce, loan, distribute or sell copies of this thesis in microform, paper or electronic formats.

The author retains ownership of the copyright in this thesis. Neither the thesis nor substantial extracts from it may be printed or otherwise reproduced without the author's permission.

L'auteur a accordé une licence non exclusive permettant à la Bibliothèque nationale du Canada de reproduire, prêter, distribuer ou vendre des copies de cette thèse sous la forme de microfiche/film, de reproduction sur papier ou sur format électronique.

L'auteur conserve la propriété du droit d'auteur qui protège cette thèse. Ni la thèse ni des extraits substantiels de celle-ci ne doivent être imprimés ou autrement reproduits sans son autorisation.

0-612-47063-6

**Canada**

**University of Alberta**

**Library Release Form**

NAME OF AUTHOR: Marko Mah

TITLE OF THESIS: Experimental determination of the elastic coefficients of anisotropic materials with the slant-stack method

DEGREE: Master of Science

YEAR THIS DEGREE GRANTED: 1999

Permission is hereby granted to the University of Alberta Library to reproduce single copies of this thesis and to lend or sell such copies for private, scholarly or scientific research purposes only.

The author reserves all other publication and other rights in association with the copyright in the thesis, and except as hereinbefore provided neither the thesis nor any substantial portion thereof may be printed or otherwise reproduced in any material form whatever without the author's prior written permission.



Marko Mah  
602 Avadh Bhatia Physics Building  
*University of Alberta*  
Edmonton, Alberta  
CANADA T6G 2J1  
mah@phys.ualberta.ca

September 20, 1999

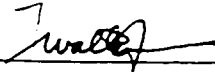
University of Alberta

Faculty of Graduate Studies and Research

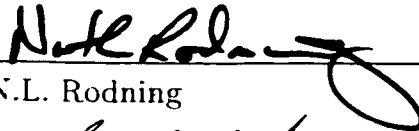
The undersigned certify that they have read, and recommend to the Faculty of Graduate Studies and Research for acceptance, a thesis entitled **Experimental determination of the elastic coefficients of anisotropic materials with the slant-stack method** submitted by **Marko Mah** in partial fulfillment of the requirements for the degree of Master of Science in Geophysics.



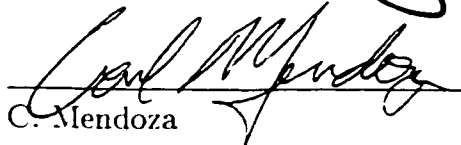
D.R. Schmitt (Supervisor)



W. Jones



N.L. Rodning



C. Mendoza

DATE: AUGUST 24, 1999

**Dedication**

To my father.

## Abstract

Through a combination of texture and porosity, the intrinsic anisotropy of many rocks is orthorhombic. Experimentally determining the nine required independent elastic coefficients for this case remains challenging and there remains room for new methodologies. Elastic coefficients are most often found from measurements of the phase-velocity in a variety of directions throughout a material. Finding this phase-velocity, which most simply corresponds to the propagation speed of a plane wave, is problematic. The  $\tau - p$  method is used to directly obtain quasi-P and quasi-S wave phase-speeds within a number of planes through a composite material of orthorhombic symmetry. Arrays of specially constructed transducers (0.65 MHz), designed to preferentially stimulate and receive the one q-P and two q-S propagation modes, were placed on a rectangular prism of the material. Over 680 individual measures of phase speed were obtained and subsequently used in a generalized least-squares inversion for the required elastic coefficients. Corresponding tests on isotropic soda-lime glass indicated that the coefficients can be determined with an uncertainty of 5 %.



## **Acknowledgements**

I would first like to thank Douglas Schmitt for his supervision, guidance, and support. During my stay at the University of Alberta, I have enjoyed the number of conversations that we have had together. I wish to thank R.H.A. David Shaw for his support and discussions during the course of this thesis. I would also like to thank the other graduate students in the Geophysics group who I've enjoyed collaborating and working with. I would also like to acknowledge the large amount of help that I have received from the Coffee Room people in the formatting of this thesis. I would like to recognize Irene Meglis, Roger Hunt, Len Tober, and Richard Tomski for their technical assistance and help. This work would have been more difficult without Drs. Kebaili and Molz whose work helped prepare the way for the present experiments. The assistance of the Alberta Microelectronics Centre in cutting of the ceramic transducers is greatly appreciated. I would also like to thank the many numerous people not already mentioned who have made my stay here more enjoyable. Needless to say, I would like to express my gratitude towards Lynn Chandler who has worked hard and tirelessly for the benefit of the graduate students in our department. I also appreciate the help of Adam Baig in the proof-reading of this thesis.

This work was supported by NSERC and the Petroleum Research Fund administered by the American Chemical Society. The use of the computer equipment and software of the Downhole Seismic Imaging Consortium during the preparation of this thesis is appreciated.

## Preface

The work presented in this thesis was carried out at the Department of Physics at the University of Alberta, Edmonton and at the Institute for Geophysical Research. The work was done under the supervision of Douglas R. Schmitt. Results from Chapter 2 have been submitted for publication in the following article:

- Mah. M., and Schmitt, D. R., Experimental determination of the elastic coefficients of anisotropic materials with the slant-stack method. Submitted to Geophysics in July 1999.

Some preliminary work from chapter 2 has been presented in conference and the corresponding abstract published in:

- Mah. M., and Schmitt, D. R., 1998. Velocity anisotropy determination with the  $\tau - p$  method: 68th Ann. Internat. Mtg., Soc. Expl. Geophys., Expanded Abstracts, 1000-1003.

# Table of Contents

<b>1</b>	<b>Introduction</b>	<b>1</b>
1.1	Background . . . . .	1
1.1.1	Sources of velocity anisotropy . . . . .	2
1.1.2	Methods of determining anisotropy . . . . .	4
1.1.3	Ambiguities in determining anisotropy . . . . .	6
1.2	Theory . . . . .	7
1.3	Relationship between stiffness and anisotropic velocities . . . . .	12
1.4	Radon transform . . . . .	17
<b>2</b>	<b>Determination of Elastic Coefficients</b>	<b>25</b>
2.1	Introduction . . . . .	25
2.2	Background . . . . .	26
2.2.1	Pulse Transmission and Elasticity . . . . .	26
2.2.2	Plane-wave Decomposition . . . . .	28
2.2.3	Experimental Method . . . . .	30
2.3	Results and Discussion . . . . .	33
2.3.1	Phase Velocities . . . . .	33
2.3.2	Inversion for Elastic Coefficients . . . . .	36
2.4	Conclusions . . . . .	40
<b>3</b>	<b>Conclusions</b>	<b>63</b>
3.1	Determination of phase velocities and the elastic coefficients . . . . .	63
3.2	Future Work . . . . .	64
<b>A</b>	<b>Results from the glass block.</b>	<b>68</b>
<b>B</b>	<b>Results from the phenolic block.</b>	<b>75</b>
B.1	x-z plane . . . . .	75
B.2	y-z plane . . . . .	82
B.3	xy-z plane . . . . .	89
B.4	x-y plane . . . . .	96

TABLE OF CONTENTS

<b>C</b>	<b>Radon transform and inversion</b>	<b>103</b>
C.1	Radon transform . . . . .	103
C.1.1	Computer program for $\tau - p$ transform . . . . .	104
C.2	Inversion . . . . .	111
C.2.1	Computer Programs for Inversion. . . . .	113
C.2.2	Testing of inversion program . . . . .	153

# List of Figures

1.1	Unit cube showing stress directions . . . . .	23
1.2	Unit cube showing relative faces. . . . .	24
2.1	Distinction between group and phase velocities. . . . .	48
2.2	Outline of phase velocity determination method. . . . .	49
2.3	Orientation of the principal directions of the phenolic block. . . . .	50
2.4	Ideal particle motions imparted and received by the transducers. . . . .	51
2.5	Observed amplitude versus time traces with offset on the glass block for various transducers. . . . .	52
2.6	The $\tau - p$ transform obtained by slant-stacking of Figure 2.5a. . . . .	53
2.7	Orientation of planes on the composite block. . . . .	54
2.8	The complete set of P-polarization results from the x-z plane. . . . .	55
2.9	Slownesses and phase velocities in the x-z plane. . . . .	56
2.10	Analysis of x-z plane SV mode arrivals. . . . .	57
2.11	Analysis of x-z plane SH mode arrivals. . . . .	58
2.12	Phase velocities versus propagation angle $\theta$ in the x-z plane. . . . .	59
2.13	Phase velocities versus propagation angle $\theta$ in the y-z plane. . . . .	60
2.14	Phase velocities versus propagation angle $\theta$ in the xy-z plane. . . . .	61
2.15	Phase velocities versus propagation angle $\theta$ in the x-y plane. . . . .	62
A.1	P-polarization results from a 2.0 cm depth source on the glass block. . . . .	69
A.2	P-polarization results from a 4.0 cm depth source on the glass block. . . . .	70
A.3	SV-polarization results from a 4.0 cm depth source on the glass block. . . . .	71
A.4	SV-polarization results from a 6.0 cm depth source on the glass block. . . . .	72
A.5	SH-polarization results from a 2.0 cm depth source on the glass block. . . . .	73
A.6	SH-polarization results from a 4.0 cm depth source on the glass block. . . . .	74
B.1	P-polarization results from a 2.0 cm depth source on the phenolic block in the x-z plane. . . . .	76

## LIST OF FIGURES

B.2	P-polarization results from a 4.0 cm depth source on the phenolic block in the x-z plane. . . . .	77
B.3	SV-polarization results from a 4.0 cm depth source on the phenolic block in the x-z plane. . . . .	78
B.4	SV-polarization results from a 6.0 cm depth source on the phenolic block in the x-z plane. . . . .	79
B.5	SH-polarization results from a 2.0 cm depth source on the phenolic block in the x-z plane. . . . .	80
B.6	SH-polarization results from a 4.0 cm depth source on the phenolic block in the x-z plane. . . . .	81
B.7	P-polarization results from a 2.0 cm depth source on the phenolic block in the y-z plane. . . . .	83
B.8	P-polarization results from a 4.0 cm depth source on the phenolic block in the y-z plane. . . . .	84
B.9	SV-polarization results from a 4.0 cm depth source on the phenolic block in the y-z plane. . . . .	85
B.10	SV-polarization results from a 6.0 cm depth source on the phenolic block in the y-z plane. . . . .	86
B.11	SH-polarization results from a 2.0 cm depth source on the phenolic block in the y-z plane. . . . .	87
B.12	SH-polarization results from a 4.0 cm depth source on the phenolic block in the y-z plane. . . . .	88
B.13	P-polarization results from a 2.0 cm depth source on the phenolic block in the xy-z plane. . . . .	90
B.14	P-polarization results from a 4.0 cm depth source on the phenolic block in the xy-z plane. . . . .	91
B.15	SV-polarization results from a 4.0 cm depth source on the phenolic block in the xy-z plane. . . . .	92
B.16	SV-polarization results from a 6.0 cm depth source on the phenolic block in the xy-z plane. . . . .	93
B.17	SH-polarization results from a 2.0 cm depth source on the phenolic block in the xy-z plane. . . . .	94
B.18	SH-polarization results from a 4.0 cm depth source on the phenolic block in the xy-z plane. . . . .	95
B.19	P-polarization results from a 2.0 cm depth source on the phenolic block in the x-y plane. . . . .	97
B.20	P-polarization results from a 4.0 cm depth source on the phenolic block in the x-y plane. . . . .	98
B.21	SV-polarization results from a 4.0 cm depth source on the phenolic block in the x-y plane. . . . .	99

*LIST OF FIGURES*

B.22 SV-polarization results from a 6.0 cm depth source on the phenolic block in the x-y plane. . . . .	100
B.23 SH-polarization results from a 2.0 cm depth source on the phenolic block in the x-y plane. . . . .	101
B.24 SH-polarization results from a 4.0 cm depth source on the phenolic block in the x-y plane. . . . .	102
C.1 Inversion residuals on data acquired on a glass block. . . . .	164
C.2 Inversion residuals on data acquired on a phenolic block. . . . .	165

# List of Tables

2.1	Elastic constants of the stress-strain tensor for a sample of the orthorhombic material phenolic. . . . .	43
C.1	Inverted elastic constants for an isotropic material as noise is added.	156
C.2	Inverted elastic constants for an orthorhombic material with 0 % noise added. . . . .	156
C.3	Inverted elastic constants for an orthorhombic material with 1 % noise added. . . . .	157
C.4	Inverted elastic constants for an orthorhombic material with 2 % noise added. . . . .	157
C.5	Inverted elastic constants for an orthorhombic material with 3 % noise added. . . . .	158
C.6	Inverted elastic constants for an orthorhombic material with 4 % noise added. . . . .	158
C.7	Inverted elastic constants for an orthorhombic material with 5 % noise added. . . . .	159
C.8	Inverted elastic constants for an orthorhombic material with 6 % noise added. . . . .	160
C.9	Inverted elastic constants for an orthorhombic material with 7 % noise added. . . . .	160
C.10	Inverted elastic constants for an orthorhombic material with 8 % noise added. . . . .	161
C.11	Inverted elastic constants for an orthorhombic material with 9 % noise added. . . . .	161
C.12	Inverted elastic constants for an orthorhombic material with 10 % noise added. . . . .	162



# Chapter 1

## Introduction

### 1.1 Background

It is well known that most rocks are anisotropic to some degree. Despite this fact velocity isotropy remains the usual assumption in conventional seismic reflection and rock physics analyses. This velocity anisotropy may be the result of preferential orientation of mineral grains, the presence of orientated cracks of various sizes, or the occurrence of thin layering. Neglecting to incorporate anisotropy leads to incorrect seismic analyses and the introduction of error. However, our understanding of the anisotropic properties of many sedimentary rocks is limited and this ignorance hinders application of more realistic seismic investigations.

Given that our increased capacity to acquire seismic data allows for greater spatial resolution required for subtle stratigraphic and production related geophysics, it is of increasing importance that the intrinsic properties of the materials through which the seismic waves pass are better understood. In particular, a more complete elastic description of the materials forming the earth is required. Many workers have attempted to do this previously, but obtaining sufficient information on the anisotropy of rocks can be prohibitively costly. In this thesis, I describe and test a new methodology which will make determination of the complete set of elastic constants more practical.

### 1.1.1 Sources of velocity anisotropy

As mentioned before, anisotropy in rocks can be caused by a number of different factors and only a few will be reviewed briefly here. In sedimentary rocks such as shales, the presence of kerogen (the organic material from which oil is derived) causes anisotropy which is detectable by the transmission of both compressional and shear waves (Vernik & Nur, 1992). As the organic-rich shales are compacted over time, the kerogen forms thin bedding parallel laminations that may be observed in back-scatter SEM images. It was found that these thin laminae induce a strong velocity anisotropy in the samples taken. In carbonate-bearing deep-sea sediments the presence of oriented calcite, a highly anisotropic mineral, gives rise to transverse isotropy in the rocks (Carlson et al., 1984).

Seismic anisotropy is also observed in shallow crustal rocks and in the uppermost mantle (Kawasaki & Konno, 1984; Brocher & Christensen, 1990; Levin et al., 1996). In the mantle, anisotropy is thought to be caused by the systematic orientations of olivine and pyroxenes. The alignment of olivine grains is thought to occur during the process of deformation which produces preferential crystallographic crystal alignment (Christensen & Salisbury, 1979) and manifests itself in the form of significant teleseismic compression and shear wave travel time anomalies (Levin et al., 1996). Due to the distribution of mineral grains, azimuthal anisotropy occurs. This azimuthal anisotropy is observed also in the uppermost mantle from Rayleigh and Love waves. The correlation between seismic anisotropy and preferred mineral orientation is supported by the comparison of seismic reflection data with laboratory measurements on cores taken from the study area (e.g., Christensen & Salisbury, 1979).

Laboratory measurements of ultrasonic wave velocities in most rock samples demonstrate that velocity increases with confining pressure. This effect is attributed to the closure of microcracks with increasing pressure (Sayers, 1988;

Vernik & Nur, 1992; Vernik 1993; Johnston & Christensen, 1995). These cracks may be formed due to overpressuring in the process of oil and gas generation (Vernik, 1993), by jointing within the regional stress fields (Schoenberg & Helbig, 1997) or by drilling induced damage (Li & Schmitt, 1998). If the cracks are preferentially aligned, some forms of anisotropic symmetry are produced. For example, introduction of a vertical crack set into a horizontally layered medium will result in three planes of symmetry and produce orthorhombic anisotropy. Indeed, observed azimuthal variations in the ratio of arrival times of shear and compressional waves (P-wave) and shear wave (S-wave) birefringence (splitting) from large earthquakes have been taken as evidence of such cracks in the crust (Crampin, 1978).

It has long been known that the ratio of the wavelength of the wave propagating through the medium to the thickness of the layers through which it is passing can have a noticeable effect (Backus, 1962; Levin, 1979; Helbig, 1981; Helbig, 1984; Melia & Carlson, 1984; Carcione et al., 1991; Hornby et al., 1994; Marion et al., 1994; Hovem, 1995). This layering induced effect is manifest in the form of transverse isotropy with a rotational axis of symmetry perpendicular to layering (Backus, 1962; Helbig, 1981; Helbig, 1984; Melia & Carlson, 1984). The existence of such anisotropy was known prior to Backus' (1962) theoretical study and has been confirmed experimentally by Melia & Carlson (1984) who measured the P-wave velocity both perpendicular and parallel to the layering. These experiments showed that differing layers of isotropic homogeneous materials can create an anisotropic medium. This result is supported by vertical seismic profiles (VSP) which show a velocity variation with angle of propagation through a layered geology (Ricker, 1953; Uhrig & Mettle, 1995; Kebaili & Schmitt, 1996).

### 1.1.2 Methods of determining anisotropy

There have been many previous attempts at determining the anisotropy of various materials. Use of ultrasonic methods of measuring compressional and shear elastic wave velocities has been the preferred method. One of the earlier attempts at determining the anisotropy of a material was by Markham (1957) who determined the elastic constants of various metals of cubic and hexagonal crystal symmetry through the use of the pulse transmission method. Simply, in the pulse transmission method the travel time of a disturbance transmitted through a known thickness of the sample is measured in order to provide the velocity.

Due to their increasing importance in manufacturing, the anisotropy of artificial composite materials has also been well studied. Okoye et al. (1996) studied a composite consisting of layers of paper and epoxy called phenolite. This layered material should be transversely isotropic. Okoye et al. (1996) measured 96 P-wave velocities in a direct pulse transmission experiment where the source transducer was centrally positioned while the receiver was moved along a profile centered over the source transducer. Okoye et al. (1996) also developed an inversion procedure to convert the velocities to elastic constants under the assumption of transverse isotropy.

Another well studied artificial composite material is phenolic composed of layers of fibre mats in epoxy. This material is similar to phenolite but has an orthorhombic symmetry. Phenolic has been studied by Cheadle et al. (1991), Vestrum (1994), and Kebaili & Schmitt (1997). Cheadle et al. (1991) used the pulse transmission technique on a specially machined prism of phenolic in order to obtain group velocities. Vestrum (1994) took a different approach of measuring both group and phase velocities on a sphere and cube of phenolic respectively. These measurements were used in separate inversions to the elastic constants of the stress-strain tensor, which compared well with each other. Kebaili &

Schmitt (1997) took a more indirect approach by obtaining a series of miniature seismograms on a block of phenolic then converting these data to the  $\tau-p$  domain using a Radon transform from which plane wave velocities were directly found. A slant-stack (Radon) transform is a mapping of a two-dimensional function  $f(x, t)$  from the offset-time  $(x, t)$  domain into the intercept time-horizontal slowness  $(\tau - p)$  domain. The slant stack (Radon) transform is defined by Robinson (1982) and Tatham (1984):

$$F(\tau, p) = \int_{-\infty}^{\infty} f(x, \tau + px) dx \quad (1.1)$$

where  $F$  is the integration of the amplitudes  $f(x, t)$  along the line  $y = \tau + px$ . As only P-wave or compressional wave phase velocities were obtained, these could not be inverted to obtain the elastic constants.

Naturally occurring rock has also been studied. One of the earliest studies was that of Kaarsberg(1959) where seismic travel time and x-ray measurements were done on sediments and shales. Kaarsberg (1959) found that the velocities both parallel and perpendicular to the bedding increase with density. This increase may be caused by preferred orientation of the basal planes of clay minerals parallel to bedding. Another study, which involved cores being taken at various angles to the axis of symmetry of some shales, is that of Johnston & Christensen (1995). Using the pulse transmission technique, the phenomenon of shear wave splitting was observed and phase velocities were measured. Through the use of phase velocity measurements, the elastic constants of the rocks were determined. Vernik & Nur (1992) and Hornby (1995) similarly measured P-wave and S-wave velocities taken in cores parallel, perpendicular, and at 45 degrees to bedding and determined the elastic constants of the rocks with pressure.

Arts et al. (1991) and Arts (1993) measured P and S wave velocities on specially machined cubes of marble and limestone using a method very similar to

the one theoretically described by van Buskirk et al. (1986). Large piezoelectric transducers measured phase velocities for both P and S waves. An advantage of the method used is that no *a priori* knowledge of the symmetry or orientation of the material is required.

### 1.1.3 Ambiguities in determining anisotropy

A problem encountered is whether group or phase velocities are being measured. Briefly, phase velocities are associated with the propagation speed of a hypothetical plane wave through the material. Group, or ray, velocities are associated with the path of the energy flow from the source to the receiver. This will be discussed in more detail in Chapter 2. Phase velocities are usually needed for inversion back to the elastic constants. In an anisotropic medium, group velocity is not necessarily equal to phase velocity. Velocities taken in directions that are neither parallel nor perpendicular to axes of symmetry may be neither group nor phase velocities. Typically, group velocities are measured from a point source to a point receiver. Experimentally, sources and receivers are of finite size calling into doubt whether group velocities are truly being measured. Similarly, phase velocities are made from plane wave sources to plane wave receivers. Typically, this is difficult to achieve in experiments and may yield velocities which are not phase velocities. In many cases it may be difficult to know what type of velocities are being measured.

Dellinger & Vernik (1994) have attempted to address this issue. They found that rock cores that were neither parallel nor perpendicular to symmetry axes yielded apparent velocities which were lower than phase velocities but greater than group velocities. Dellinger & Vernik (1994) showed that in order to measure phase velocities in cores, the ratio of the height of the core to the transducer width must be less than 3 and to measure group velocities the ratio must be greater

than 20. So long as these rules of thumb are followed, one can be reasonably certain of the type of measurement being taken. Another example is the work of Hornby (1996). Cores were cut parallel, perpendicular and at off-axis angles to the symmetry of a shale. At off-axis angles, not only are the cores difficult to acquire and require *a priori* knowledge of symmetry axes but the velocities measured may be neither group nor phase. This ambiguity may lead to large and unquantifiable errors in the determination of the critically important parameters that control the wave shape away from the axes of symmetry. According to Dellinger & Vernik (1994) and Kebaili & Schmitt (1997), in order to obtain direct phase velocity measurements, large transducers must be used relative to sample size. This constraint limits the number of phase velocity measurements that can be practically taken, which are necessary to determine the elastic constants of the material. One method of addressing this problem is described by Kebaili & Schmitt (1997). They used a Radon transformation to put a series of  $x - t$  arrivals into the  $\tau - p$  domain. The shape of this arrival curve in the  $\tau - p$  domain contains substantial information on the anisotropy of the medium, as the phase velocities are obtained as a function of the direction of propagation.

In this thesis, the methodology described by Kebaili & Schmitt (1997) is extended and improved with the development of shear wave transducers. Phase velocity measurements are made on the orthorhombic medium phenolic for a number of different orientations and an inversion to the elastic constants of the material is performed.

## 1.2 Theory

The following is a brief summary of the mathematical work and a more complete description can be found in Lay & Wallace (1995) and Musgrave (1970). It is important to discuss the underlying theory of elasticity as it applies to elastic

wave anisotropy.

To begin, the stress is related to strain by the stress-strain relationship which is given by the generalized Hooke's Law where the Einstein summation convention will be used:

$$\sigma_{ij} = c_{ijkl}\epsilon_{kl} \quad (1.2)$$

where

$$i = 1, 2, 3:$$

$$j = 1, 2, 3:$$

$$k = 1, 2, 3:$$

$$l = 1, 2, 3:$$

$\sigma_{ij}$  is the second order stress tensor,

$\epsilon_{kl}$  is the second order strain tensor, and

$c_{ijkl}$  is the fourth rank elasticity tensor with components of stiffness.

Since the elasticity tensor  $c_{ijkl}$  has 4 indices, each of which goes from 1 to 3, the elasticity tensor has 81 elements present.

If one takes the unit cube as an example then  $\sigma_{ij}$  is the stress or pressure on the  $i^{th}$  face in the  $x_j$  direction as shown in Figure 1.1. The  $i^{th}$  face is the face on the unit cube whose outward normal is parallel to  $x_i$  direction as can be seen in Figure 1.2. For convenience, in chapter 2  $x$ ,  $y$ , and  $z$  will be used for  $x_1$ ,  $x_2$ , and  $x_3$  respectively.

The strain  $\epsilon_{kl}$  is defined in a similar manner to the stress  $\sigma_{ij}$ . The strain  $\epsilon_{kl}$  is the strain on the  $k^{th}$  surface in the  $x_l$  direction and will be defined by the following formula (Lay & Wallace, 1995) as:

$$\epsilon_{kl} = \frac{1}{2} \left( \frac{\partial U_k}{\partial x_l} + \frac{\partial U_l}{\partial x_k} \right) \quad (1.3)$$



where  $U_k$  is the displacement in the  $x_k$  direction.

A closer look at  $\epsilon_{11}$ ,  $\epsilon_{22}$ , and  $\epsilon_{33}$  shows that these strains are distortions in the size of the unit cube.

$$\text{These are strains normal to the surface.} \quad \left( \begin{array}{l} \epsilon_{11} = \frac{\partial U_1}{\partial x_1} \text{ which is an elongation of} \\ \text{the unit cube in the } x_1 \text{ direction} \\ \epsilon_{22} = \frac{\partial U_2}{\partial x_2} \text{ which is an elongation of} \\ \text{the unit cube in the } x_2 \text{ direction} \\ \epsilon_{33} = \frac{\partial U_3}{\partial x_3} \text{ which is an elongation of} \\ \text{the unit cube in the } x_3 \text{ direction} \end{array} \right.$$

(i.e. compression or elongation)

A closer look at  $\epsilon_{12}$ ,  $\epsilon_{13}$ , and  $\epsilon_{23}$  shows that these are distortions in the shape of the unit cube.

$$\text{These are strains parallel} \quad \left( \begin{array}{l} \epsilon_{12} = \frac{1}{2} \left( \frac{\partial U_1}{\partial x_2} + \frac{\partial U_2}{\partial x_1} \right) \text{ is the shearing on surface 1} \\ \text{in the } x_2 \text{ direction} \\ \epsilon_{13} = \frac{1}{2} \left( \frac{\partial U_1}{\partial x_3} + \frac{\partial U_3}{\partial x_1} \right) \text{ is the shearing on surface 1} \\ \text{in the } x_3 \text{ direction} \\ \epsilon_{23} = \frac{1}{2} \left( \frac{\partial U_2}{\partial x_3} + \frac{\partial U_3}{\partial x_2} \right) \text{ is the shearing on surface 2} \\ \text{in the } x_3 \text{ direction} \end{array} \right.$$

to the surface.(i.e. shear)

As can be easily seen from Equation 1.3,  $\epsilon_{kl}$  is equal to  $\epsilon_{lk}$ . (i.e.,  $\epsilon_{12}=\epsilon_{21}$  and so forth.) This symmetry implies:

$$c_{ijkl} = c_{ijlk} . \quad (1.4)$$

A similar symmetry exists for the stress tensor as well where  $\sigma_{ij}$  is equal to  $\sigma_{ji}$ . This symmetry of stresses implies:

$$c_{ijkl} = c_{jikl} . \quad (1.5)$$

Using the symmetries in the stress and strain tensors reduces the 81 element stress-strain tensor  $c_{ijkl}$  to only 36 independent elements.

Arguments of symmetry and thermodynamics (i.e., internal energy of the material must increase with a strain) reduces from 81 to 21 the components of stiffness (Musgrave, 1970). For the sake of convenience, the  $c_{ijkl}$  stiffness tensor can be represented as a symmetric 6 x 6 matrix  $C_{mn}$ .

The stiffness  $c_{ijkl}$  can be transformed to  $C_{mn}$  according to the rule (Vestrum, 1994):

$$m = \begin{cases} i & \text{if } i=j \\ 9 - (i + j) & \text{if } i \neq j \end{cases} \text{ and} \quad (1.6)$$

$$n = \begin{cases} k & \text{if } k=l \\ 9 - (k + l) & \text{if } k \neq l \end{cases} \quad (1.7)$$

Using this formula translates the generalized Hooke's Law from  $\sigma_{ij} = c_{ijkl}\epsilon_{kl}$  to the following form:

$$\begin{bmatrix} \sigma_{11} \\ \sigma_{22} \\ \sigma_{33} \\ \sigma_{23} \\ \sigma_{13} \\ \sigma_{12} \end{bmatrix} = \begin{bmatrix} C_{11} & C_{12} & C_{13} & C_{14} & C_{15} & C_{16} \\ C_{21} & C_{22} & C_{23} & C_{24} & C_{25} & C_{26} \\ C_{31} & C_{32} & C_{33} & C_{34} & C_{35} & C_{36} \\ C_{41} & C_{42} & C_{43} & C_{44} & C_{45} & C_{46} \\ C_{51} & C_{52} & C_{53} & C_{54} & C_{55} & C_{56} \\ C_{61} & C_{62} & C_{63} & C_{64} & C_{65} & C_{66} \end{bmatrix} \begin{bmatrix} \epsilon_{11} \\ \epsilon_{22} \\ \epsilon_{33} \\ 2\epsilon_{23} \\ 2\epsilon_{13} \\ 2\epsilon_{12} \end{bmatrix} \quad (1.8)$$

where  $C_{mn} = C_{nm}$  and by examination it may be noted that only 21 independent stiffnesses exist. However, this is the most general case where there is no symmetry. It is useful to examine briefly how the elastic tensor  $C_{mn}$  appears with increasing symmetry.

For isotropic symmetry there are 2 independent constants given as the Lamé's parameter  $\lambda$  and  $\mu$  (Musgrave, 1970) such that:

$$C_{ij} = \begin{vmatrix} \lambda + 2\mu & \lambda & \lambda & 0 & 0 & 0 \\ \lambda & \lambda + 2\mu & \lambda & 0 & 0 & 0 \\ \lambda & \lambda & \lambda + 2\mu & 0 & 0 & 0 \\ 0 & 0 & 0 & \mu & 0 & 0 \\ 0 & 0 & 0 & 0 & \mu & 0 \\ 0 & 0 & 0 & 0 & 0 & \mu \end{vmatrix} \quad (1.9)$$

Materials of cubic symmetry have 3 independent constants (Musgrave, 1970):

$$C_{ij} = \begin{vmatrix} a & b & b & 0 & 0 & 0 \\ b & a & b & 0 & 0 & 0 \\ b & b & a & 0 & 0 & 0 \\ 0 & 0 & 0 & c & 0 & 0 \\ 0 & 0 & 0 & 0 & c & 0 \\ 0 & 0 & 0 & 0 & 0 & c \end{vmatrix}. \quad (1.10)$$

For hexagonal symmetry (transverse isotropy) 5 independent constants are required (Musgrave, 1970).

$$C_{ij} = \begin{vmatrix} a & b & c & 0 & 0 & 0 \\ b & a & c & 0 & 0 & 0 \\ c & c & d & 0 & 0 & 0 \\ 0 & 0 & 0 & e & 0 & 0 \\ 0 & 0 & 0 & 0 & e & 0 \\ 0 & 0 & 0 & 0 & 0 & x \end{vmatrix} \quad (1.11)$$

where  $x = \frac{a-b}{2}$ .

Orthorhombic symmetry is characterized by 3 mutually orthogonal planes of symmetry and 9 independent elastic constants (Musgrave, 1970).

$$C_{ij} = \begin{vmatrix} a & b & c & 0 & 0 & 0 \\ b & d & e & 0 & 0 & 0 \\ c & e & f & 0 & 0 & 0 \\ 0 & 0 & 0 & g & 0 & 0 \\ 0 & 0 & 0 & 0 & h & 0 \\ 0 & 0 & 0 & 0 & 0 & i \end{vmatrix} \quad (1.12)$$

In contrast to the previous cases, if no symmetry is present the material is treated as triclinic which is characterized by 21 independent elastic constants (Musgrave, 1970).

$$C_{ij} = \begin{vmatrix} a & b & c & d & e & f \\ b & g & h & i & j & k \\ c & h & l & m & n & o \\ d & i & m & p & q & r \\ e & j & n & q & s & t \\ f & k & o & r & t & u \end{vmatrix} \quad (1.13)$$

For a variety of reasons, one might expect the symmetry of many rocks to be rather low, with orthorhombic symmetry being that of the highest symmetry. However in natural crystals less symmetry can exist, as in the cases of calcite and plagioclase feldspar in order of decreasing symmetry and requiring an increasing number of elastic constants of 7 and 21, respectively.

Determining the stiffness tensor directly by actually applying large pressures and shears to the sample and determining the infinitesimal compressions can be difficult. Instead, it is often simpler to determine these properties indirectly by measuring the elastic wave velocities and densities of the material.

### 1.3 Relationship between stiffness and anisotropic velocities

Newton's second law states that the sum of the forces applied to the unit cube will be equal to the mass times the acceleration. In other words, the mass multiplied by the acceleration in the  $x_i$  direction is equal to the sum of the forces in the  $x_i$  direction:

$$\vec{F} = m \vec{a} \quad (1.14)$$

Take for example in the  $x_1$  direction  $\sum F_{x_1} = ma_{x_1} = m\ddot{U}_1$ .

$$\begin{aligned} \sum F_{x_1} &= \left[ \sigma_{11} - \left( \sigma_{11} + \frac{\partial \sigma_{11}}{\partial x_1} (-\Delta x_1) \right) \right] \Delta x_2 \Delta x_3 \\ &+ \left[ \sigma_{21} - \left( \sigma_{21} + \frac{\partial \sigma_{21}}{\partial x_2} (-\Delta x_2) \right) \right] \Delta x_1 \Delta x_3 \\ &+ \left[ \sigma_{31} - \left( \sigma_{31} + \frac{\partial \sigma_{31}}{\partial x_3} (-\Delta x_3) \right) \right] \Delta x_1 \Delta x_2 \end{aligned} \quad (1.15)$$

This equation simplifies to the following:

$$\begin{aligned} \sum F_{x_1} &= \left( \frac{\partial \sigma_{11}}{\partial x_1} + \frac{\partial \sigma_{21}}{\partial x_2} + \frac{\partial \sigma_{31}}{\partial x_3} \right) \Delta x_1 \Delta x_2 \Delta x_3 \\ &= \left[ \frac{\partial (c_{11kl} \epsilon_{kl})}{\partial x_1} + \frac{\partial (c_{21kl} \epsilon_{kl})}{\partial x_2} + \frac{\partial (c_{31kl} \epsilon_{kl})}{\partial x_3} \right] \Delta x_1 \Delta x_2 \Delta x_3 \end{aligned} \quad (1.16)$$

But  $\frac{\partial c_{ijkl}}{\partial x_m} = 0$  for  $m=1,2,3$  since the material is assumed to be homogeneous and the elastic constants cannot change with position.

This means:

$$\sum F_{x_1} = \left[ c_{11kl} \frac{\partial \epsilon_{kl}}{\partial x_1} + c_{21kl} \frac{\partial \epsilon_{kl}}{\partial x_2} + c_{31kl} \frac{\partial \epsilon_{kl}}{\partial x_3} \right] \Delta x_1 \Delta x_2 \Delta x_3 . \quad (1.17)$$

However,

$$\sum F_{x_1} = m\ddot{U}_1 = \rho \Delta x_1 \Delta x_2 \Delta x_3 \ddot{U}_1 \quad (1.18)$$

where  $\rho$  is the density for the unit cube.

When Equation 1.17 and Equation 1.18 are combined, one obtains the following:

$$\rho \Delta x_1 \Delta x_2 \Delta x_3 \ddot{U}_1 = c_{i1kl} \epsilon_{kl,i} \Delta x_1 \Delta x_2 \Delta x_3 \quad (1.19)$$

which can be simplified to:

$$\rho \ddot{U}_i = c_{ijkl} \epsilon_{kl,j} . \quad (1.20)$$

But, as defined before:

$$\begin{aligned} \epsilon_{kl} &= \frac{1}{2} \left( \frac{\partial U_k}{\partial x_l} + \frac{\partial U_l}{\partial x_k} \right) \\ &= \frac{1}{2} (U_{k,l} + U_{l,k}) . \end{aligned} \quad (1.21)$$

which implies:

$$\begin{aligned} \epsilon_{kl,j} &= \frac{1}{2} \left( \frac{\partial^2 U_k}{\partial x_l \partial x_j} + \frac{\partial^2 U_l}{\partial x_k \partial x_j} \right) \\ &= \frac{1}{2} (U_{k,lj} + U_{l,kj}) . \end{aligned} \quad (1.22)$$

So, when Equation 1.22 is substituted into Equation 1.20, one obtains the following:

$$\begin{aligned} \rho \ddot{U}_i &= c_{ijkl} \left( \frac{1}{2} (U_{k,lj} + U_{l,kj}) \right) \\ &= \frac{1}{2} (c_{ijkl} U_{k,lj} + c_{ijkl} U_{l,kj}) \\ &= c_{ijkl} U_{l,jk} . \end{aligned} \quad (1.23)$$

Due to the simplicity of using plane waves, if one assumes that the plane wave solutions to this equation are of the form:

$$U_i = A_i e^{i \frac{2\pi}{\lambda} (n_r x_r - \nu t)} \quad (1.24)$$

where  $\nu$  is the phase velocity,  $\vec{n} = (n_1, n_2, n_3)$  is the wave front normal,  $\vec{A} = (A_1, A_2, A_3)$  is the amplitude vector, and  $\vec{x} = (x_1, x_2, x_3)$  is the position vector.

From this ansatz

$$\dot{U}_i = \left( -\nu \left( i \frac{2\pi}{\lambda} \right) \right) A_i e^{i \frac{2\pi}{\lambda} (n_r x_r - \nu t)} \quad (1.25)$$

and

$$\begin{aligned}\ddot{U}_i &= \left(-\nu \left(i \frac{2\pi}{\lambda}\right)\right)^2 A_i e^{i \frac{2\pi}{\lambda}(n_r x_r - \nu t)} \\ &= -\left(\nu \frac{2\pi}{\lambda}\right)^2 A_i e^{i \frac{2\pi}{\lambda}(n_r x_r - \nu t)} .\end{aligned}\quad (1.26)$$

Similarly,

$$U_l = A_l e^{i \frac{2\pi}{\lambda}(n_r x_r - \nu t)} .\quad (1.27)$$

$$U_{l,j} = i \frac{2\pi}{\lambda} n_j A_l e^{i \frac{2\pi}{\lambda}(n_r x_r - \nu t)} , \text{ and}\quad (1.28)$$

$$\begin{aligned}U_{l,jk} &= \left(i \frac{2\pi}{\lambda}\right)^2 n_j n_k A_l e^{i \frac{2\pi}{\lambda}(n_r x_r - \nu t)} \\ &= -\left(\frac{2\pi}{\lambda}\right)^2 n_j n_k A_l e^{i \frac{2\pi}{\lambda}(n_r x_r - \nu t)} .\end{aligned}\quad (1.29)$$

When Equation 1.26 and Equation 1.29 are substituted in Equation 1.23 one gets the following:

$$-\rho \left(\nu \frac{2\pi}{\lambda}\right)^2 A_i e^{i \frac{2\pi}{\lambda}(n_r x_r - \nu t)} = -c_{ijkl} \left(\frac{2\pi}{\lambda}\right)^2 n_j n_k A_l e^{i \frac{2\pi}{\lambda}(n_r x_r - \nu t)}\quad (1.30)$$

Equation 1.30 simplifies to:

$$\rho \nu^2 A_i = c_{ijkl} n_j n_k A_l\quad (1.31)$$

The following substitution  $\Gamma_{il} = c_{ijkl} n_j n_k$  is used where  $\Gamma_{il}$  are the Christoffel equations (Musgrave, 1970). When this substitution is made into Equation 1.31 one obtains the following:

$$\rho\nu^2 A_i = \Gamma_{il} A_l \quad (1.32)$$

which implies

$$(\Gamma_{il} - \rho\nu^2 \delta_{il}) A_l = 0 . \quad (1.33)$$

When written in matrix form, this equation is an eigenvalue problem,  $Bx = \lambda x$ , where the eigenvalues and eigenvectors of the system are equivalent to the phase velocities and amplitude vectors respectively:

$$\begin{bmatrix} \Gamma_{11} & \Gamma_{12} & \Gamma_{13} \\ \Gamma_{21} & \Gamma_{22} & \Gamma_{23} \\ \Gamma_{31} & \Gamma_{32} & \Gamma_{33} \end{bmatrix} \begin{bmatrix} A_1 \\ A_2 \\ A_3 \end{bmatrix} = \rho\nu^2 \begin{bmatrix} A_1 \\ A_2 \\ A_3 \end{bmatrix} . \quad (1.34)$$

For example, the case of the orthorhombic medium has the following 2-dimensional stiffness matrix:

$$C_{ij} = \begin{vmatrix} a & b & c & 0 & 0 & 0 \\ b & d & e & 0 & 0 & 0 \\ c & e & f & 0 & 0 & 0 \\ 0 & 0 & 0 & g & 0 & 0 \\ 0 & 0 & 0 & 0 & h & 0 \\ 0 & 0 & 0 & 0 & 0 & i \end{vmatrix}$$

where the letters a through i represent the 9 independent elastic constants.

For the direction  $\vec{n} = (1, 0, 0)$  Equation 1.34 becomes:

$$\begin{bmatrix} a & 0 & 0 \\ 0 & i & 0 \\ 0 & 0 & h \end{bmatrix} \begin{bmatrix} A_1 \\ A_2 \\ A_3 \end{bmatrix} = \rho\nu^2 \begin{bmatrix} A_1 \\ A_2 \\ A_3 \end{bmatrix} \quad (1.35)$$

Three eigenvectors and corresponding eigenvalues are determined as follows:

$$\vec{A}_1 = (1, 0, 0) \quad \rho\nu_1^2 = a$$

$$\vec{A}_2 = (0, 1, 0) \quad \rho\nu_2^2 = i$$

$$\vec{A}_3 = (0, 0, 1) \quad \rho\nu_3^2 = h$$



where  $\vec{A}_1$  is the P-wave or compressional wave polarization while  $\vec{A}_2$  and  $\vec{A}_3$  are the two S-wave or shear wave polarizations.

By being able to forward calculate the phase velocities from the elastic constants one is able to determine the elastic constants from the phase velocities. However, one must still be able to calculate the phase velocities from the group velocity data. In order to do this operation, the Radon transform will be employed.

## 1.4 Radon transform

As mentioned previously, a slant-stack (Radon) transform is a mapping of a two-dimensional function  $f(x, t)$  from the offset-time  $(x, t)$  domain into the intercept time-horizontal slowness  $(\tau - p)$  domain. The slant stack (Radon) transform is defined by Robinson (1982) and Tatham (1984) as :

$$F(\tau, p) = \int_{-\infty}^{\infty} f(x, \tau + px) dx \quad (1.36)$$

where  $F$  is the integration of the amplitudes  $f(x, t)$  along the line  $y = \tau + px$ .

This equation basically means the data are decomposed into different plane wave components where for each  $\tau$  value on a given horizontal slowness  $p$ , the amplitudes of all the samples along the line given by the line  $y = \tau + px$  is summed. Since this summation is performed over slanting lines, the Radon transform is occasionally called a slant stack.

To summarize, offset-time data are converted to  $\tau - p$  space by the application of the Radon transform where the intercept time  $\tau$  is a function of the horizontal slowness  $p$ . By combining the information gathered from the two  $\tau - p$  curves obtained from data gathered in the same plane, the phase velocity  $\nu$  is determined as a function of the propagation angle or direction of propagation.

This methodology is described in more detail in Chapter 2.

## References

Arts, R. J., Rasolofosaon, P. N. J., and Zinszner, B. E., 1991. Complete inversion of the anisotropic elastic tensor in rocks: Experiment versus Theory: 61st Ann. Internat. Mtg., Soc. Expl. Geophys., Expanded Abstracts, 1538-1541.

Arts, R.J., 1993. A study of general anisotropic elasticity in rocks by wave propagation: Theoretical and experimental aspect, Ph. D. thesis. Institut Français du Pétrole.

Backus, G. E., 1962. Long-wave anisotropy produced by horizontal layering: J. Geophys. Res., **67**, 4427-4440.

Banik, N. C., 1984. Velocity anisotropy of shales and depth estimation in the North Sea basin: Geophysics, **49**, 1411-1419.

Brocher, T. M., and Christensen, N. I., 1990, Seismic anisotropy due to preferred mineral orientation observed in shallow crustal rocks in southern Alaska: Geology, **18**, 737-740.

Carlson, R. L., Schaftenaar, C. H., and Moore, R. P., 1984, Causes of compressional-wave anisotropy in carbonate-bearing, deep-sea sediments: Geophysics, **49**, 525-532.

Carcione, J. M., Kosloff, D., and Behle, A., 1991, Long-wave anisotropy in stratified media: A numerical test: Geophysics, **56**, 245-254.

Christensen, N. I. and Salisbury, M. H., 1979. Seismic anisotropy in the oceanic upper mantle: Evidence from the Bay of Islands Ophiolite Complex: *J. Geophys. Res.*, **84**, no. B9, 4601-4610.

Crampin, S., 1978. Seismic-wave propagation through a cracked solid: polarizations as a possible dilatancy diagnostic: *Geophys. J. R. astr. Soc.*, **53**, 467-496.

Dellinger, J., and Vernik, L., 1994. Do traveltimes in pulse-transmission experiments yield anisotropic group or phase velocities?: *Geophysics*, **59**, 1774-1779.

Helbig, K., 1981. Systematic classification of layer-induced transverse isotropy: *Geophysical Prospecting*, **29**, 550-577.

Helbig, K., 1984. Anisotropy and dispersion in periodically layered media: *Geophysics*, **49**, 364-373.

Hornby, B., 1996. Experimental determination of anisotropic properties of shales, in Fjaer, E., Holt, R. M., and Rathore, J. S., Eds., *Seismic Anisotropy: Soc. Expl. Geophys.*, 238-296.

Hornby, B. E., Schwartz, L. M., and Hudson, J. A., 1994. Anisotropic effective-medium modeling of the elastic properties of shales: *Geophysics*, **59**, 1570-1583.

Hovem, J. M., 1995. Acoustic waves in finely layered media: *Geophysics*, **60**, 1217-1221.

Johnston, J. E., and Christensen, N. I., 1995. Seismic anisotropy of shales: *J. Geophys. Res.*, **100**, no.B4, 5991-6003.

Kaarsberg, E. A., 1959. Introductory studies of natural and artificial argillaceous aggregates by sound-propagation and x-ray diffraction methods: *J. Geol.*, **67**, 447-472.

Kawasaki, I., and Konno, F., 1984. Azimuthal anisotropy of surface waves and the possible type of the seismic anisotropy due to preferred orientation of olivine in the uppermost mantle beneath the Pacific Ocean: *J. Phys. Earth*, **32**, 229-244.

Kebaili, A., and Schmitt, D. R., 1996. Velocity anisotropy observed in well-bore seismic arrivals: Combined effects of intrinsic properties and layering: *Geophysics*, **61**, 12-20.

Kebaili, A., and Schmitt, D. R., 1997. Ultrasonic anisotropic phase velocity determination with the Radon transformation: *J. Acoust. Soc. Am.*, **101**, 3278-3286.

Lay, T., and Wallace, T. C., 1995. *Modern Global Seismology*: Academic Press.

Levin, F. K., 1979, Seismic velocities in transversely isotropic media: *Geophysics*, **44**, 918-936.

Levin, V., Menke, W., and Lerner-Lam, A., 1996. Seismic anisotropy in the north-eastern US as a source of significant teleseismic P traveltimes anomalies: *Geophys. J. Int.*, **126**, 593-603.

Li, Y. Y., and Schmitt, D. R., 1998, Drilling induced core fractures and in situ stress. *J. Geophys. Res.*, **103**, 5225-5239.

Marion, D., Mukerji, T., and Mavko, G., 1994. Scale effects on velocity dispersion: From ray to effective medium theories in stratified media: *Geophysics*, **59**, 1613-1619.

Melia, P. J., and Carlson, R. L., 1984. An experimental test of P-wave anisotropy in stratified media: *Geophysics*, **49**, 374-378.

Musgrave, M. J. P., 1970, *Crystal acoustics*: Holden-Day.

Okoye, P.N., Zhao, P. and Uren, N.F., 1996. Inversion technique for recovering the elastic constants of transversely isotropic materials: *Geophysics*, **61**, 1247-1257.

Ricker, N., 1953. The form and laws of propagation of seismic wavelets: *Geophysics*, **18**, 10-40.

Robinson, E. A., 1982, Spectral approach to geophysical inversion by Lorentz, Fourier, and Radon transforms: *Proc. of the IEEE*, **70**, 1039-1054.

Sayers, C. M., 1988, Inversion of ultrasonic wave velocity measurements to obtain the microcrack orientation distribution function in rocks: *Ultrasonics*, **26**, 73-77.

Schoenberg, M., and Helbig, K., 1997. Orthorhombic media: Modelling elastic wave behaviour in a vertically fractured earth: *Geophysics*. **62**, 1954-1974.

Tatham, R. H., 1984. Multidimensional filtering of seismic data: *Proc. of the IEEE*. **72**, 1357-1369.

Ulrig, L. F., and Van Melle, F. A., 1955. Velocity anisotropy in stratified media: *Geophysics*, **20**, 774-779.

van Buskirk, W. C., Cowin, S. C., and Carter Jr, R., 1986. A theory of acoustic measurement of the elastic constants of a general anisotropic solid. *J. of Mat. Sci.*, **21**, 2759-2762.

Vernik, L., 1993. Microcrack-induced versus intrinsic elastic anisotropy in mature HC-source shales: *Geophysics*. **58**, 1703-1706.

Vernik, L., and Nur, A., 1992. Ultrasonic velocity and anisotropy of hydrocarbon source rocks: *Geophysics*. **57**, 727-735.

Vestrum, R.W., 1994. Group and phase-velocity inversions for the general anisotropic stiffness tensor, M.Sc. thesis, Univ. of Calgary.

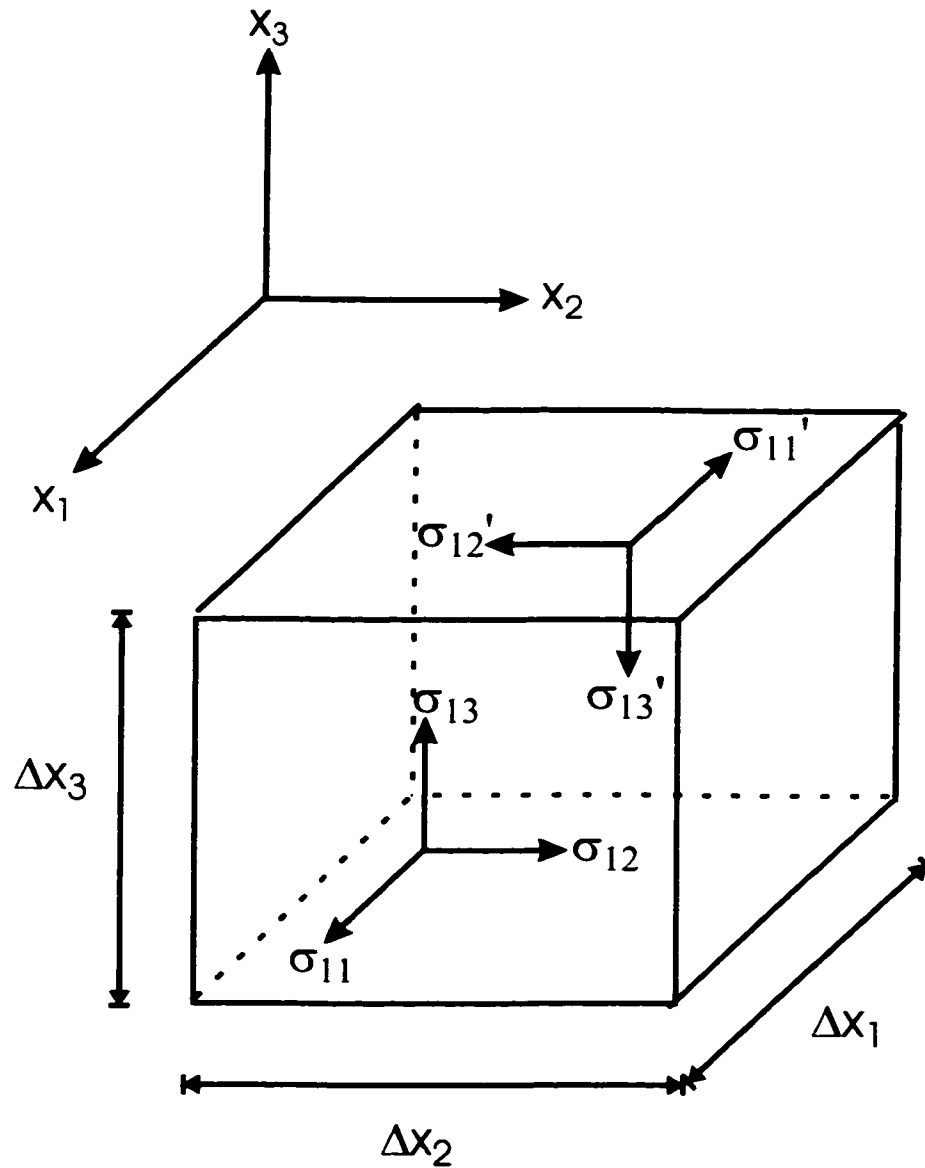


Figure 1.1:  $\sigma_{ij}$  is the stress on the  $i^{\text{th}}$  face in the  $x_j$  direction.  $\sigma'_{ij}$  is the stress on the face opposite the  $i^{\text{th}}$  face on the unit cube and is defined as  $\sigma_{ij} + \frac{\partial \sigma_{ij}}{\partial x_i} (-\Delta x_i)$ .  $\Delta x_i$  is the width of the unit cube in the  $x_i$  direction.

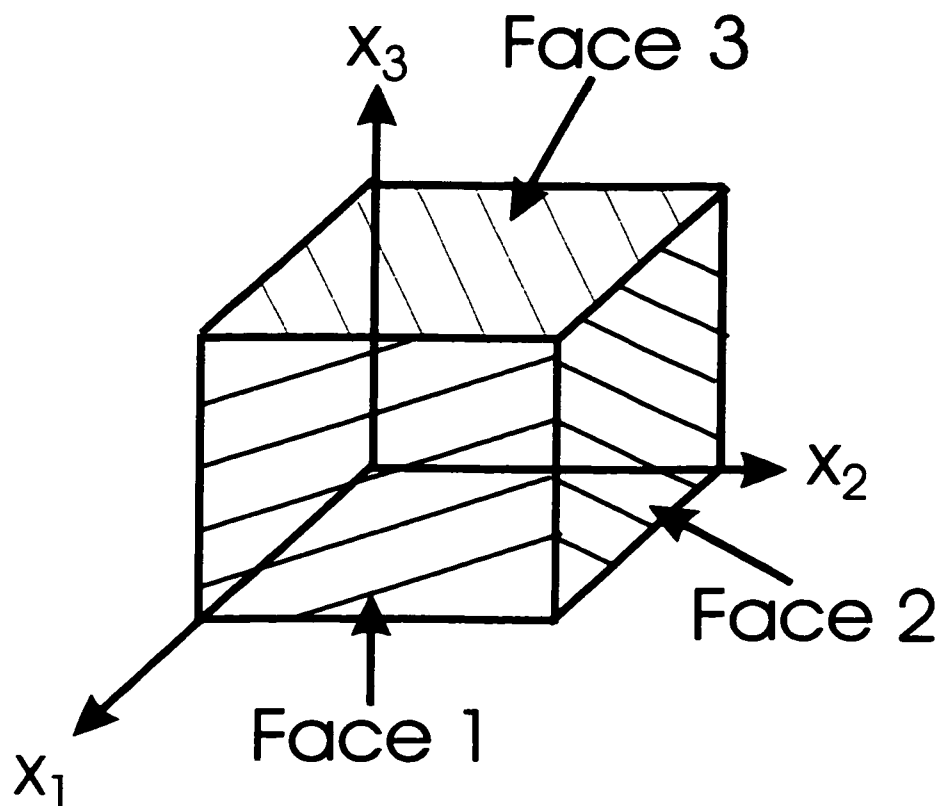


Figure 1.2: Face 1 is the face on the unit cube whose outward normal is parallel to direction  $x_1$ . Face 2 is the face on the unit cube whose outward normal is parallel to direction  $x_2$ . Face 3 is the face on the unit cube whose outward normal is parallel to direction  $x_3$ .



## Chapter 2

# Experimental Determination of the Elastic Coefficients of Anisotropic Materials With the Slant-Stack Method

### 2.1 Introduction

Wave speed isotropy is the usual assumption in reflection seismic profiling. However, most rocks are somewhat intrinsically anisotropic due to texture or aligned microcrack damage. Even simple consideration of this anisotropy improves the resolution of seismic images. Indeed, neglecting to incorporate anisotropy can introduce substantial error in the positioning of subsurface reflectors. Despite this concern, the lack of understanding of the wave speed anisotropy of many rocks hinders in part more realistic seismic imaging and modeling. However, obtaining the elastic coefficients required for more realistic modeling remains difficult.

In this chapter, I describe further development of an experimental method for measuring anisotropic phase velocities in complex media (Kebaili & Schmitt, 1997) which allows for the complete determination of the set of elastic coefficients in materials of orthorhombic symmetry. The method employs arrays of small, specially constructed transducers that impart and receive the quasi-P

(quasi-compressional) and two quasi-S (quasi-shear) modes. Gathers of traces so obtained, in a geometry reminiscent of a walk-a-way vertical seismic profile (VSP) (Kebaili & Schmitt, 1996), are analyzed in the  $\tau - p$  domain. The advantage of this procedure is that phase (plane-wave) velocities, sometimes difficult to measure experimentally, but necessary to characterize a material's elasticity, are directly obtained. The results of tests of the method on isotropic glass and anisotropic composite material indicate its utility. However, certain shear wave arrivals suggest that in complex, layered materials dispersion may need to be considered.

## 2.2 Background

### 2.2.1 Pulse Transmission and Elasticity

A number of scale dependent factors such as the heterogeneity of layering and the orientation of fractures influence seismic wave anisotropy. The intrinsic elastic properties of the rock are also essential factors needed to describe anisotropy. In the most general case, twenty-one independent coefficients define a material's elasticity. Such a complete description is difficult to achieve experimentally, however, and most studies on rock presume on the basis of texture that the rock is either isotropic, transversely isotropic (TI), or orthorhombic with 2, 5, or 9 independent constants, respectively (e.g., Musgrave, 1970).

These elastic constants may in principle be found by measuring the static deformation of a test sample. However, quasi-static measurements can be subject to substantial error due to the difficulties encountered in applying stress and measuring strain: instead, ultrasonic pulse transmission methods have become popular in characterizing complex composite materials and rock since the work of Markham (1957). Briefly in review, one quasi-P wave and two quasi-S plane-waves propagate in any direction through a general homogeneous anisotropic

medium obeying the general Hooke's law (e.g., see Neighbours & Schacher, 1967).

$$\sigma_{ij} = c_{ijkl}\epsilon_{kl} \quad (2.1)$$

where the  $c_{ijkl}$  are the elastic stiffness constants.

If these are plane waves, the phase velocities and polarization directions are the eigenvalues and eigenvectors of :

$$\Gamma_{il}A_l = \rho\nu^2 A_i \quad (2.2)$$

where  $\Gamma_{il}$  are the Christoffel equations dependent on the elastic constants via:

$$\Gamma_{il} = c_{ijkl}n_j n_k \quad (2.3)$$

When the elastic coefficients are known, the wave speeds in any direction are determined by solving Equation (2.3). Conversely, the elastic coefficients may be determined by measuring a sufficient number of wave speeds. If the material is known to be isotropic, the elastic coefficients are found by measuring only a P and an S wave speed in any direction. The minimum number of wave-speed measurements required increases for materials of lower symmetry (more independent coefficients) and if the directions of symmetry in a given test piece are unknown.

Since the early measurements of Markham (1957) on cubic and hexagonal metals, numerous methods have been developed for geophysical application. A few methods include pulse transmission through specially machined spheres (Pros & Babuska, 1967; Thill et al., 1969; Pros & Podrouzkova, 1974; Vestrum, 1994) or multifaceted prisms (Markham, 1957; Carlson et al., 1984; Arts et al., 1991; Cheadle et al., 1991; Vestrum, 1994) but most commonly through carefully oriented cylindrical core samples (e.g., Kaarsberg, 1959; Vernik & Nur, 1992; Vernik, 1993; Johnston & Christensen, 1995; Hornby, 1996).

One complication in such analyses is that the phase, or plane wave, velocity necessary to determine the elastic coefficient may often differ from the more easily obtained group (or ray) velocity. Essentially, an observer at P (Figure 2.1), detecting the arrival of the wavefront W, curved due to the anisotropy of the medium, at time  $t$  after excitation of a source at the origin O, determines a group velocity  $d/t$  for the ray along the line between O and P described by angle  $\phi$ . However, this observer cannot distinguish the wavefront W from a plane wave front F with normal at angle  $\theta$  that passed through O at the time of excitation. The speed of this plane wave is the same as the corresponding phase velocity the magnitude of which is given by  $D/t$ . The physical consequences of this difference are well documented (e.g., see Musgrave, 1970; Auld, 1973) and introduce ambiguity to experimental velocity measurements in anisotropic media (Dellinger & Vernik, 1994; Vestrum, 1994; Kebaili & Schmitt, 1997). Without careful consideration of the sample and transducer geometries, it can be difficult to know whether group, phase, or some intermediate velocity is measured. Group velocities may be converted to phase velocities if a sufficient number of the former are measured to allow a smooth differentiation with respect to the propagation angle (see Thomsen, 1986). Indeed, Vestrum (1994) developed a specialized procedure to invert the group velocities obtained in pulse transmission experiments over a sphere and a multifaceted prism of an orthorhombic composite similar to that employed here. Okoye et al. (1996) resorted to smooth polynomial fitting of phase velocities observed obtained through a bar of transversely isotropic material in order to minimize the errors.

### 2.2.2 Plane-wave Decomposition

Not being able to measure phase velocities, in Equation 2.2, adds error to, or substantially complicates, the determination of the elastic coefficients in pulse

transmission measurements (Vestrum, 1994; Okoye et al., 1996). One approach to reduce these problems is to implement a plane-wave decomposition via the  $\tau-p$  analysis (Kebaili & Schmitt, 1996, 1997) which provides directly the phase velocity as a function of the ray parameter (or horizontal slowness)  $p(\theta) = \sin(\theta)/\nu(\theta)$  where  $\theta$  defines the direction of the normal to the plane wave propagating with directionally dependent phase velocity  $\nu$ . The slowness parameter  $p$  is equivalent to the raypath parameter as described by the Snell's law in Equation 2.4 where  $\theta_1$  and  $V_1$  are the incident angle and velocity in medium 1 and  $\theta_2$  and  $V_2$  are the incident angle and velocity in medium 2.

$$\frac{\sin \theta_1}{V_1} = \frac{\sin \theta_2}{V_2} = p \quad (2.4)$$

The essential components of the phase velocity determination method are previously described (Kebaili & Schmitt, 1997) and are only outlined here. In the technique, the pulsed elastic wave energy produced from a minimum of two source transducers are detected by a coplanar array of receiving transducers mounted on the adjacent side of the test piece (Figure 2.2a). The sets of arrival times from each of the two transducers yield hyperbolic-like offset versus travel-time curves in the  $x-t$  domain (Figure 2.2b) which transform to ellipse-like curves in the  $\tau-p$  domain (Figure 2.2c). If the block of material is homogeneous, then at constant horizontal slowness  $p$  the vertical slowness  $q$  is (Kebaili & Schmitt, 1997):

$$q(p) = \frac{\tau_2(p) - \tau_1(p)}{z_2 - z_1} \quad (2.5)$$

where  $\tau_1$  and  $\tau_2$  are the intercept times at constant  $p$  corresponding to the  $\tau-p$  curves for the sources at offsets  $z_1$  and  $z_2$ , respectively (Figure 2.2c). It is worth noting that  $q$  in an anisotropic material depends on the horizontal slowness  $p$  and is hence also implicitly dependent on the propagation angle  $\theta$  within the plane.

The phase velocity  $\nu$  is then

$$\nu(\theta) = (q^2(\theta) + p^2(\theta))^{-1/2} \quad (2.6)$$

at the phase propagation angle:

$$\theta = \arctan\left(\frac{p}{q}\right) \quad (2.7)$$

### 2.2.3 Experimental Method

Experiments were carried out on blocks of soda-lime glass and an industrial composite of laminated fibre mats in a phenolic epoxy. The symmetries of such composites are relatively well controlled and as such they have been used in tests by numerous authors (Cheadle et al., 1991; Karayaka & Kurath, 1994; Vestrum, 1994; Okoye et al., 1996; Kebaili & Schmitt, 1997)

Silicate glasses are essentially frozen fluids with no preferred textural direction and provide a highly isotropic and homogeneous mechanical medium. The 20 cm x 20 cm x 8 cm block employed was prepared from materials used in wall construction. Two adjacent perpendicular surfaces were prepared using a surface grinder, the flatness of the surfaces was measured to be better than 0.1 mm. In simple direct pulse transmission, the P- and S-wave velocities were measured to be  $5690 \pm 60$  m/s and  $3440 \pm 26$  m/s, respectively. The error was determined from the standard deviation in the data. The bulk density was  $2600 \pm 100$  kg/m<sup>3</sup>.

The composite consists of layers of woven fibre mats bonded with the epoxy. Two directions are defined by the weave of the mats with the directions of the straight and the woven fibres are termed the warp and weft, respectively. The layering, warp, and weave reduce the symmetry to orthorhombic (Karayaka & Kurath, 1994) with a substantial anisotropy in planes parallel to the z axis (Fig-

ure 2.3) but with weaker anisotropy within the x-y plane. A large block 66 x 27 x 17 cm of this material (grade CE phenolic) was milled to provide flat and perpendicular surfaces paralleling the layering, the warp, and the weave. The mass density of this composite is given by the manufacturer as 1395 kg/m<sup>3</sup> and there are approximately 20 fibre mats per cm thickness within the material.

One P and two S wave transducers that acted as both sources and receivers were prepared from piezo-electric ceramics. The transducers were made as small as possible in order that the transducer dimension effects could be minimized. P-wave transducers were prepared from commonly available PZT-5 (lead zirconate) sheets by cutting into 2.0 mm squares using a computer controlled diamond saw used in electronic chip manufacturing. These transducers predominantly expand in the direction perpendicular to the block (Figure 2.4a). The nominal resonant frequency of these transducers is 1.0 MHz. S-wave piezo-electric ceramics (EBL #3 - Stavely Sensors) with a resonant frequency of 0.65 MHz were cut into 2 mm X 3 mm rectangles in two perpendicular directions to make transducers preferentially sensitive to the different quasi-S wave polarizations. The two differing cuts of S-wave transducers produce displacements parallel to the surface of the test piece, referred to hereafter as SV and SH, that are also parallel (Figure 2.4b) and perpendicular (Figure 2.4c) to the source-receiver array plane, respectively. These designations of P, SV, and SH polarization should not be taken too literally especially when employed over complex anisotropic media with quasi-P and quasi-S polarizations, these designations simply refer to the mode which is attempted to be preferentially generated given the experimental limitations.

Due to directionality constraints in the outward propagation of energy from the source, the SV transducers were poor transmitters although they were still used in reception. The P transducers were found to better generate SV-like polarizations and were consequently used for transmitting in both the P and SV

arrays. This effect is expected as the P transducers act as vertical point sources that also generate an SV radiation pattern with substantial energy at oblique angles.

All the transducers were mechanically damped to increase their bandwidth by potting in a urethane-metal powder mixture. The P-wave transducers were mounted on a conductive, malleable, removable substrate that was clamped to the block. Both SV and SH transducers were directly glued to the samples using conductive silver paint.

The transducers were placed on the sample in a coplanar array as shown in Figure 2.2a with two transmitters on one side at a spacing of  $2.0 \text{ cm} \pm 0.1 \text{ cm}$ . The receiving transducers were mounted in a linear array on the adjacent perpendicular surface at a spacing of  $0.5 \text{ cm} \pm 0.1 \text{ cm}$ . The source transducers were activated with a 300 Volt, 10 ns rise time spike. The response of the receiver transducers to the resulting elastic waves were digitally acquired by a high speed sampling oscilloscope at a rate of 8 ns/sample for  $120 \mu\text{s}$  with the waveforms transferred via a GPIB bus to a computer for archiving and analysis. Nonetheless, random noise was a significant problem due to the small sizes of the transducers. The sample was shielded in a grounded steel box and high frequency line filters were included on all electrical equipment to reduce this noise. Approximately 2000 individual pulses were stacked on the oscilloscope to improve the data quality.

Only simple processing of the waveforms was carried out to reduce the effects of trigger noise and spurious reflected and other mode arrivals. The high amplitude trigger noise was simply muted as were portions of the trace before and after the desired arrivals by modulation with a simple tapered window. These data were then bandpass filtered (bandpass = 0 MHz - 0.15 MHz - 1.20 MHz - 1.70 MHz) to remove any of the remaining high frequency noise.



Examples of the processed waveforms acquired on the glass block are shown in Figure 2.5. These data generally show that in the isotropic, low-attenuation glass the waveforms retain much of the same character with offset and indicate that consistent signals are generated and received. The  $\tau - p$  transform was accomplished by a conventional  $x - t$  domain slant-stack (Appendix C). The slant-stack of the P-wave  $x - t$  traces obtained on the glass block at the depth of 2.0 cm is shown in Figure 2.6. The  $\tau(p)$  values at the first amplitude peak, used in  $\Delta\tau(p) = \tau_2(p) - \tau_1(p)$  in Eqn. 2.5, were picked iteratively. Analysis of the shape of this  $\tau - p$  curve using Eqns. 2.5 to 2.7 yields velocities of  $5724 \pm 64$  m/s and  $3467 \pm 15$  m/s for the P and SH mode transducers, respectively. The P and SH velocities agree to better than 1% with P ( $5690 \pm 60$  m/s) and S ( $3440 \pm 26$  m/s) velocities measured directly through the block as noted earlier. This agreement suggests that uncertainties of better than 1.0 % may be expected using the  $\tau - p$  technique under well controlled conditions for a homogeneous material which, for practical purposes, may be considered lossless (i.e., nondispersive).

## 2.3 Results and Discussion

### 2.3.1 Phase Velocities

Arrays were constructed within 4 different planes on the composite material oriented with respect to the texture in the x-z, the y-z, the x-y and xy-z, a diagonal plane containing the z axis rotated  $45^\circ$  from the x axis (Figure 2.7). The three different P, SV, and SH polarizations were obtained at two different source depths in each of these planes resulting in a total of 24 individual sets of data composed of 920 source receiver combinations. Analysis of the resulting  $\tau - p$  curves yielded 624 high-quality measurements of the phase velocity of which only the portion of the results for the x-z plane is presented for illustration.

The P-wave transducers for the x-z array were arranged with the sources at

2 cm and 4 cm depth on the y-z plane and the receivers mounted on the x-y plane (Figure 2.4a). The processed waveforms (Figure 2.8) display a hyperbolic-like moveout with increasing offset and show only a modest degree of dispersion. The resulting  $\tau - p$  transforms (Figure 2.8) have ellipse-like shapes as expected. However, at  $\tau = 0$  (i.e., when the vertical slowness  $q = 0$ ) both ellipses intersect at  $300 \mu\text{s/m}$  and  $310 \mu\text{s/m}$  which yield at face value horizontal velocities of  $3333 \text{ m/s}$  and  $3226 \text{ m/s}$ , respectively. This discrepancy is not unexpected as such angles cannot be truly illuminated within the given experimental configuration and should be taken as indicative of edge effects in the transformation. Modeling and experience with the data suggest that with the present arrangement of the arrays the phase velocities obtained between phase propagation angles  $\theta$  from  $5^\circ$  to  $70^\circ$  will be valid. In this plane of investigation, the phase propagation angle is the angle from the z axis which describes the direction the plane wave propagates in.

The x-z plane P vertical slowness  $q$  versus horizontal slowness  $p$  (Figure 2.9a) obtained from the  $\tau - p$  transforms shows substantial divergence from isotropic behaviour. The high degree of velocity anisotropy within the material is shown when the  $q - p$  plot is converted to  $\nu - \theta$  (Figure 2.9b) where over the range of phase propagation angles where the results are valid ( $5^\circ$  to  $70^\circ$ ) the velocity increases from  $2650 \text{ m/s}$  to  $3450 \text{ m/s}$  as the propagation direction varies from near vertical to subhorizontal.

While analysis of the P mode transducers is relatively straightforward, obtaining results from the SV mode is complicated by the strong coupling between the P and SV mode with both unavoidably generated at the same time. As noted earlier, P mode transducers were used for SV wave generation and this arrangement introduces problems of directionality (Figure 2.10a) in which a strong P wave arrival exists over much of the array. This arrival is followed by a later

SV mode that is substantially weaker at greater offsets. Again, this result is not unexpected as the radiation pattern for a vertical point source has strong P amplitudes in the direction of particle motion and SV amplitudes at more oblique angles (e.g., White, 1983). For this mode, the P and SV modes produced at the 2.0 cm depth were not sufficiently separated in time to allow for accurate velocity determination and the results shown were obtained from sources at 4.0 and 6.0 cm depths. There is little that can be done to ameliorate this aspect as the P-SV coupling is intrinsic to wave propagation in elastic materials. At the greater depths, however, the two modes are sufficiently distinct to allow the P mode to be muted, isolating the SV arrivals (Figure 2.10b) for transformation to the  $\tau - p$  domain (Figure 2.10c). The  $\tau - p$  curve in Figure 2.10c is quite continuous but straightens towards the end. Judging from the continuity of the  $\tau - p$  curve and the level of error in the data caused by transducer placement problems or heterogeneities within the sample, it seems the slant-stack Radon transform contains a degree of averaging to reduce this error. Also the  $\tau - p$  curve straightens out towards the end because the slant stack Radon transform was performed past the physical limits of the data. In other words, the array of receivers extended out a finite distance allowing only a range of angles to be investigated. This means a limited the range of  $p$  or slowness values may be investigated.

A further complication is the shape of the SV mode waveforms that display substantial waveform stretching and increasing complexity with offset. This waveform stretching is attributed to dispersion whereby the different frequencies of the waveform travel at differing velocities. Some of this complexity is likely due to cross-talk between the SV and SH mode particle motions. However, the composite is primarily a layered medium in which the scale of the layering relative to the wavelengths introduced can be important (e.g., Helbig, 1984; Marion

et al., 1994; Rio et al., 1996). The observed waveform complexities may be a manifestation of the influence of the layering on wave propagation. Examination of these waveform effects is deferred in order to focus on the anisotropy determination strategy.

The SH mode traces are cleaner with a sharp waveform (Figure 2.11a) allowing for a clear  $\tau - p$  transformation (Figure 2.11b). The SH mode transducers were not subject to the same cross-talk as seen for the SV records above. However, there is noticeable spreading of the waveforms with propagation distance which is not seen in the case for the glass indicating that there is substantial dispersion for the SH mode also. Though difficult to quantify, there appears to be slightly less dispersion for the SH mode in the x-y plane.

P, SV, and SH phase velocities obtained from the analyses of the complete set of  $\tau - p$  transformations are shown in Figures 2.12 to 2.15. As expected, the planes containing the z-axis perpendicular to the lamination are highly anisotropic for both P and S modes. The greatest P anisotropy is 23 % in the y-z plane whilst the greatest SH anisotropy is seen in the y-z plane with 13 %. Both the P and SH modes show extremum at phase angles approaching the principle directions. Interestingly, within the x-y plane the greatest phase velocity is observed near  $45^\circ$ .

### 2.3.2 Inversion for Elastic Coefficients

A generalized least-squares inversion method was developed to obtain the elastic coefficients from observed phase velocities and propagation angles. Relatively straightforward inversion methodologies were employed (Kincaid & Cheney, 1996) and the strategy need only be briefly outlined here. Further details on the computer code employed may be found in Appendix C. The inversion strategy begins with an initial guess at the elastic coefficients with the assump-

tion that the density is already well known. Phase velocities with propagation angle are calculated from this seed and the residuals of these with those observed are minimized using an L2 norm. Both nearest-neighbor and secant methods (Kincaid & Cheney, 1996) are iteratively employed. Pseudo-random jumps in the values are included to prevent trapping of the inversion in a local minimum. This method was first tested on a number of synthetic results in which the phase velocities were first forward modeled on a hypothetical orthorhombic material. In the noise-free case, the elastic coefficients were reproduced to better than 0.01 %. The influence of various levels of noise, in the sense of both electrical effects and transducer misplacement, was modeled by the addition of random noise to synthetic data. This method showed the inversion to be accurate within an average of 3 % for random errors in velocity of up to 10 % (Appendix C).

This inversion methodology was applied to the 624 obtained values of phase velocity versus phase angle summarized in Figures 2.12 to 2.15. The inversion assumed the material was orthorhombic and that the x-z, x-y, and y-z planes were planes of symmetry. Two greatly different seed values were used: one in which all the elastic coefficients were initially zero and another provided by Vestrum (1994) on a similar material. The procedure was stopped once 500 iterations of the inversion were performed. The calculation typically required only 448 seconds on a 170 MHz machine using a high level programming language. The inverted results are shown in Table 2.1 in the notational style used by Vestrum (1994) and a statistical analysis of the results indicate they are accurate to within 2 %. The choice of the seeds was not important as both initial guesses approached the solution within 300 iterations and the final difference between the solutions differed by only 5 MPa or by less than 0.2 %.

One way to test the reliability of the method is to use the resulting elastic coefficients to calculate in a forward sense what the phase velocities would be.

These theoretical phase velocity values are shown as lines in Figures 2.12 to 2.15 for the sake of comparison. The SH wave velocities are generally well determined with a maximum discrepancy of 87 m/s between the calculated and observed values. The P and SV mode phase velocities are less well determined with the greatest error of 182 m/s seen for the P mode in the y-z plane. The reasons for this discrepancy are not fully understood but may be due to the dispersion present for both the P and SV waveforms. Further, the degree of error is expected to be higher for the SV mode due to the problems already indicated and because, even in the anisotropic medium, these two modes will preferentially be coupled relative to the SH mode it might be expected that this coupling will introduce error into the P mode determinations.

Various types of inversions done by others with important differences when compared with the type of inversion used in this thesis. Arts et al. (1991) solved for all 21 elastic constants of the stress-strain tensor in the least-squares sense using the measurements of the phase velocities and the corresponding polarizations for various directions of propagation. Okoye et al. (1996) assumes that the material is transversely isotropic and applies a smooth polynomial fitting to the phase velocities before applying the least-squares method iteratively. Vestrum (1994) treats the material being studied as triclinic even though studies have shown that it is orthorhombic in nature. Vestrum's (1994) inversion used is an iterative application of Newton's method. The inversion used in this thesis treats the material as orthorhombic though it can handle the triclinic case. The inversion requires the phase velocities with the corresponding polarizations for differing directions of propagation. The inversion is applied without the application of a smooth polynomial fitting unlike Okoye et al. (1996). The inversion does use the application of an iterative least-squares inversion similar to Arts et al. (1991) and Okoye et al. (1996) as well as the secant method, similar to Newton's method

used by Vestrum (1994). The inversion makes use of pseudo-random jumps in order to prevent entrapment in localized minima in the residuals unlike the use of damping factors in Vestrum (1994).

For an orthorhombic medium, four distinct planes on the sample are investigated in Figure 2.7. The three non-diagonal planes are the only ones necessary to determine the 9 elastic constants of the stress-strain tensor if the planes are oriented along known axes of symmetry. The diagonal plane is investigated in order to help localize the results because axes of symmetry may not be well defined. If the situation arises that no information about the axes of symmetry of the orthorhombic material is known or that the material is indeed triclinic, a more general approach needs to be taken. The most general approach in order to determine the elastic constants requires three planes orientated along an arbitrary set of axes and two perpendicular planes running diagonally to this set of axes. It is recommended to use an additional third diagonal plane, in order to help constrain the results better, for a total of six distinct planes to accurately determine the 21 independent elastic constants of the stress-strain tensor.

Although the elastic coefficients were readily determined from a number of phase velocities in the above inversion, some experimental problems remain. The most important is the observation of substantial dispersion. This dispersion is evident all the records of the P, SV, and SH mode waveforms seen in Figures 2.5, 2.8, and 2.10. This dispersion is only weakly, if at all, detectable in the measurements on glass, a nearly ideal, high Q, elastic medium suggesting that the dispersion may in part be a consequence of the structure or composition of the material. Another possible cause is that of a wave travelling through a layered medium where the ratio of the wavelength of the propagating wave to the layer thickness becomes an important factor. Attenuation is another possible cause of the spreading of waveforms with offset where the higher frequencies would

be attenuated more than the low frequencies. This dispersion must have some influence on the accuracy of the  $\tau - p$  method of phase velocity determination and needs to be considered in the future (see Martinez & McMechan, 1984). Other potential problems reside with the difficulties of cleanly separating different arrivals and the unavoidable P-SV mode coupling. This is due to the complexities in polarization of the different modes in an anisotropic medium (e.g., Crampin, 1978) and the related imperfections of the transmitting and receiving transducers. A final problem is that only a limited range of angles may be covered with the transducer arrays and for equal spacing of transducers this will introduce a sampling bias towards the far offset transducers.

## 2.4 Conclusions

Phase velocities were determined directly as a function of phase propagation angle on an anisotropic composite material of orthorhombic symmetry. Special, near-point transducers were developed to impart and receive different elastic wave energies. These transducers were designated as P, SV, and SH to indicate the primary mode of particle motion to which each different transducer was sensitive. However, it must be noted that such pure modes do not generally propagate in anisotropic media where more complex polarizations exist and the designations should only be considered as approximate. Clean P and SH modes could be generated and received in both glass and the test anisotropic composite. However, the SV mode is complicated by the coupled nature of P and SV waves and by difficulties the directionality of SV mode receivers to impart the desired wave energy into the medium. Twenty four arrays of these transducers were constructed along 4 strategic planes of the composite material allowing 624 individual P, SV, and SH mode phase velocities to be obtained. When the experimental approach was tested on a block of soda-lime glass, an essentially isotropic, low loss, elastic



medium. the P and S velocities were recovered to better than 1 % relative to conventional pulse transmission tests. In the glass it was difficult to detect any dispersion by spreading of the observed waveforms with increasing propagation distance.

Under the assumption that the test composite material was orthorhombic, nine independent elastic constants were obtained by a nonlinear least-squares inversion procedure. Phase velocities, calculated in a forward manner using the obtained elastic constants, indicate that these elastic constants are in generally good agreement with the observed phase velocities. However, some discrepancies remain and these may be due, in part, to the fact that there is very noticeable dispersion in all the waveform modes (i.e., pulse spreading with increasing propagation distance) particularly for the SV mode. This dispersion is not accounted for in the present  $\tau - p$  velocity determination method. Further, because of experimental constraints, the predominant frequencies of the compressional and the shear mode transducers differed at 1.0 MHz and 0.65 MHz, respectively. The band difference together with the observed dispersion effects possibly account, in part, for the discrepancies. Further, it is highly likely that there is some small scale heterogeneities within the laminated composite as a consequence of its construction and these structures could also introduce additional errors to the measurements. However, the smoothing intrinsic to the  $\tau - p$  method should alleviate the effects of small scale heterogeneities to some degree.

Although part of the waveform spreading with offset may possibly be due to intrinsic attenuation, it is also likely that part of the effect may be a consequence of wave propagation through the layered structure of the composite. Although difficult to quantify, there appears to be less dispersion in the x-y plane waveforms suggesting that the observed dispersion is symptomatic of the layering. Indeed, such layering induced dispersion is not unexpected especially once the dimensions

of the layers approach the wavelength of the illuminating elastic wave energy (e.g., Helbig, 1984). This situation may be the case in the present material as the wavelength of the shear waves approach 2 mm which is only a factor of 4 greater than the nominal 0.5 mm scale of the layering. Such effects were first hinted at experimentally by Melia & Carlson (1984) on plastic-glass composites.

Future work will focus on technical development of the technique in order to make it less cumbersome and so it can be employed under pressure. One great advantage of the present methodology is that it can be applied to samples of simple shape such as rectangular prisms and even cylinders. The latter will be particularly useful in the context of determining anisotropy in shales which may often assumed to be transversely isotropic using core samples with a minimum of additional preparation. Of more fundamental concern, however, is the potential for experimental tests of the trade-off between wave velocity anisotropy, dispersion, and scale in layered anisotropic media: these future experiments have implications beyond laboratory determination of elastic properties. The  $\tau - p$  method will aid in such fundamental studies of layered media.

$C_{ij}$ (GPa)	j=1	j=2	j=3	j=4	j=5	j=6
i=1	16.351 ± 0.166	7.085 ± 0.079	6.621 ± 0.142	0	0	0
i=2	7.085 ± 0.079	15.391 ± 0.017	6.584 ± 0.115	0	0	0
i=3	6.621 ± 0.142	6.584 ± 0.115	10.593 ± 0.079	0	0	0
i=4	0	0	0	3.399 ± 0.018	0	0
i=5	0	0	0	0	2.974 ± 0.024	0
i=6	0	0	0	0	0	3.813 ± 0.005

Table 2.1: Elastic constants of the stress-strain tensor for a sample of the orthorhombic material phenolic.

## References

- Arts, R. J., Rasolofosaon, P. N. J., and Zinszner, B. E., 1991. Complete inversion of the anisotropic elastic tensor in rocks: Experiment versus Theory: 61st Ann. Internat. Mtg., Soc. Expl. Geophys., Expanded Abstracts, 1538-1541.
- Auld, B. A., 1973. Acoustic fields and waves in solids: John Wiley and Sons, Inc.
- Carlson, R. L., Schaftenaar, C. H., and Moore, R. P., 1984. Causes of compressional-wave anisotropy in carbonate-bearing, deep-sea sediments: *Geophysics*, **49**, 525-532.
- Cheadle, S. P., Brown, R. J., and Lawton, D.C., 1991. Orthorhombic anisotropy: A physical seismic modeling study: *Geophysics*, **56**, 1603-1613.
- Crampin, S., 1978. Seismic-wave propagation through a cracked solid: polarization as a possible dilatancy diagnostic: *Geophys. J. R. astr. Soc.*, **53**, 467-496.
- Dellinger, J., and Vernik, L., 1994. Do traveltimes in pulse-transmission experiments yield anisotropic group or phase velocities?: *Geophysics*, **59**, 1774-1779.
- Helbig, K., 1984. Anisotropy and dispersion in periodically layered media: *Geophysics*, **49**, 364-373.
- Hornby, B., 1996. Experimental determination of anisotropic properties of shales, in Fjaer, E., Holt, R. M., and Rathore, J. S., Eds., *Seismic Anisotropy: Soc. Expl. Geophys.*, 238-296.

Johnston, J. E., and Christensen, N. I., 1995, Seismic anisotropy of shales: *J. Geophys. Res.*, **100**, no. B4, 5991-6003.

Kaarsberg, E. A., 1959, Introductory studies of natural and artificial argillaceous aggregates by sound-propagation and x-ray diffraction methods: *J. Geol.*, **67**, 447-472.

Karayaka, M., and Kurath, P., 1994, Deformation and failure behaviour of woven composite laminates: *J. Eng. Mat. and Technol.*, **116**, 222-232.

Kebaili, A., and Schmitt, D. R., 1996, Velocity anisotropy observed in well-bore seismic arrivals: Combined effects of intrinsic properties and layering: *Geophysics*, **61**, 12-20.

Kebaili, A., and Schmitt, D. R., 1997, Ultrasonic anisotropic phase velocity determination with the Radon transformation: *J. Acoust. Soc. Am.*, **101**, 3278-3286.

Kincaid D., and Cheney W., 1996, *Numerical Analysis*: Brooks/Cole Publishing Company.

Marion, D., Mukerji, T., and Mavko, G., 1994, Scale effects on velocity dispersion: From ray to effective medium theories in stratified media: *Geophysics*, **59**, 1613-1619.

Markham, M.F., 1957, Measurement of elastic constants by the ultrasonic pulse method: *British J. Appl. Phys.*, **6**, 56-63.

Martinez. R. D., and McMechen. G. A., 1984, Analysis of absorption and dispersion effects in tau-p synthetic seismograms: 54th Ann. Internat. Mtg., Soc. Expl. Geophys., Expanded Abstracts, Session: S24.2.

Melia. P. J., and Carlson. R. L., 1984, An experimental test of P-wave anisotropy in stratified media: *Geophysics*, **49**, 374-378.

Musgrave. M. J. P., 1970, *Crystal acoustics*: Holden-Day.

Neighbours, J. R., and Schacher. G. E., 1967, Determination of elastic constants from sound-velocity measurements in crystals of general symmetry: *J. Appl. Phys.*, **38**, 5366-5375.

Okoye. P.N., Zhao. P. and Uren. N.F., 1996, Inversion technique for recovering the elastic constants of transversely isotropic materials: *Geophysics*, **61**, 1247-1257.

Pros, Z., and Babuska, V., 1967, A method for investigating the elastic anisotropy on spherical rock samples: *Z. Geophys.*, **33**, 289-291.

Pros. Z., and Podrouzkova. Z., 1974, Apparatus for investigating the elastic anisotropy of spherical samples at high pressure: *Veroof. Zentral Inst. Phys. d. Erde. Potsdam*, **22**, 42-47.

Rio, P., Mukerji, T., Mavko, G., and Marion, D., 1996, Velocity dispersion and upscaling in a laboratory-simulated VSP: *Geophysics*, **61**, 584-593.

Thill, R. E., Willard, R. J. and Bur, T.R., 1969, Correlation of longitudinal velocity variation with rock fabric: *J. Geophys. Res.*, **74**, 4897-4909.

Thomsen, L.. 1986. Weak elastic anisotropy: *Geophysics*, **51**, 1954-1966.

Vernik, L.. 1993. Microcrack-induced versus intrinsic elastic anisotropy in mature HC-source shales: *Geophysics*, **58**, 1703-1706.

Vernik, L. and Nur, A.. 1992. Ultrasonic velocity and anisotropy of hydrocarbon source rocks: *Geophysics*, **57**, 727-735.

Vestrum, R.W., 1994, Group and phase-velocity inversions for the general anisotropic stiffness tensor. M.Sc. thesis. Univ. of Calgary.

White, J. E., 1983, *Underground Sound*: Elsevier Science Publishing Company Inc.

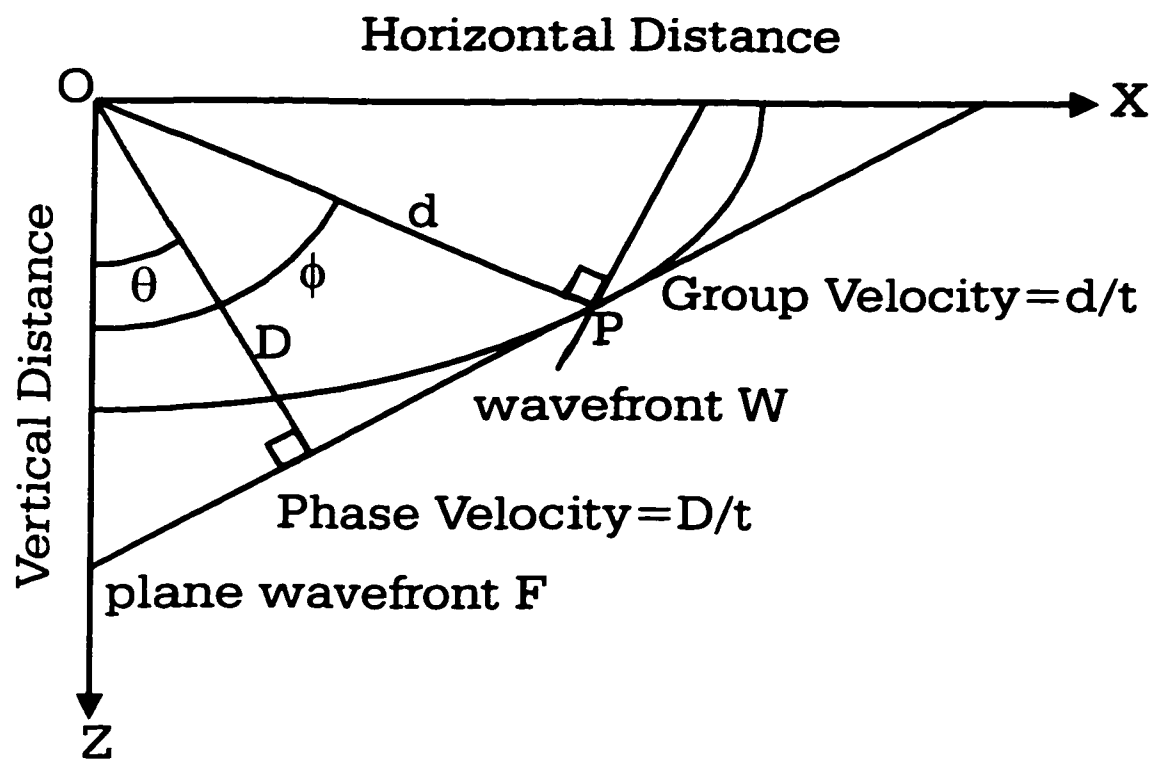
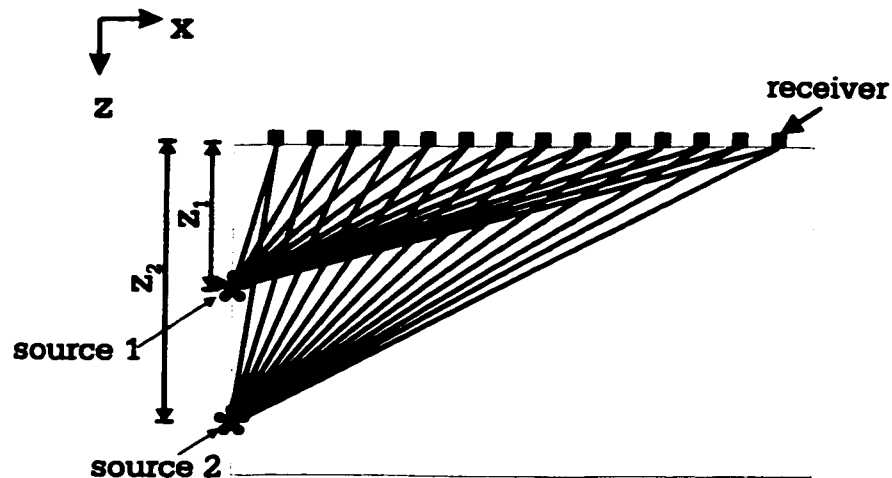
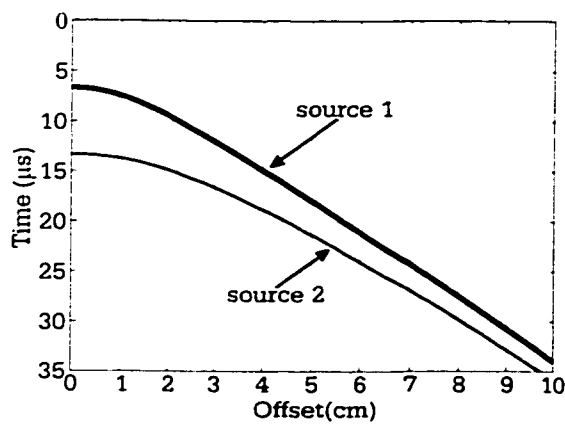


Figure 2.1: Distinction between group and phase velocities in anisotropic media (after Kebaili & Schmitt, 1997).

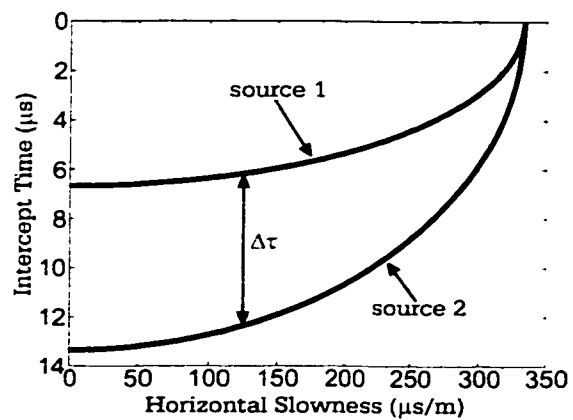




(a) Plan view of the plane containing sources and receivers with ray paths for a homogeneous anisotropic medium.



(b) Composite travel-time versus offset ( $x$ ) curves obtained for the two different source positions in a).



(c) Composite of the  $\tau - p$  transform of the travel-time curves in b) with the determination of  $\Delta\tau$  at a given constant horizontal slowness  $p$  illustrated.

Figure 2.2: Outline of phase velocity determination method.

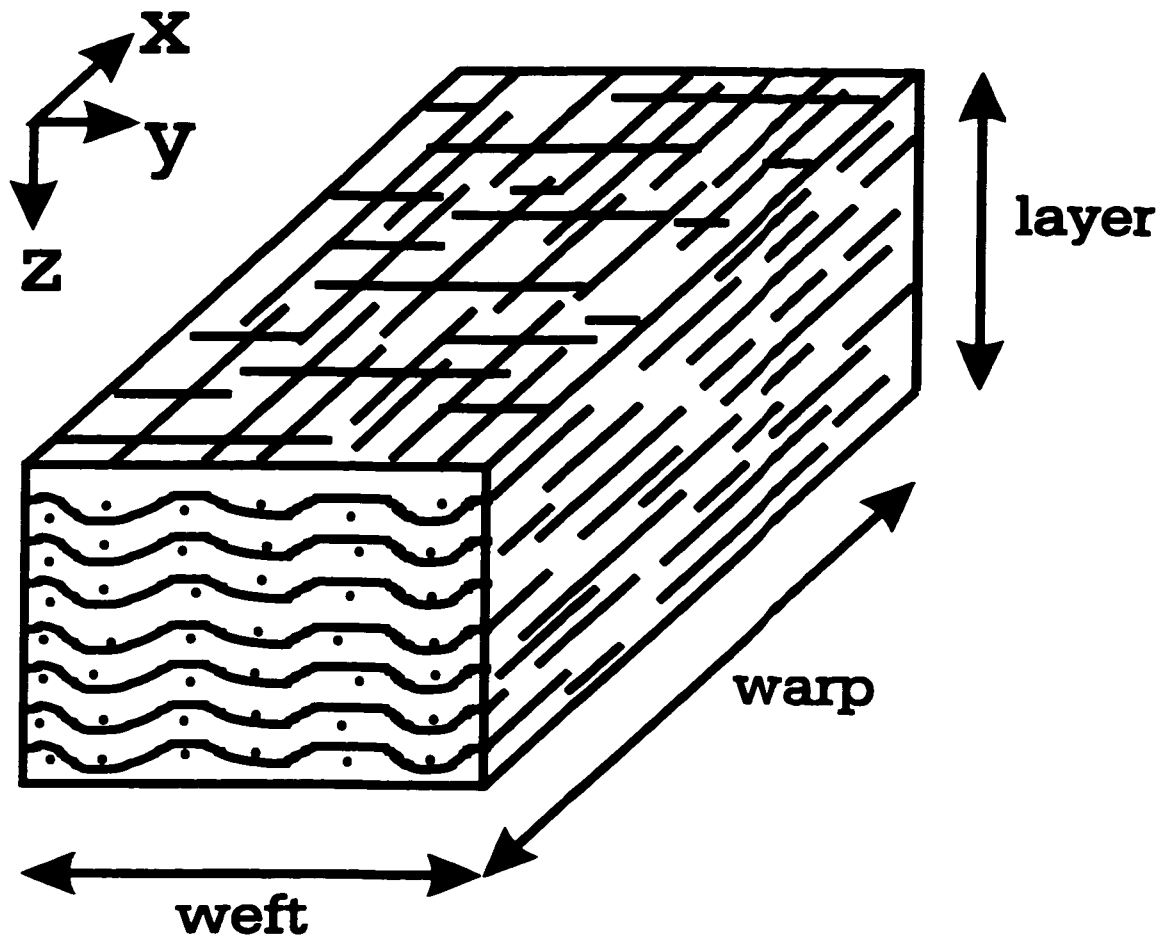
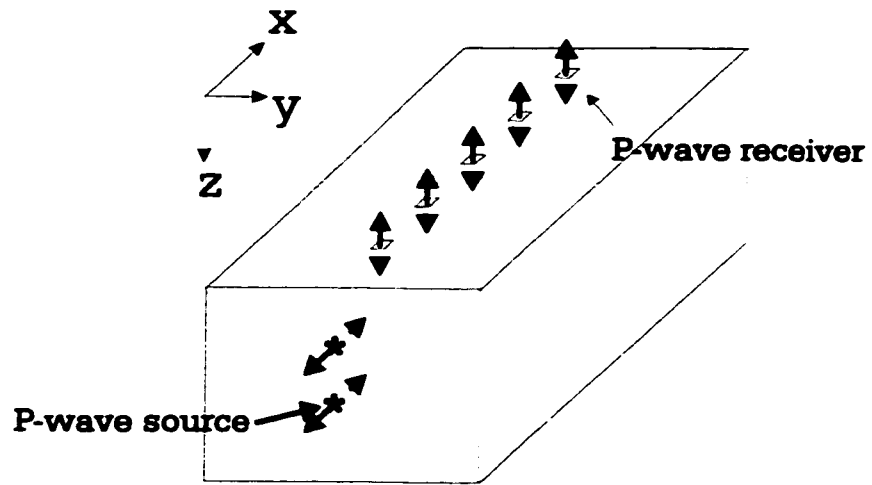
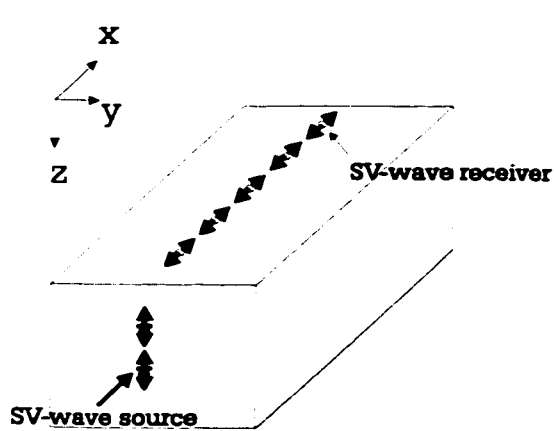


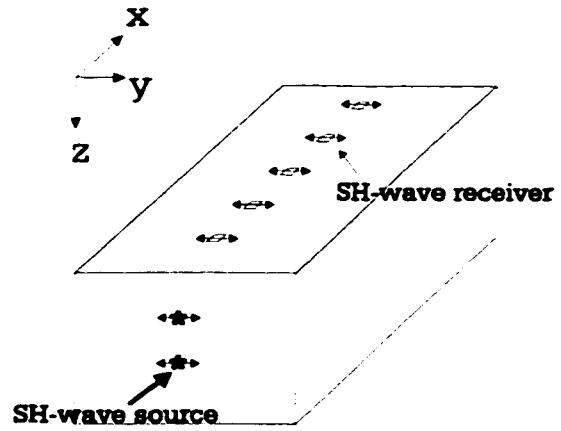
Figure 2.3: Orientation of the principal directions of the phenolic block relative to the  $x$ - $y$ - $z$  co-ordinate reference axes employed.



(a) P mode transducer.

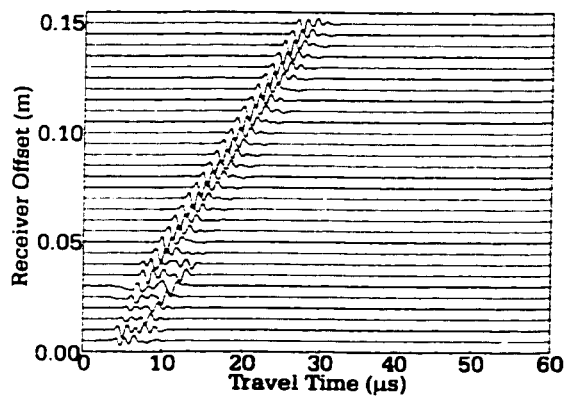


(b) SV mode transducer.

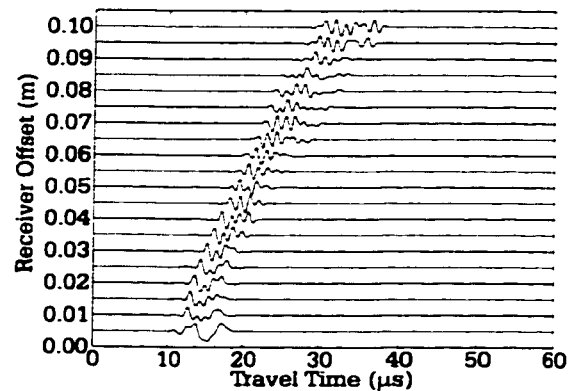


(c) SH mode transducer.

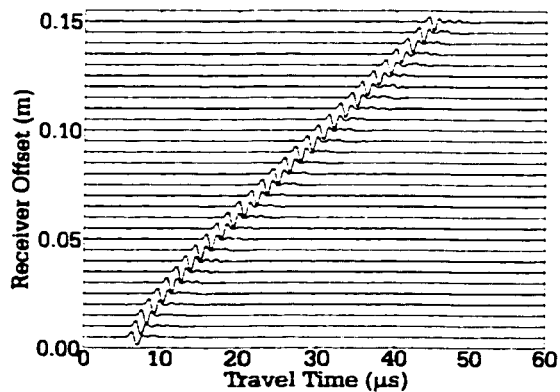
Figure 2.4: Ideal particle motions imparted and received by the transducers.



(a) P source transducer at 2.0 cm depth.



(b) SV source transducer at 4.0 cm depth.



(c) SH source transducer at 2.0 cm depth.

Figure 2.5: Observed amplitude versus time traces with offset on the glass block for various transducers.

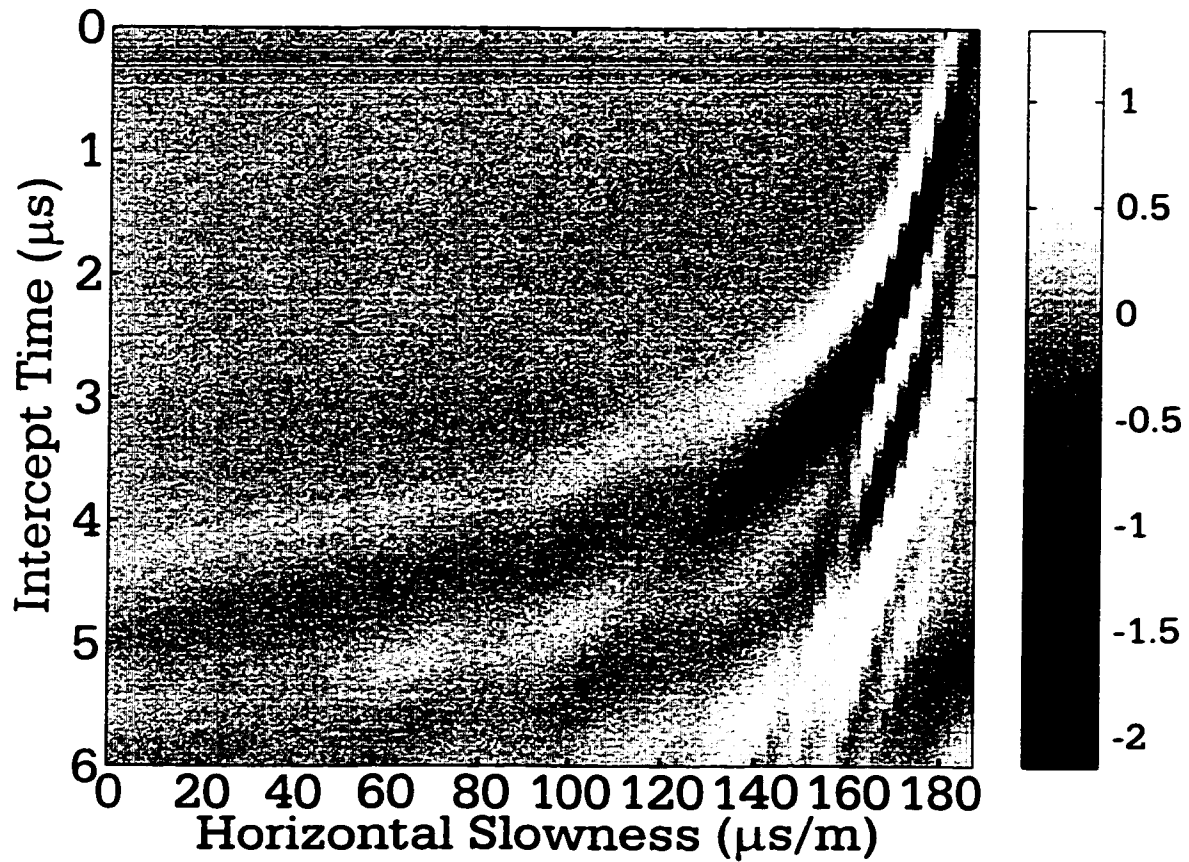


Figure 2.6: The  $\tau - p$  transform obtained by slant-stacking of Figure 2.5a.

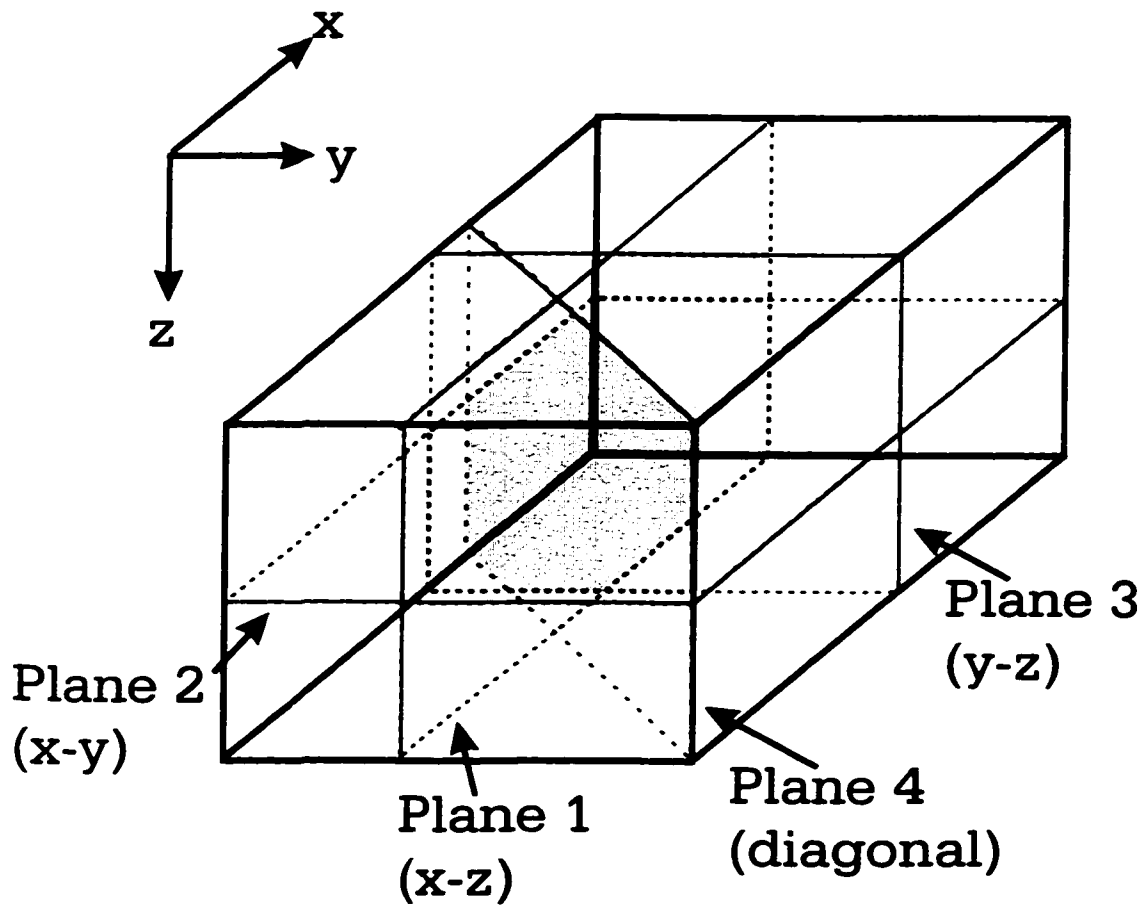
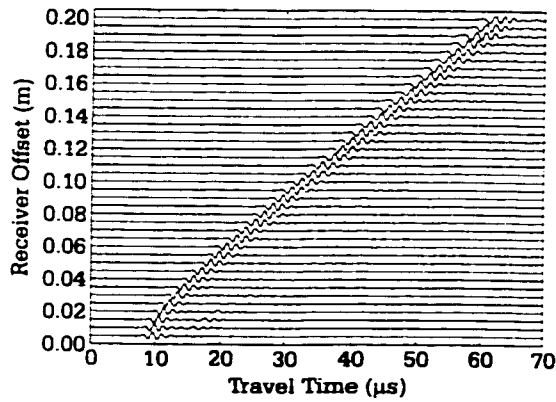
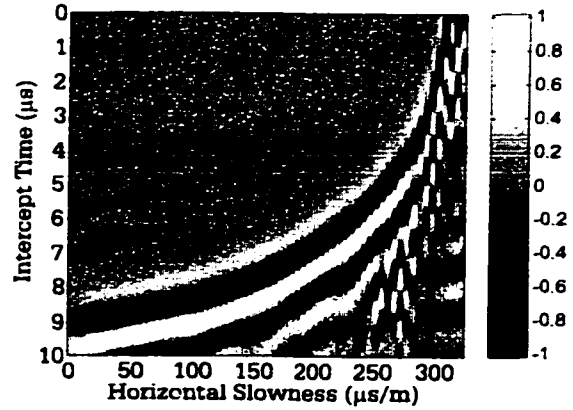


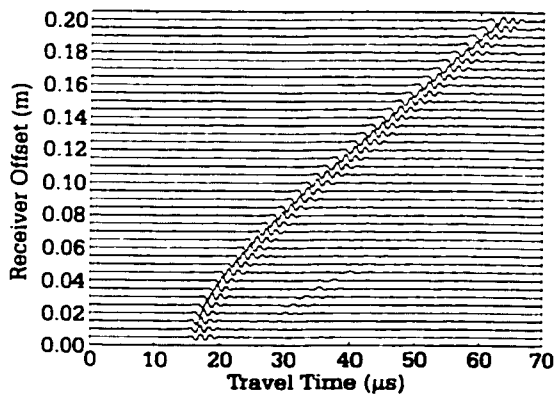
Figure 2.7: The four planes on the composite block in which arrays were prepared and designated as  $x-z$ ,  $x-y$ ,  $y-z$ , and  $xy-z$  (i.e., diagonal).



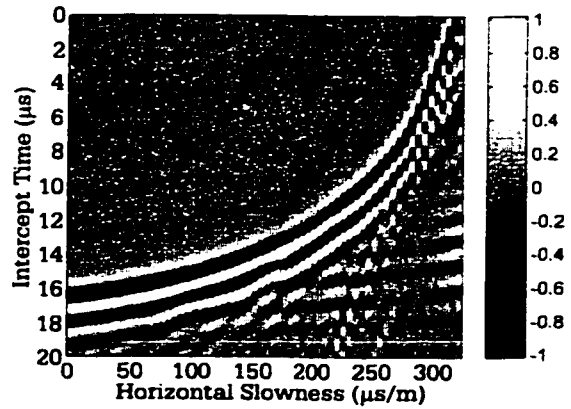
(a) Amplitude versus time traces with offset for the 2.0 cm deep source 1.



(b)  $\tau - p$  transform of a) from which the series of  $\tau_1(p)$  is obtained.

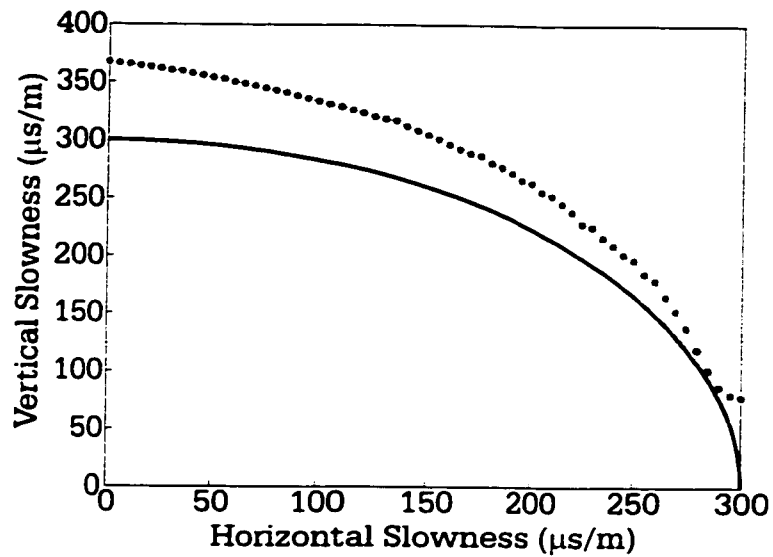


(c) Amplitude versus time traces with offset for the 4.0 cm deep source 2.

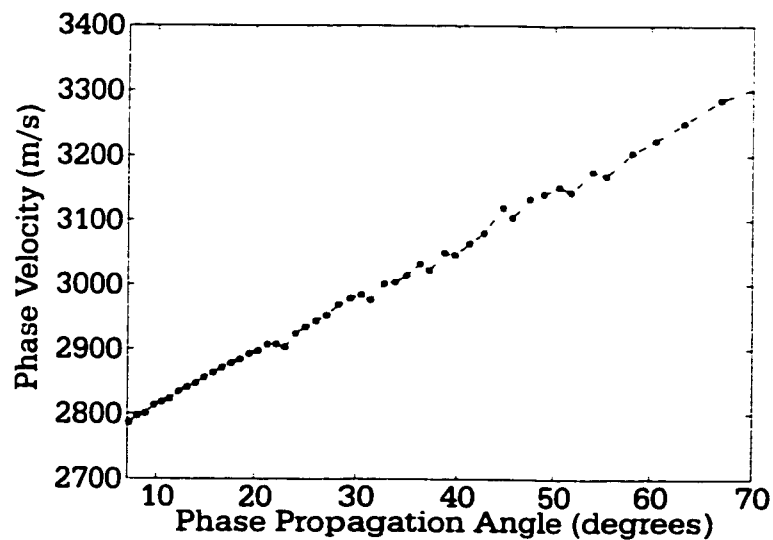


(d)  $\tau - p$  transform of c) from which the series of  $\tau_2(p)$  is obtained.

Figure 2.8: The complete set of P-polarization results from the x-z plane.



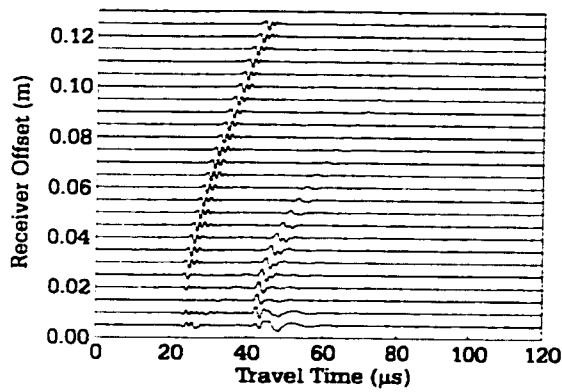
(a) Vertical slowness  $q$  as a function of horizontal slowness  $p$ . the data obtained are indicated by asterisks symbols. the continuous line shown for comparison is the circular  $q - p$  curve that would exist for an isotropic medium.



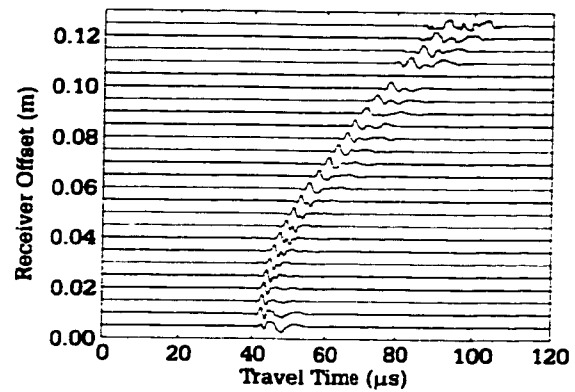
(b) Corresponding P phase velocity versus phase propagation angle  $\theta$ .

Figure 2.9: Slownesses and phase velocities obtained from the  $\tau - p$  transforms of the x-z plane P transducer traces of Figure 2.8.

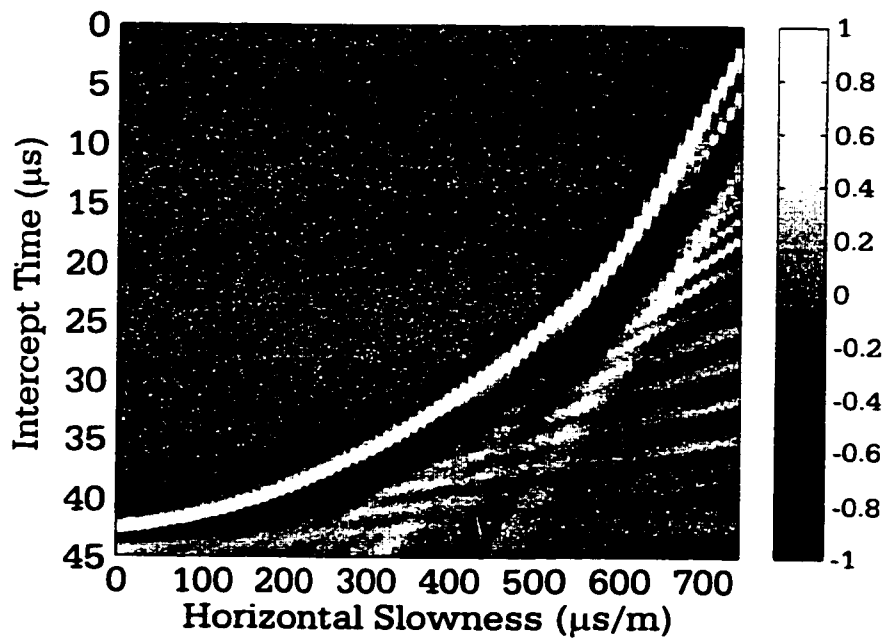




(a) Unmodified SV mode records for the 6.0 cm deep source displaying strong P mode arrivals and transducer directionality effects.

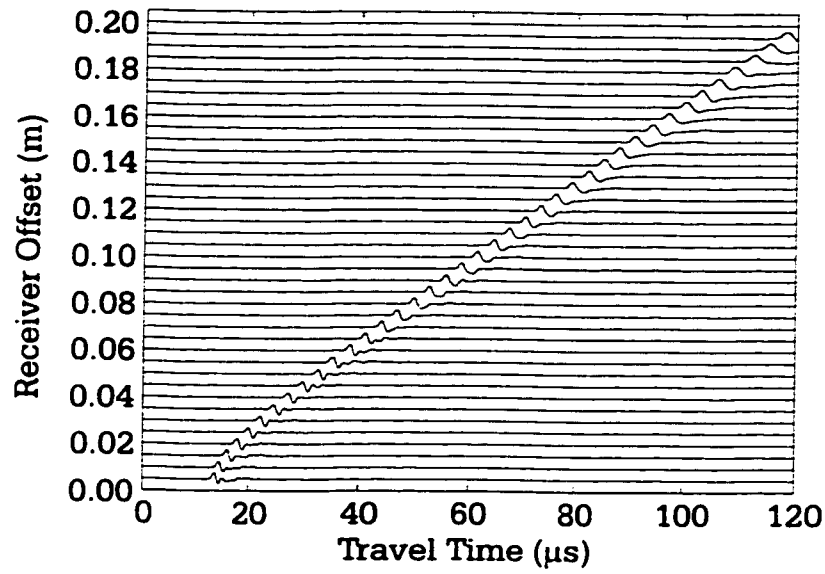


(b) Isolated SV mode arrivals after muting of P mode arrivals followed by peak amplitude normalization.

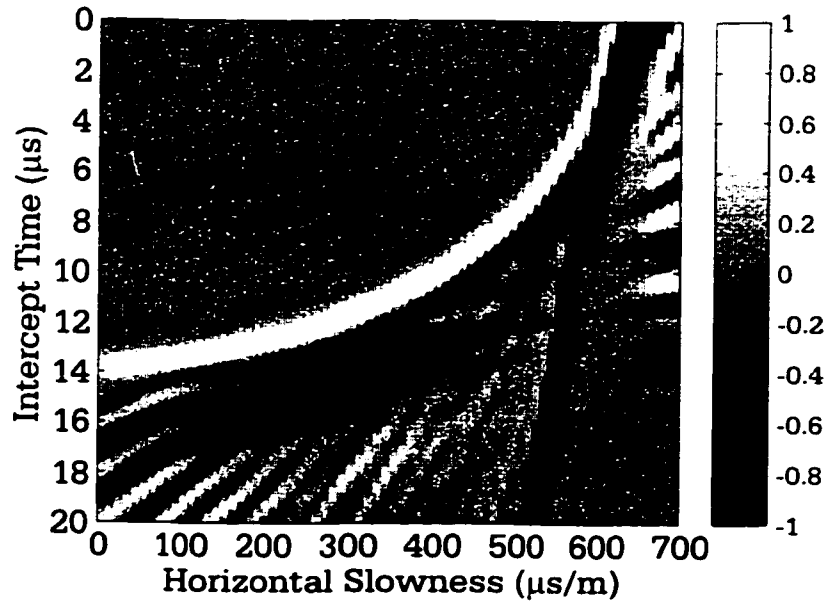


(c) Peak amplitude normalization of the  $\tau - p$  transform via slant-stack of (b).

Figure 2.10: Analysis of x-z plane SV mode arrivals.



(a) The SH mode records for the 2.0 cm deep source.



(b) The corresponding  $\tau - p$  transformation of (a).

Figure 2.11: Analysis of x-z plane SH mode arrivals.

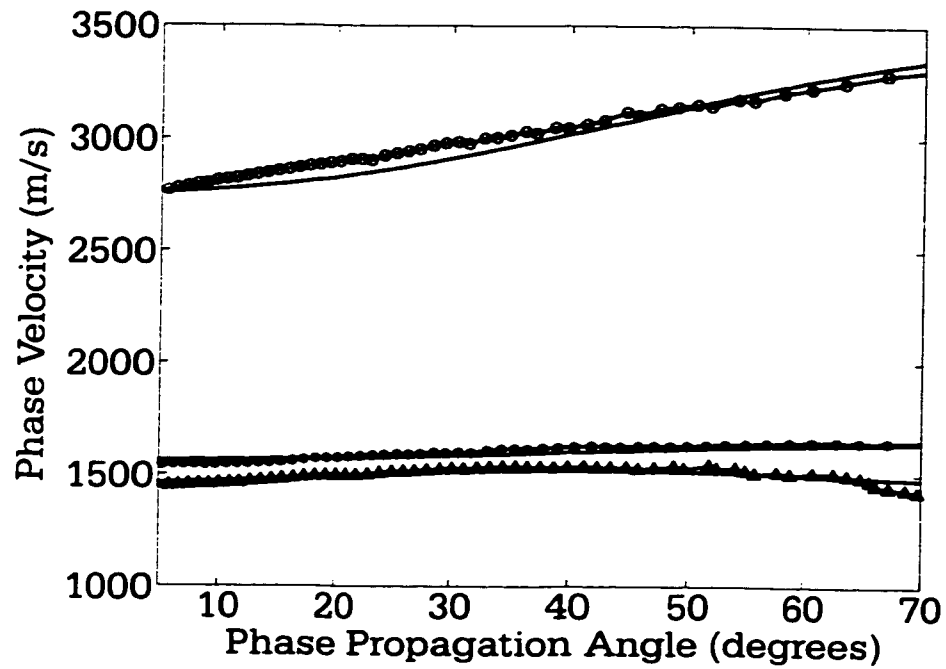


Figure 2.12: Summary of the phase velocities versus propagation angle  $\theta$  obtained from the  $\tau - p$  analysis of the arrivals in the  $x-z$  plane. Symbols represent the P-wave (circles), the SV-wave (triangles), and the SH-wave (asterisks) particle motion polarizations. The angle  $\theta$  is measured from the  $z$ -axis.

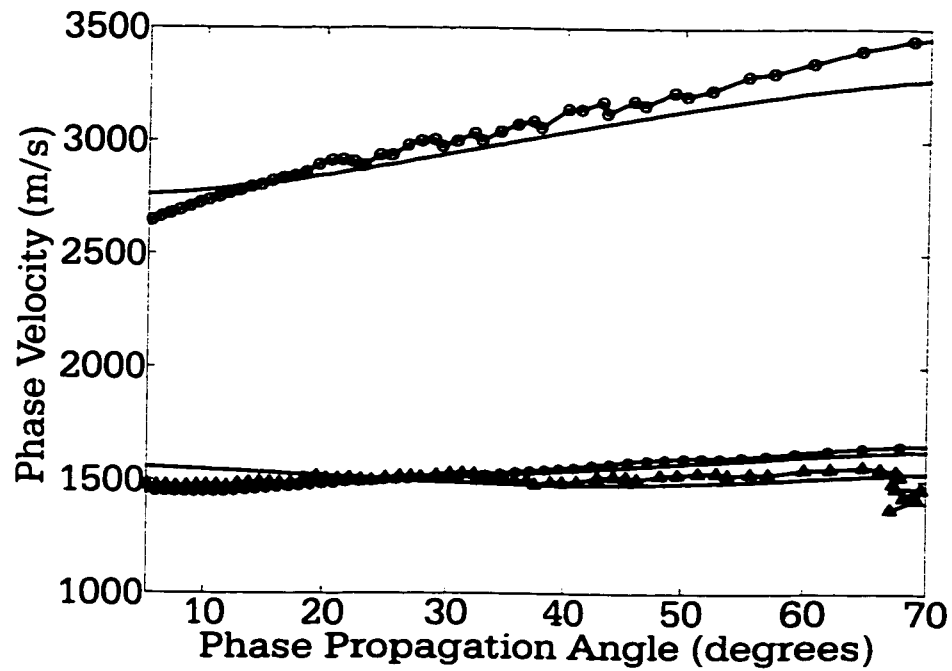


Figure 2.13: Summary of the phase velocities versus propagation angle  $\theta$  obtained from the  $\tau - p$  analysis of the arrivals in the  $y-z$  plane. Symbols represent the P-wave (circles), the SV-wave (triangles), and the SH-wave (asterisks) particle motion polarizations. The angle  $\theta$  is measured from the  $z$ -axis.

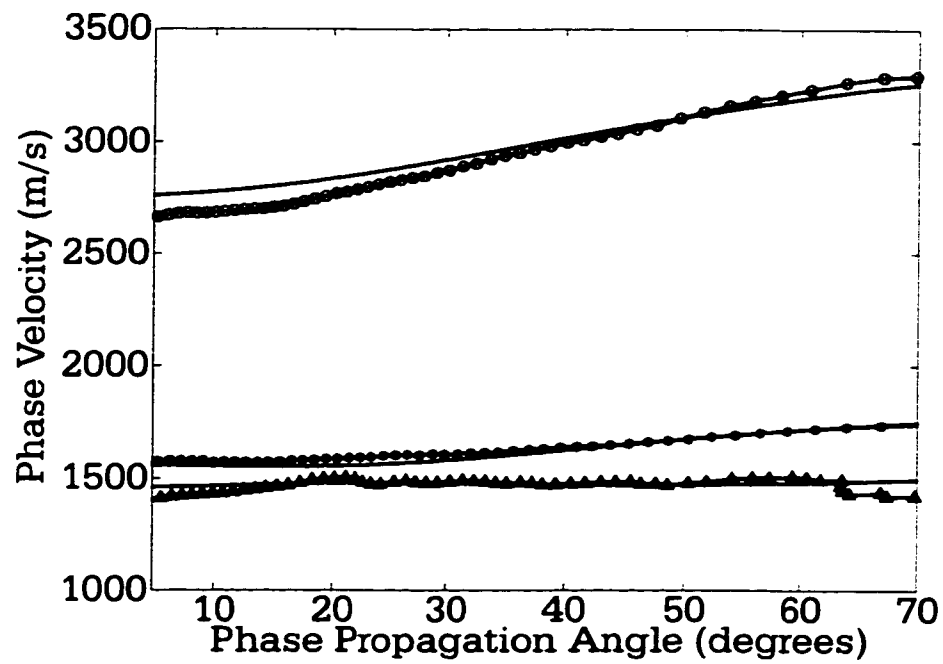


Figure 2.14: Summary of the phase velocities versus propagation angle  $\theta$  obtained from the  $\tau - p$  analysis of the arrivals in the  $xy-z$  plane. Symbols represent the P-wave (circles), the SV-wave (triangles), and the SH-wave (asterisks) particle motion polarizations. The angle  $\theta$  is measured from the  $z$ -axis.

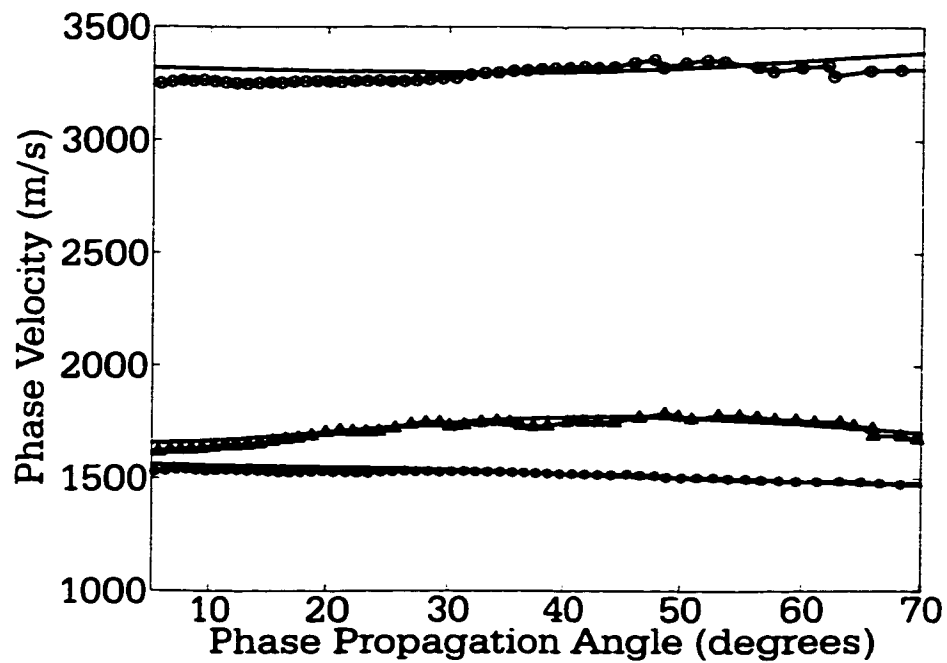


Figure 2.15: Summary of the phase velocities versus propagation angle  $\theta$  obtained from the  $\tau - p$  analysis of the arrivals in the x-y plane. Symbols represent the P-wave (circles), the SV-wave (triangles), and the SH-wave (asterisks) particle motion polarizations. The angle  $\theta$  is measured from the y-axis.

# Chapter 3

## Conclusions

### 3.1 Determination of phase velocities and the elastic coefficients

In this thesis, the technique for determining wave speed anisotropy, first presented by Kebaili & Schmitt (1996) was further extended to include two shear wave modes. The technique was later employed on a block of composite material which was known to be anisotropic by Kebaili & Schmitt (1997). The technique was employed on a similar block of material and the observed results were further inverted to obtain the complete elastic description of the material.

The velocities were determined using Kebaili & Schmitt's (1996) slant-stack technique. To do this the arrival times were measured for two coplanar source-receiver arrays using three differing polarizations in four different planes; this corresponds to 920 source-receiver combinations. The application of the  $\tau - p$  transform to the resulting data sets provided 624 high quality independent phase velocity measurement dependent on the phase propagation angle. Aside from providing a direct measure of the phase or plane wave velocities, usually otherwise difficult or impossible to determine, the slant-stack methodology has a number of additional advantages. First, the measurements can be carried out in a non-destructive manner on relatively easily machined shapes such as

rectangular prisms and cylinders. Second, the slant-stack methodology implicitly contains a degree of averaging over the entire set of waveforms acquired. This stacking help reduce the effects of small heterogeneities within the sample and errors in transducer placement. The advantage of the method in measuring the interval anisotropy in vertical seismic profile (VSP) experiments has already been presented in Kebaili & Schmitt (1996).

Kebaili & Schmitt (1997) measured the P-wave anisotropy only on a similar composite material. The present work included these measurements but extended them with small shear ‘SH’ and ‘SV’ orientation transducers. Under the assumption that the test material (phenolic) has orthorhombic symmetry, the nine independent elastic constants were obtained by a nonlinear least-squares inversion of the observed phase velocities to an uncertainty of better than 2 %. The nonlinear least-squares inversion procedure developed in this work is able to invert for the full 21 independent elastic constants that occur for the triclinic case. Limitations in transducer coverage allowed inversion of the 624 phase velocities only for the orthorhombic case.

An unexpected and additional observation is the waveform spreading or stretching seen with increasing offset. This pulse broadening is symptomatic of a wave speed dispersion and hence attenuation. The effect appeared to be particularly severe for the SV mode propagating in the vertical plane at oblique angles to the layers.

## 3.2 Future Work

There are a number of interesting areas of research made possible with developments in this thesis. Immediate and direct future work should include the acquisition of data in two additional diagonal planes over the existing phenolic sample in order to determine the most general elastic constants for the triclinic



case where no material symmetry is assumed. Such an experiment would confirm whether or not the phenolic sample is truly orthorhombic, or more importantly resolve whether the material can be considered as nearly orthorhombic. After this application of this methodology to synthetic samples, the next logical step would be to apply this methodology to a series of already well-characterized rock. Unfortunately, the elastic properties of rock are often highly dependent on the type of porosity and on the external confining pressure. Further, when rock samples are removed from their native environment, some drilling induced damage and stress relief will tend to damage the core. This may lead to changes in the characteristics of the rock. One way to partially overcome this problem is to carry out the measurements under pressure. Future work should focus on the technical development of the technique in order to make it less cumbersome so that these experiments can be carried out efficiently under confining pressures (to at least 300 MPa) in order to evaluate the effects of anisotropy change with pressure. Many different types of both sedimentary and igneous rocks need be tested.

Another area of future work is studying the properties of rocks in the borehole through the use of vertical seismic profile (VSP) data. The results from the experiments performed under confining pressure should be compared with the results from VSP data in order to determine possible effects caused by removal of the rock samples from their native environment.

On a more fundamental level, it was noted that there is spreading in the waveform with offset. How this spreading of the waveforms with offset affects the  $\tau - p$  transform should be studied, possibly through numerical modeling, in order to better improve the determination of phase velocities.

As mentioned previously, the spreading of the waveform may be due to both dispersion and attenuation. Such effects should be studied theoretically and

supported by numerical modeling. One of the most interesting areas for future application of this technique is in the study of layered media and how elastic waves of various frequencies are influenced by propagation through the medium. One crucial topic relates to what may be observed when the wavelength becomes similar to the thickness of the layer. In such a situation, the material behaviour is no longer employ the existing effective medium theories. When the wavelength of the propagating wavelet approaches or exceeds the layer thickness, one must worry about the scale effects of the propagation through layered media. We hope to make new contributions to the understanding of the trade-off between anisotropy and geological scale.

Anisotropy in rocks may be the result of preferential orientation of mineral grains, the presence of oriented cracks of various sizes, or the occurrence of thin layering. One should investigate how these differing sources of anisotropy contribute to observable effects such as dispersion and attenuation. These differing sources of anisotropy may even contribute to a directional dependence in the dispersion and attenuation. This should be investigated by studying materials with similar symmetry but differing sources of anisotropy. The slant-stack technique developed here is ideal for such studies.

Perhaps most importantly will be the studies of the trade-off between wave velocity anisotropy, dispersion, and scale in layered anisotropic media. A better understanding of the characteristics of elastic waves in this regime is crucial to better interpretation of seismic observations. Some of the results may have implications towards our view of the earth's structure.

## References

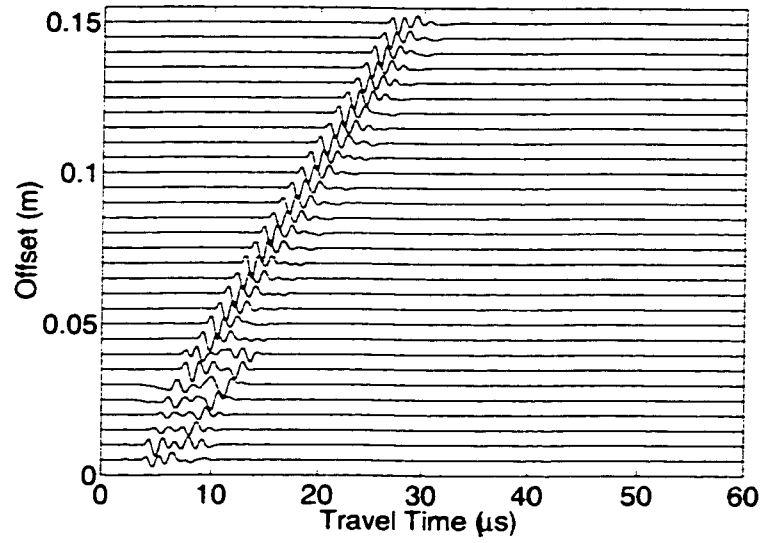
Kebaili, A., and Schmitt, D. R., 1996, Velocity anisotropy observed in well-bore seismic arrivals: Combined effects of intrinsic properties and layering: Geo-

physics, **61**, 12-20.

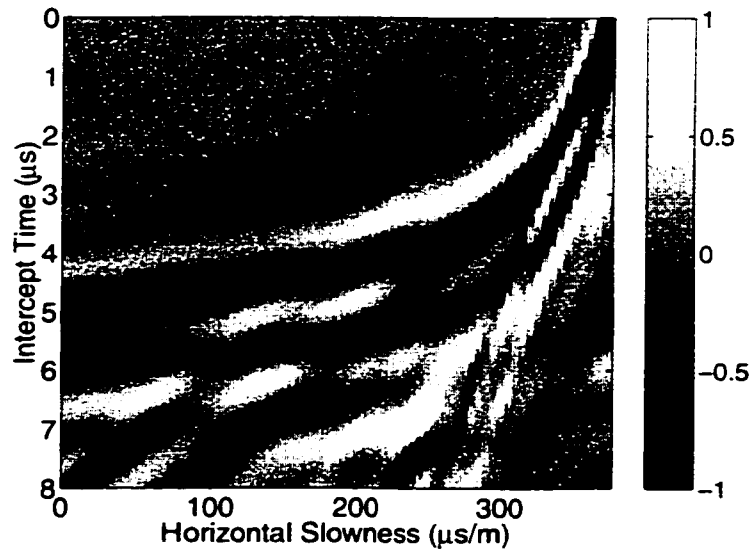
Kebaili, A., and Schmitt, D. R., 1997, Ultrasonic anisotropic phase velocity determination with the Radon transformation: J. Acoust. Soc. Am., **101**, 3278-3286.

# **Appendix A**

**Results from the glass block.**

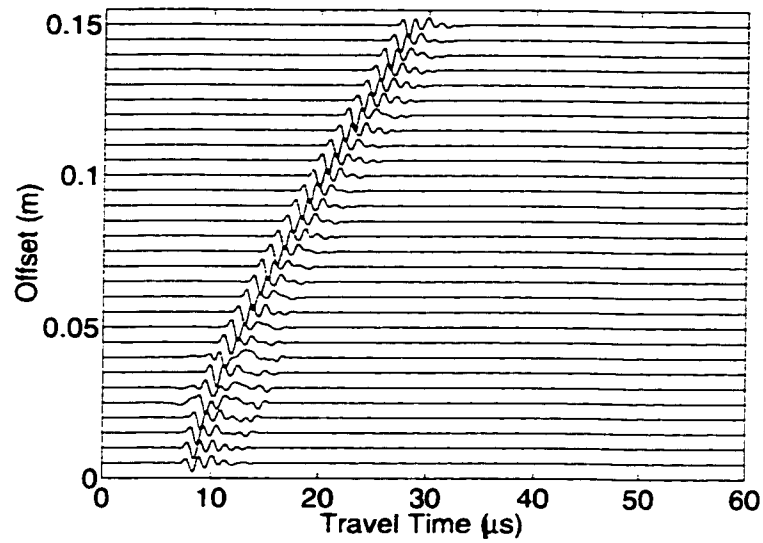


(a) Amplitude versus time traces with offset.

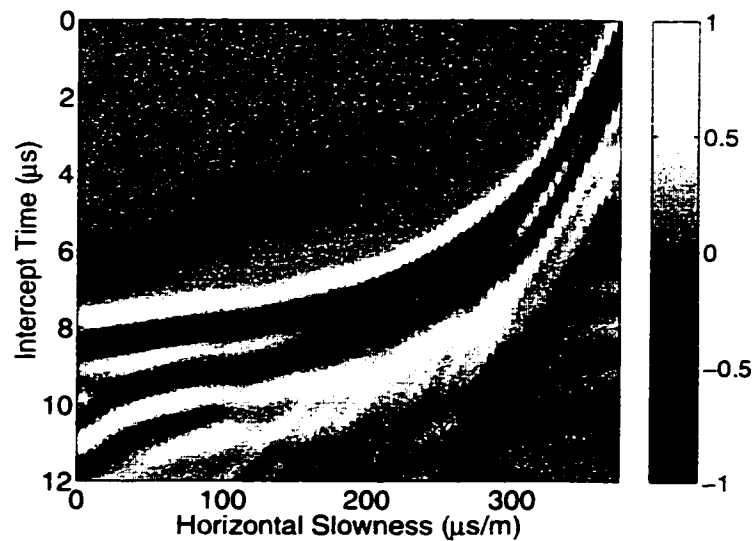


(b) Peak amplitude normalization of the  $\tau - p$  transform via slant-stack of (a).

Figure A.1: P-polarization results from a 2.0 cm depth source on the glass block.

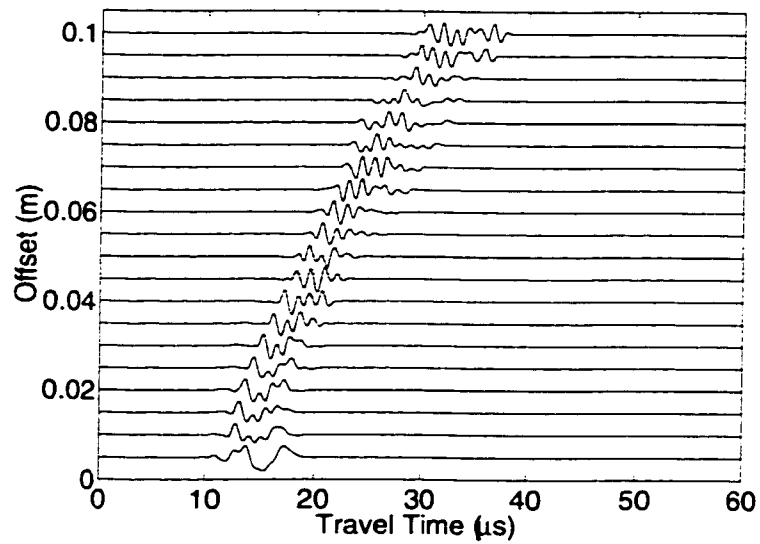


(a) Amplitude versus time traces with offset.



(b) Peak amplitude normalization of the  $\tau - p$  transform via slant-stack of (a).

Figure A.2: P-polarization results from a 4.0 cm depth source on the glass block.



(a) Amplitude versus time traces with offset.

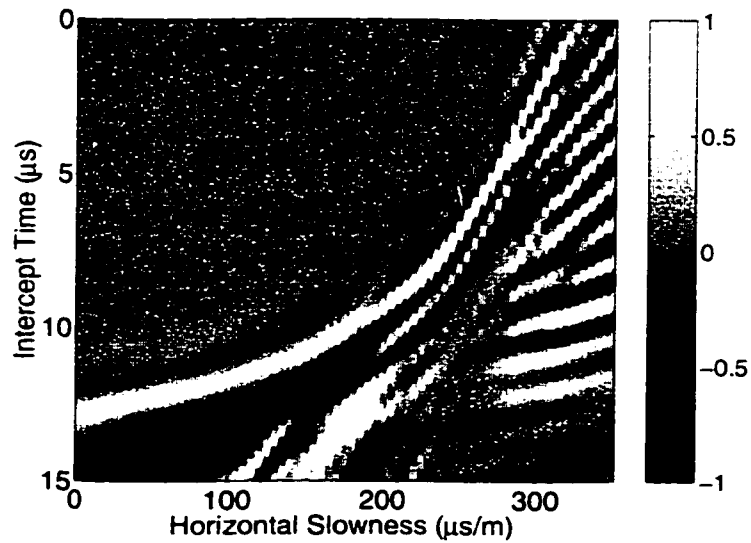
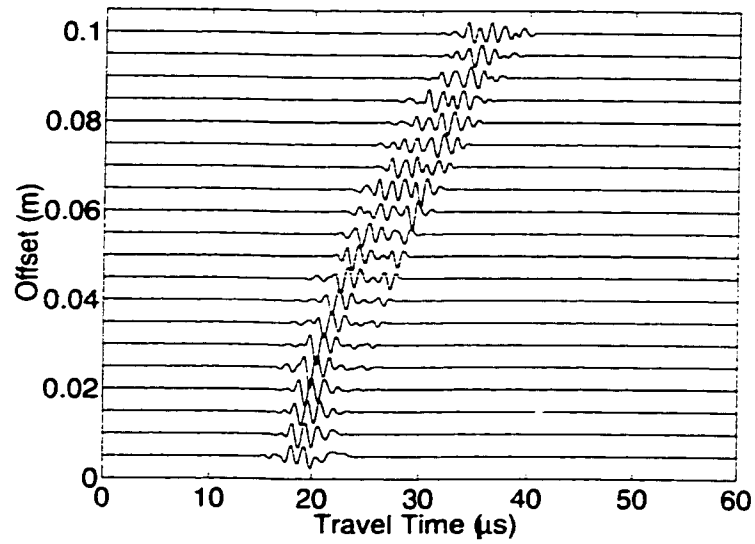
(b) Peak amplitude normalization of the  $\tau - p$  transform via slant-stack of (a).

Figure A.3: SV-polarization results from a 4.0 cm depth source on the glass block.



(a) Amplitude versus time traces with offset.

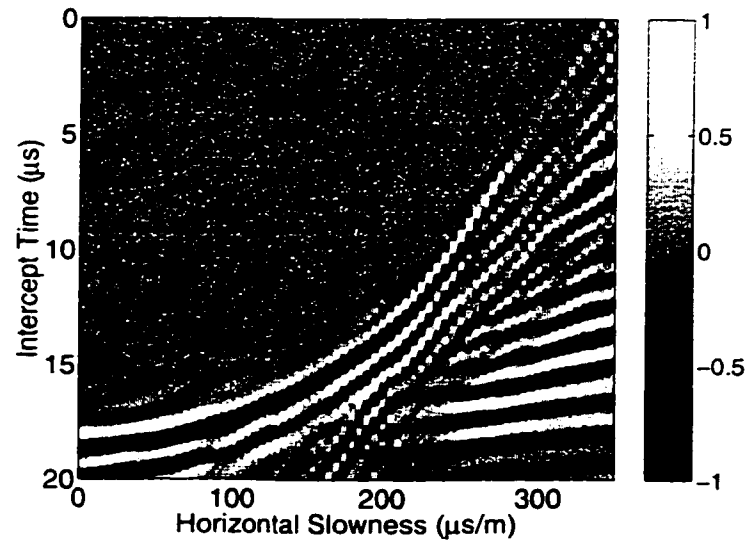
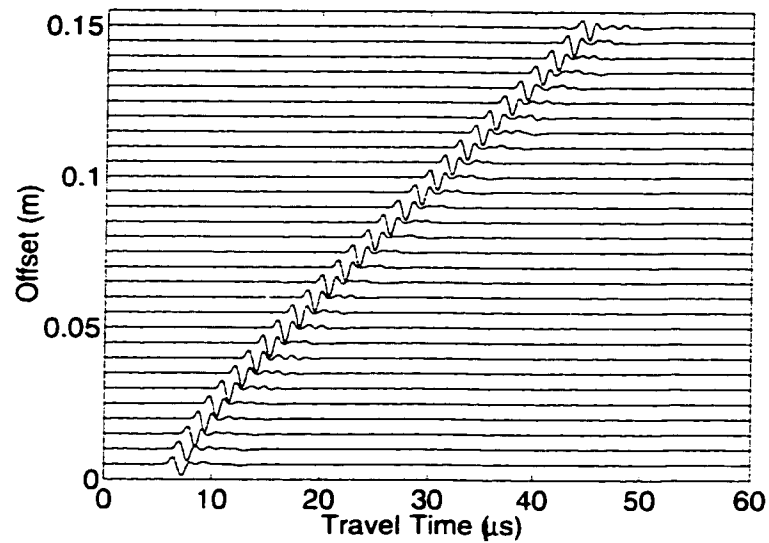
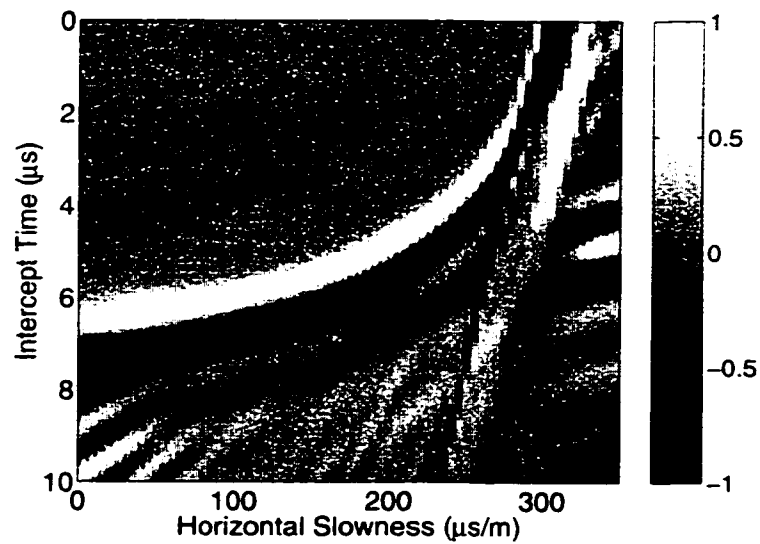
(b) Peak amplitude normalization of the  $\tau - p$  transform via slant-stack of (a).

Figure A.4: SV-polarization results from a 6.0 cm depth source on the glass block.



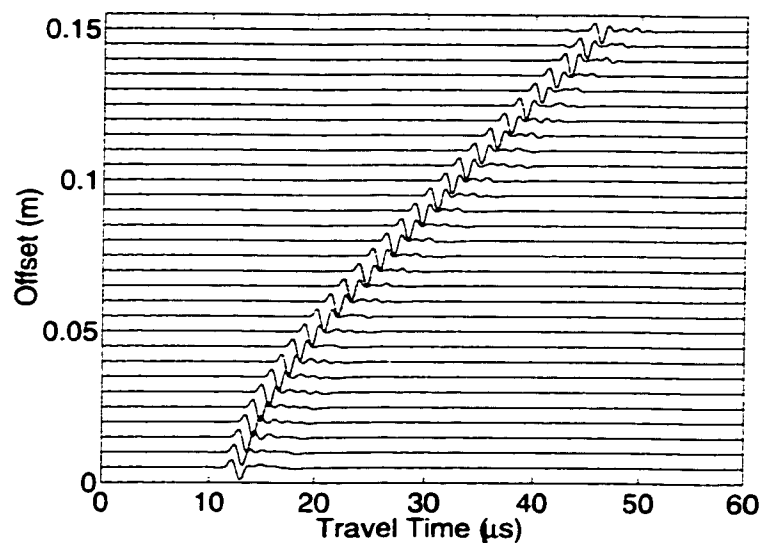


(a) Amplitude versus time traces with offset.



(b) Peak amplitude normalization of the  $\tau - p$  transform via slant-stack of (a).

Figure A.5: SH-polarization results from a 2.0 cm depth source on the glass block.



(a) Amplitude versus time traces with offset.

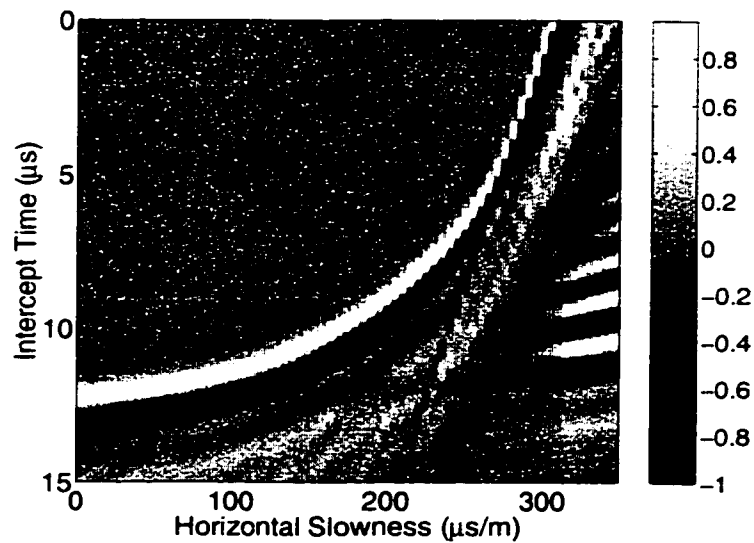
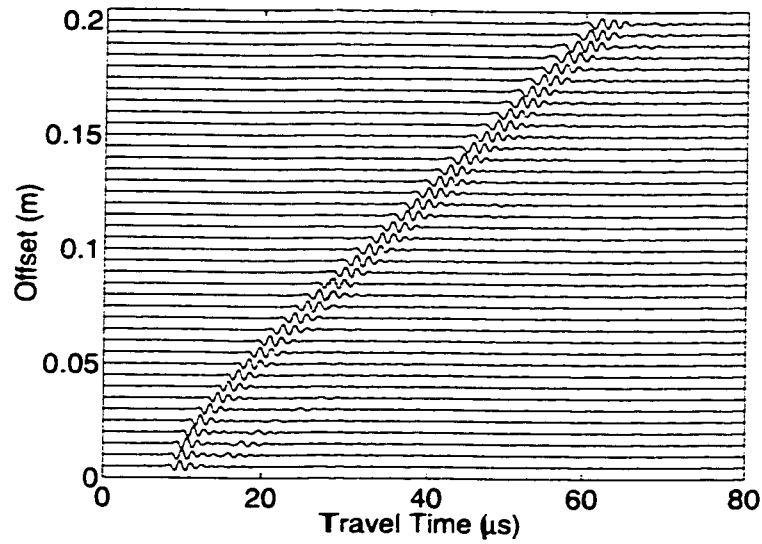
(b) Peak amplitude normalization of the  $\tau - p$  transform via slant-stack of (a).

Figure A.6: SH-polarization results from a 4.0 cm depth source on the glass block.

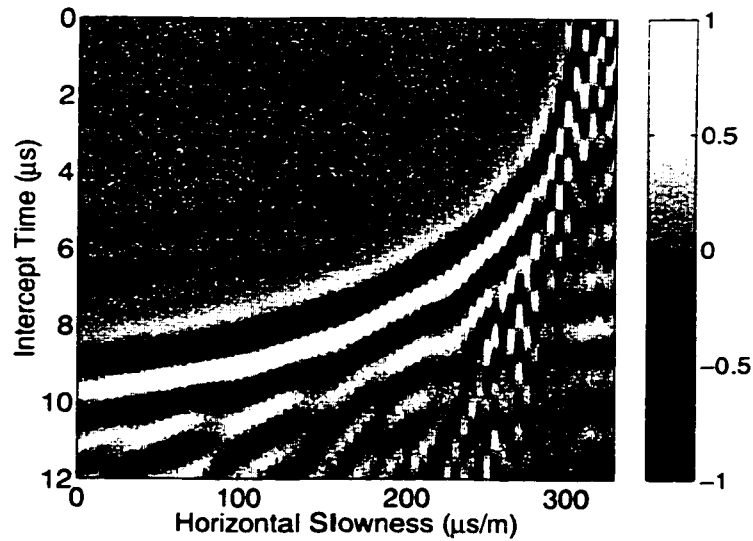
# **Appendix B**

## **Results from the phenolic block.**

### **B.1 x-z plane**

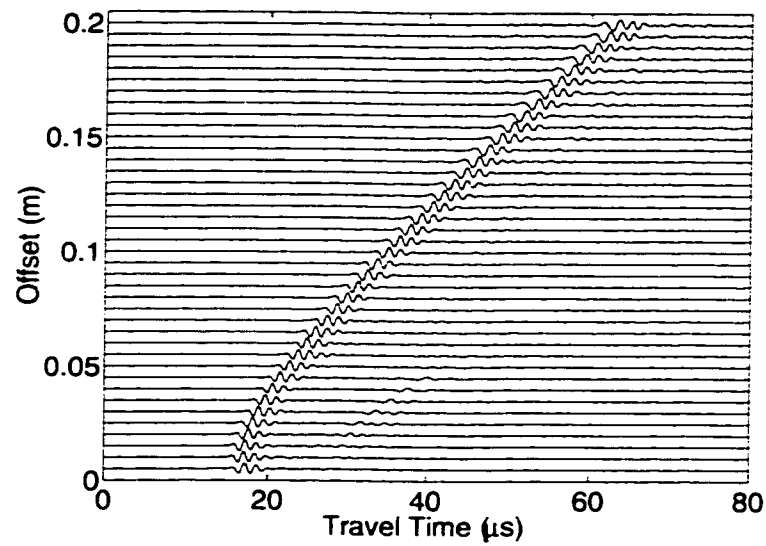


(a) Amplitude versus time traces with offset.



(b) Peak amplitude normalization of the  $\tau - p$  transform via slant-stack of (a).

Figure B.1: P-polarization results from a 2.0 cm depth source on the phenolic block in the x-z plane.



(a) Amplitude versus time traces with offset.

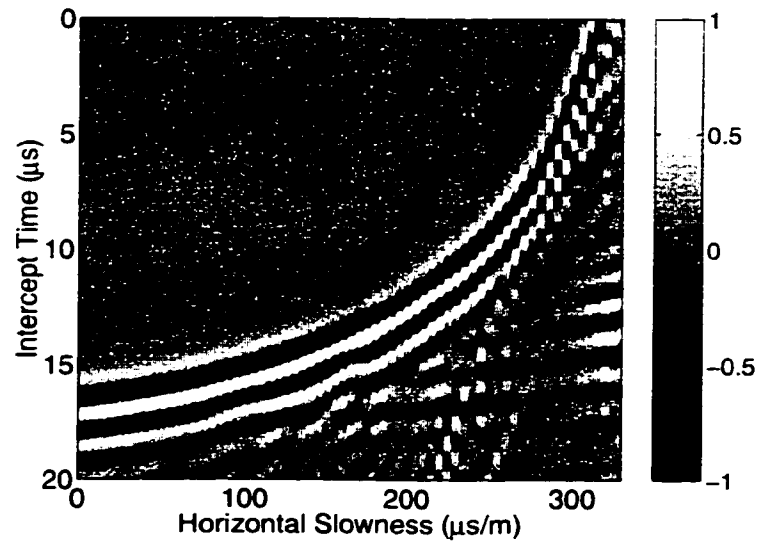
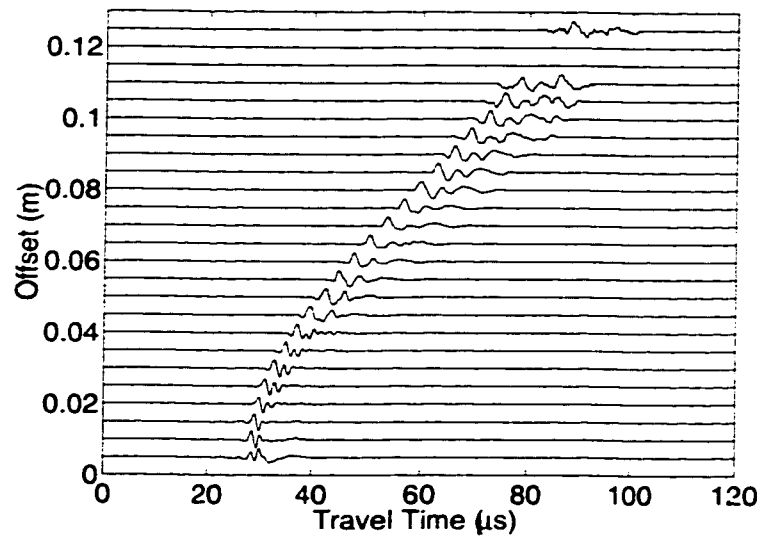
(b) Peak amplitude normalization of the  $\tau - p$  transform via slant-stack of (a).

Figure B.2: P-polarization results from a 4.0 cm depth source on the phenolic block in the x-z plane.



(a) Amplitude versus time traces with offset.

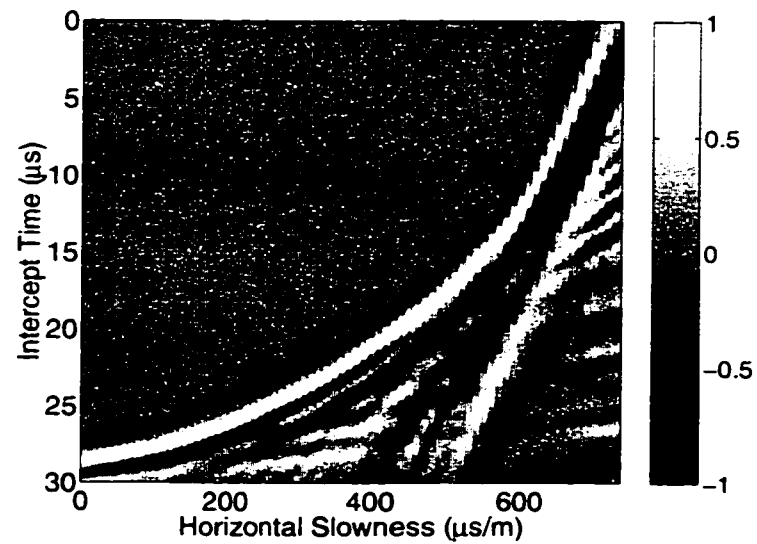
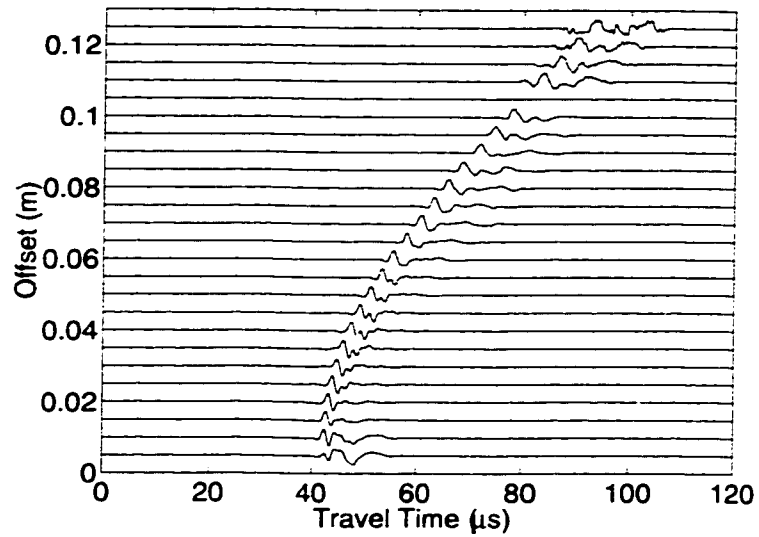
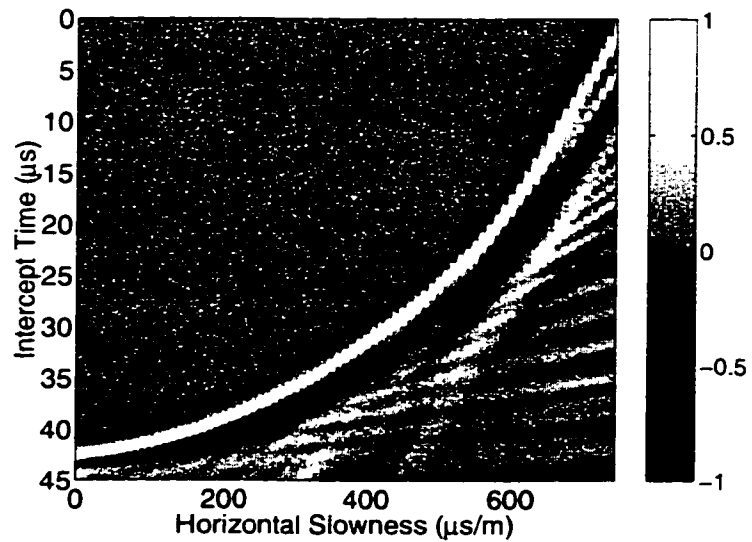
(b) Peak amplitude normalization of the  $\tau - p$  transform via slant-stack of (a).

Figure B.3: SV-polarization results from a 4.0 cm depth source on the phenolic block in the x-z plane.

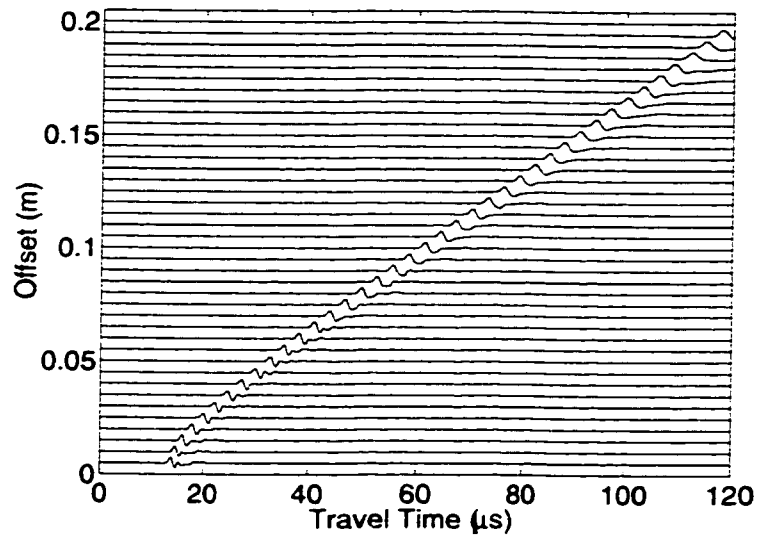


(a) Amplitude versus time traces with offset.



(b) Peak amplitude normalization of the  $\tau - p$  transform via slant-stack of (a).

Figure B.4: SV-polarization results from a 6.0 cm depth source on the phenolic block in the x-z plane.



(a) Amplitude versus time traces with offset.

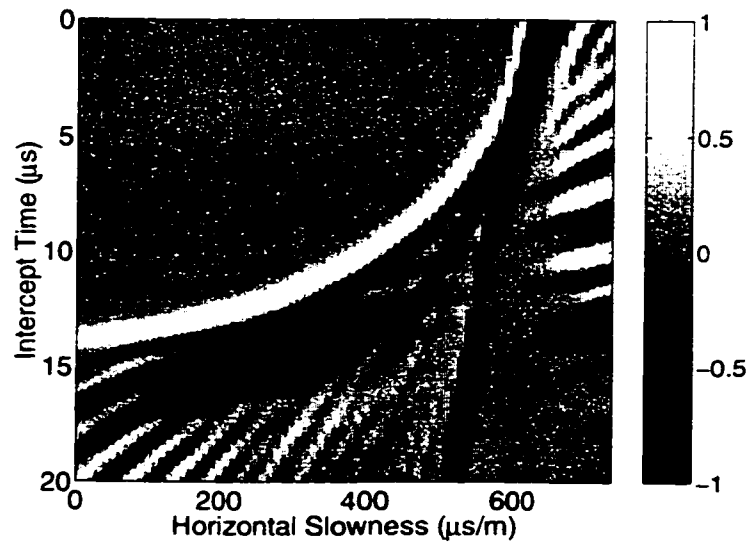
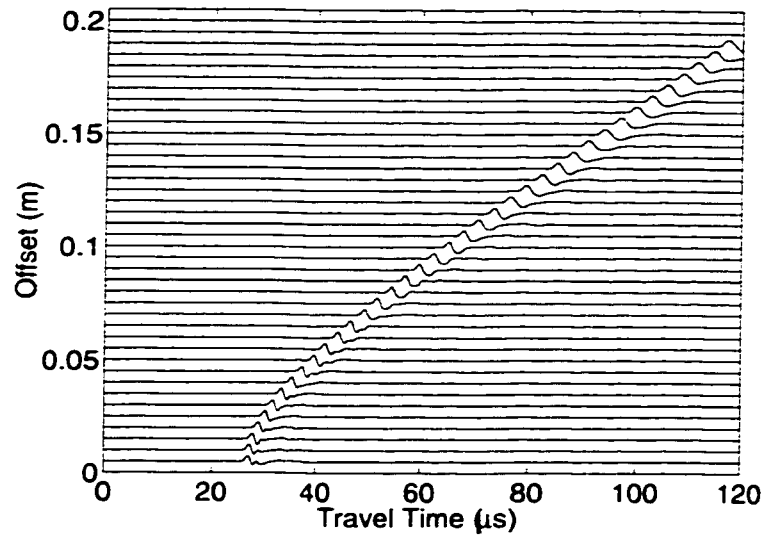
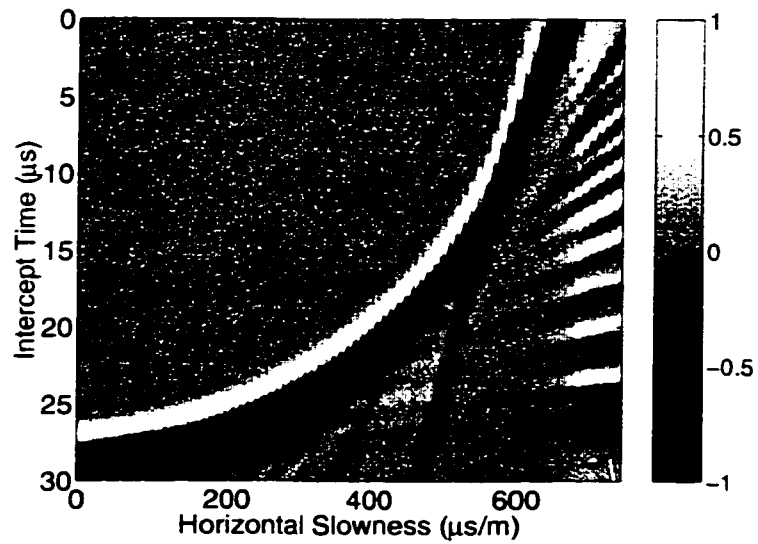
(b) Peak amplitude normalization of the  $\tau - p$  transform via slant-stack of (a).

Figure B.5: SH-polarization results from a 2.0 cm depth source on the phenolic block in the x-z plane.





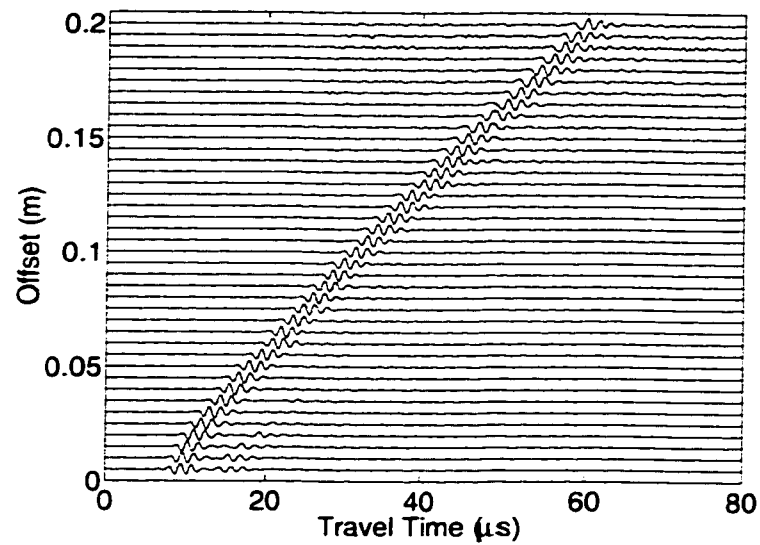
(a) Amplitude versus time traces with offset.



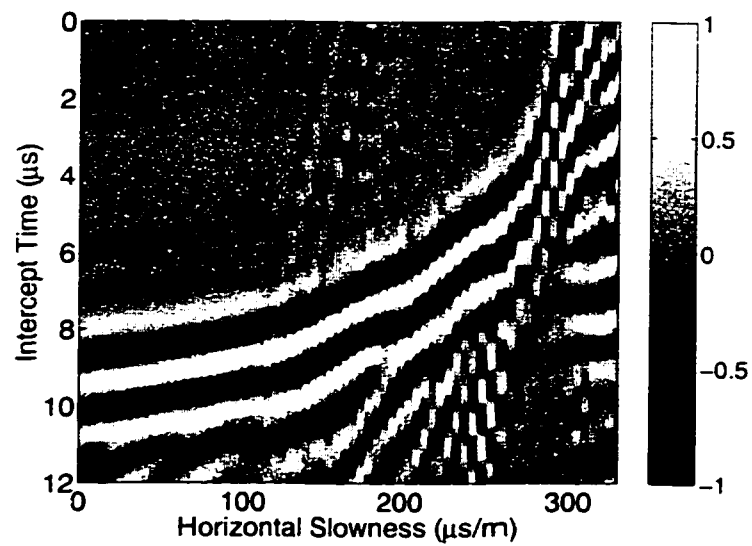
(b) Peak amplitude normalization of the  $\tau - p$  transform via slant-stack of (a).

Figure B.6: SH-polarization results from a 4.0 cm depth source on the phenolic block in the x-z plane.

## **B.2 y-z plane**

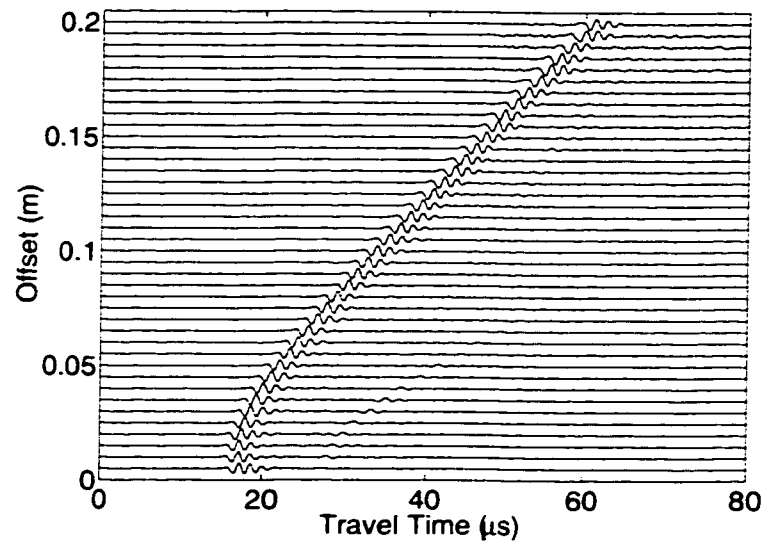


(a) Amplitude versus time traces with offset.

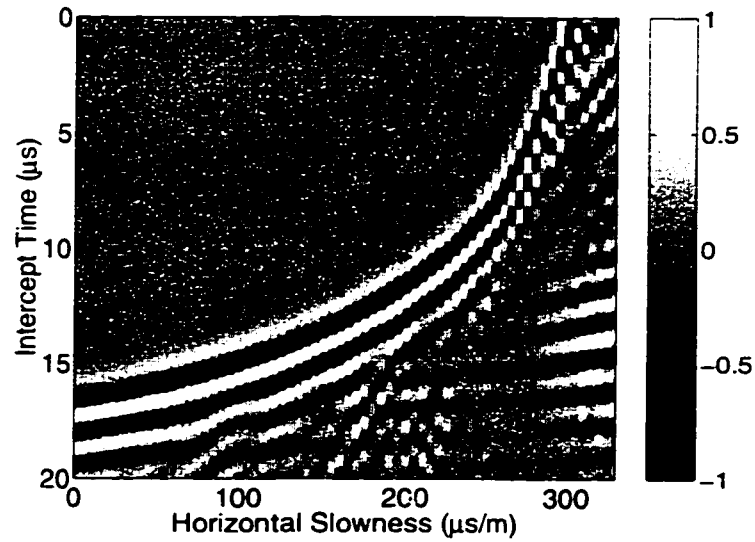


(b) Peak amplitude normalization of the  $\tau - p$  transform via slant-stack of (a).

Figure B.7: P-polarization results from a 2.0 cm depth source on the phenolic block in the y-z plane.

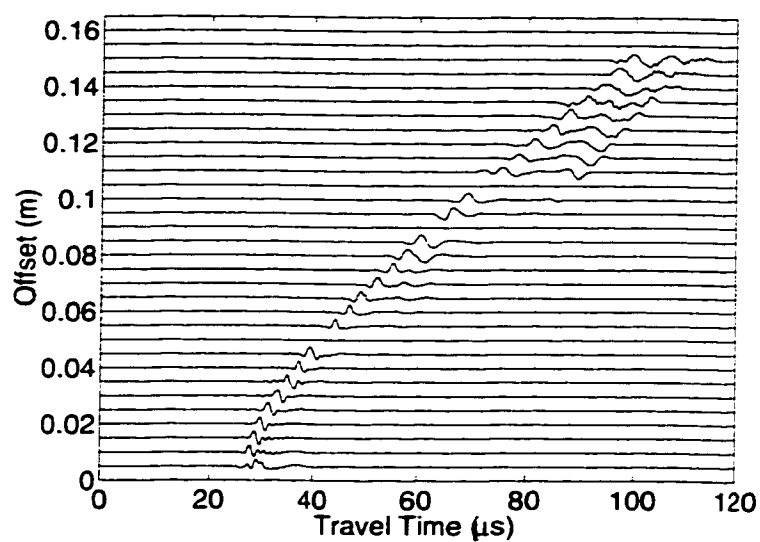


(a) Amplitude versus time traces with offset.



(b) Peak amplitude normalization of the  $\tau - p$  transform via slant-stack of (a).

Figure B.8: P-polarization results from a 4.0 cm depth source on the phenolic block in the y-z plane.



(a) Amplitude versus time traces with offset.

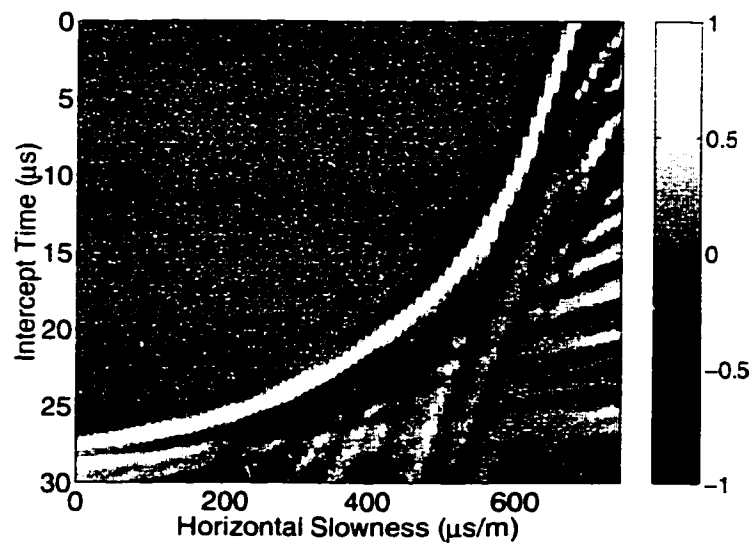
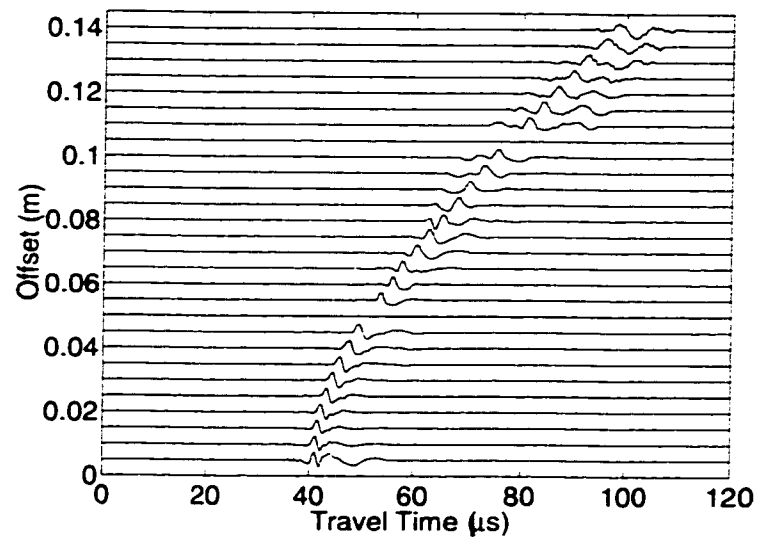
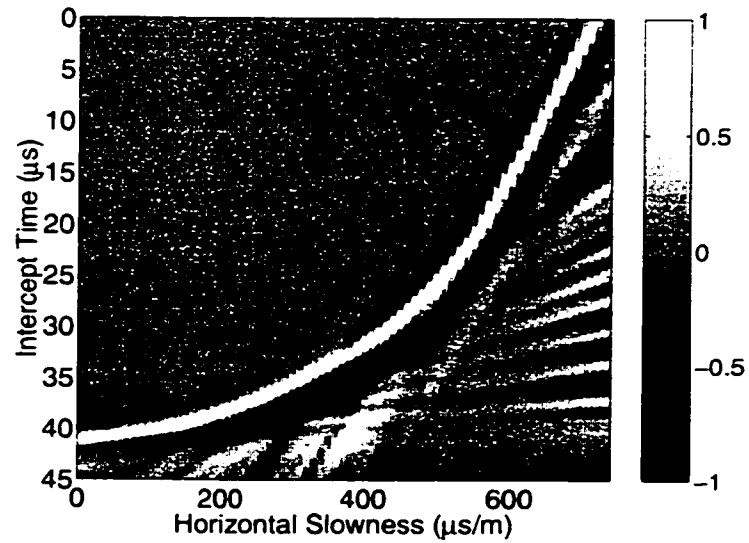
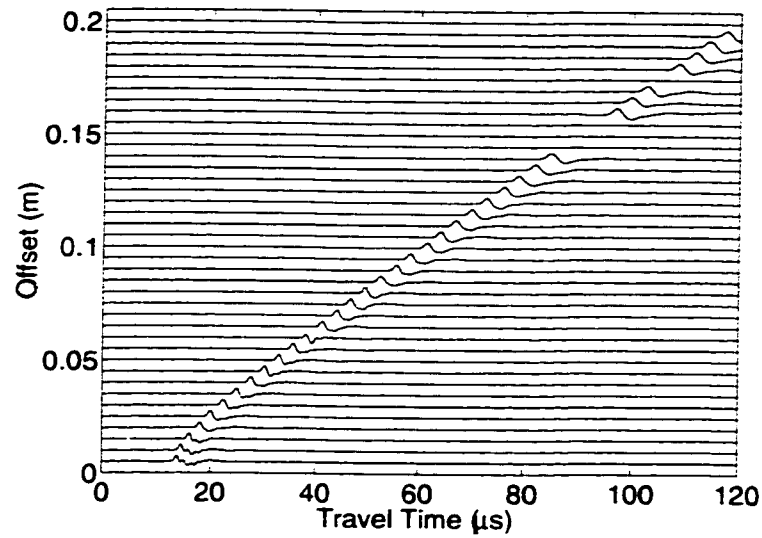
(b) Peak amplitude normalization of the  $\tau - p$  transform via slant-stack of (a).

Figure B.9: SV-polarization results from a 4.0 cm depth source on the phenolic block in the y-z plane.

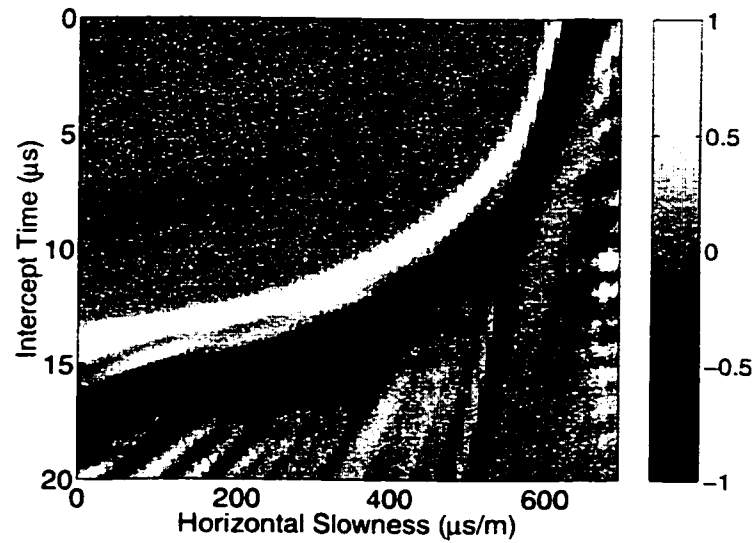


(a) Amplitude versus time traces with offset.

(b) Peak amplitude normalization of the  $\tau - p$  transform via slant-stack of (a).Figure B.10: SV-polarization results from a 6.0 cm depth source on the phenolic block in the  $y-z$  plane.

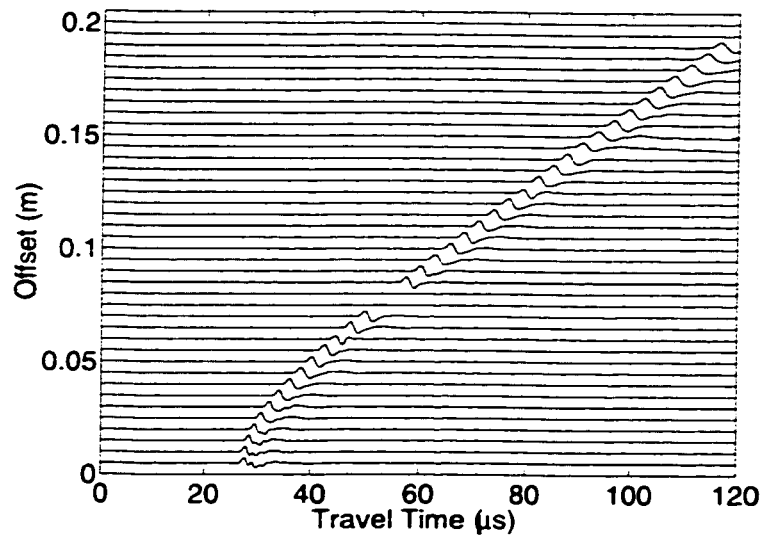


(a) Amplitude versus time traces with offset.

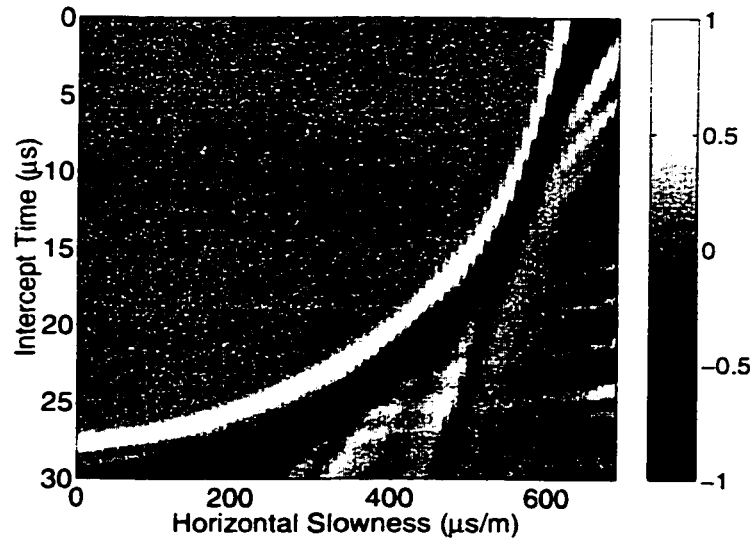


(b) Peak amplitude normalization of the  $\tau - p$  transform via slant-stack of (a).

Figure B.11: SH-polarization results from a 2.0 cm depth source on the phenolic block in the y-z plane.



(a) Amplitude versus time traces with offset.

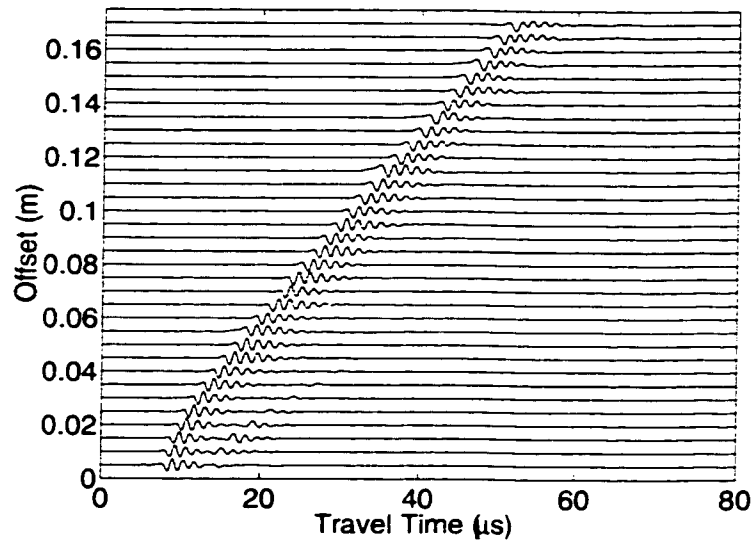


(b) Peak amplitude normalization of the  $\tau - p$  transform via slant-stack of (a).

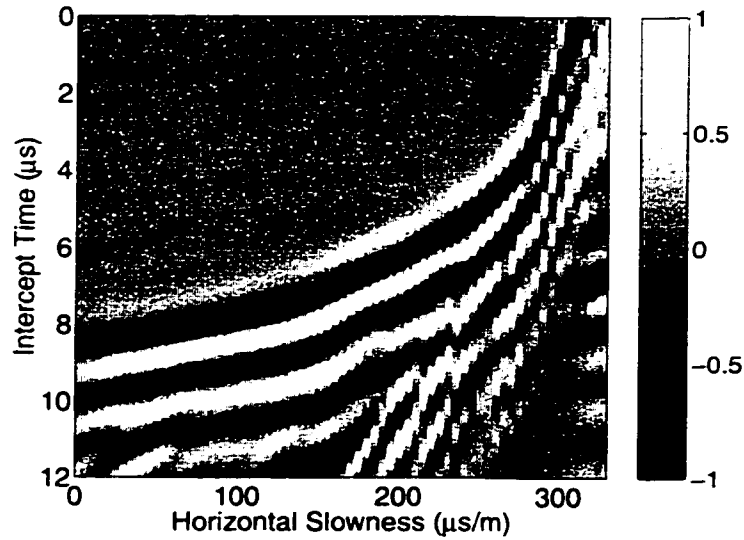
Figure B.12: SH-polarization results from a 4.0 cm depth source on the phenolic block in the  $y-z$  plane.



### **B.3 xy-z plane**

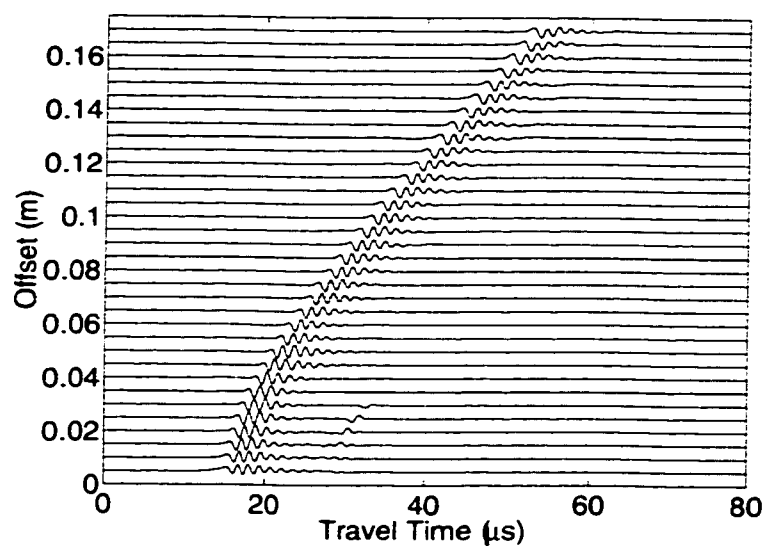


(a) Amplitude versus time traces with offset.

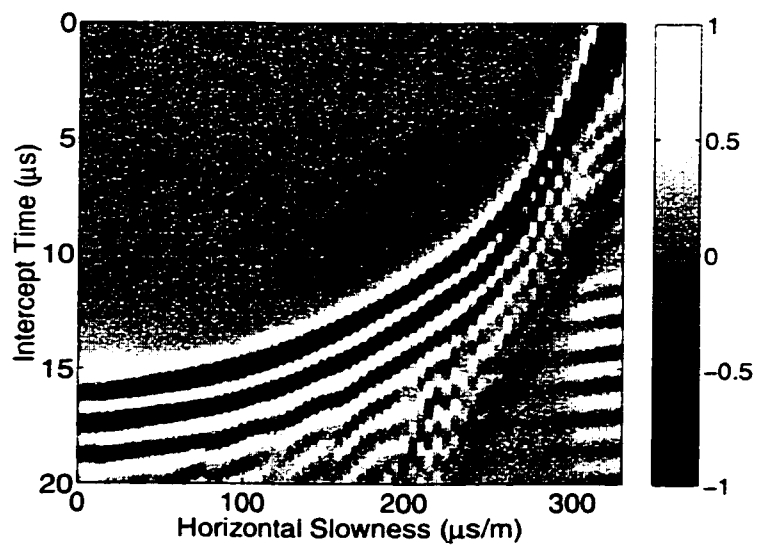


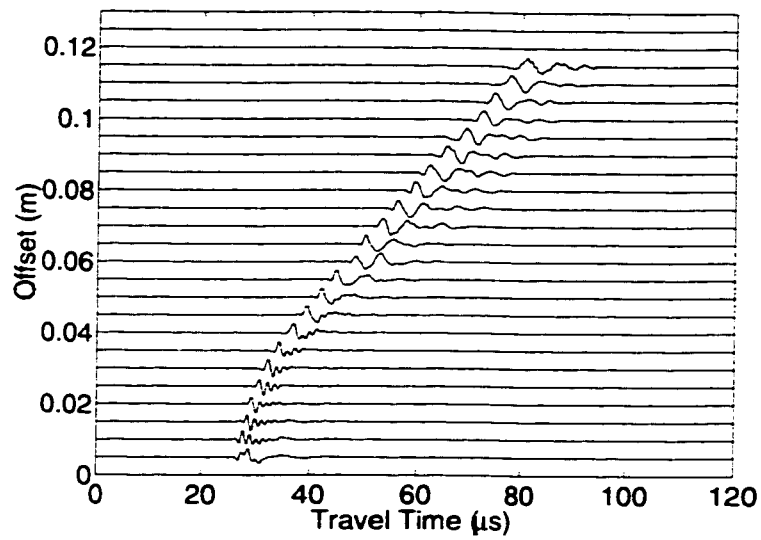
(b) Peak amplitude normalization of the  $\tau - p$  transform via slant-stack of (a).

Figure B.13: P-polarization results from a 2.0 cm depth source on the phenolic block in the xy-z plane.

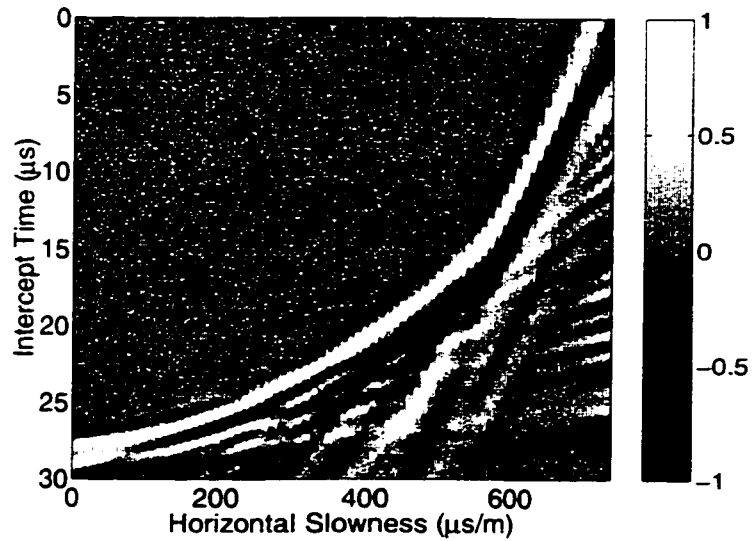


(a) Amplitude versus time traces with offset.

(b) Peak amplitude normalization of the  $\tau - p$  transform via slant-stack of (a).Figure B.14: P-polarization results from a 4.0 cm depth source on the phenolic block in the  $xy$ - $z$  plane.

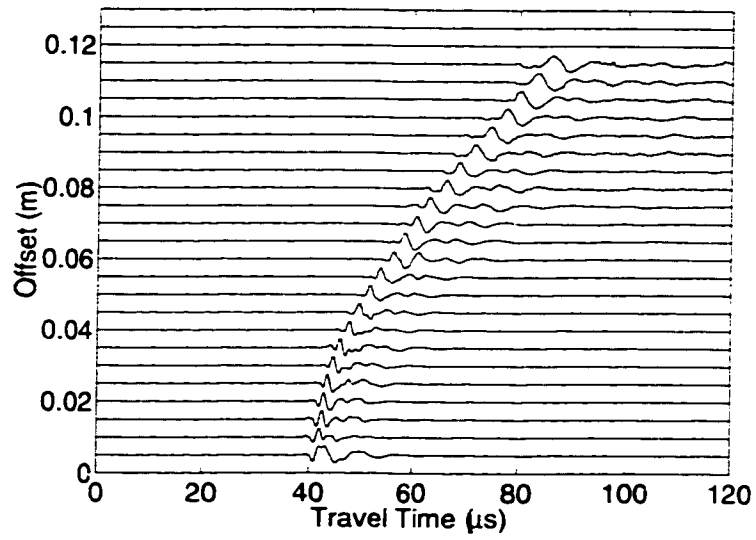


(a) Amplitude versus time traces with offset.

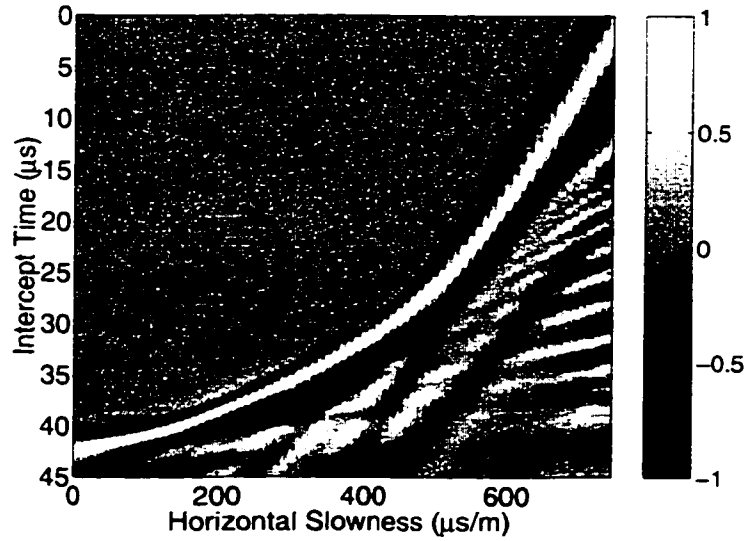


(b) Peak amplitude normalization of the  $\tau - p$  transform via slant-stack of (a).

Figure B.15: SV-polarization results from a 4.0 cm depth source on the phenolic block in the  $xy-z$  plane.

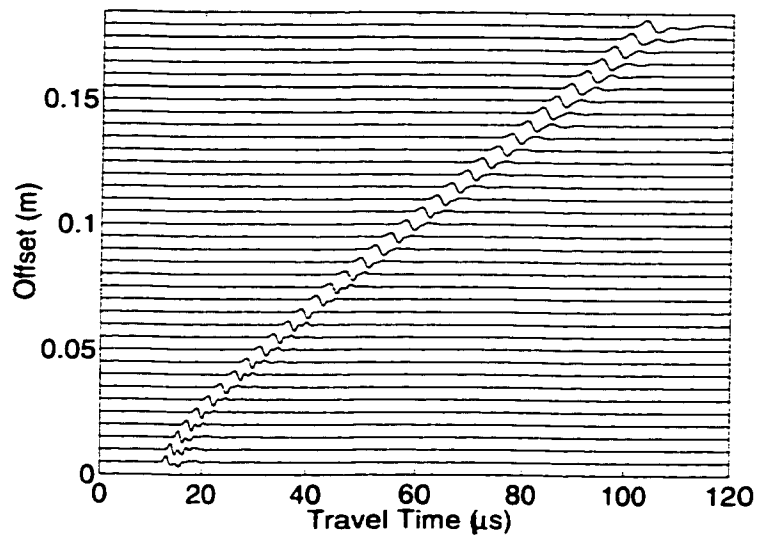


(a) Amplitude versus time traces with offset.

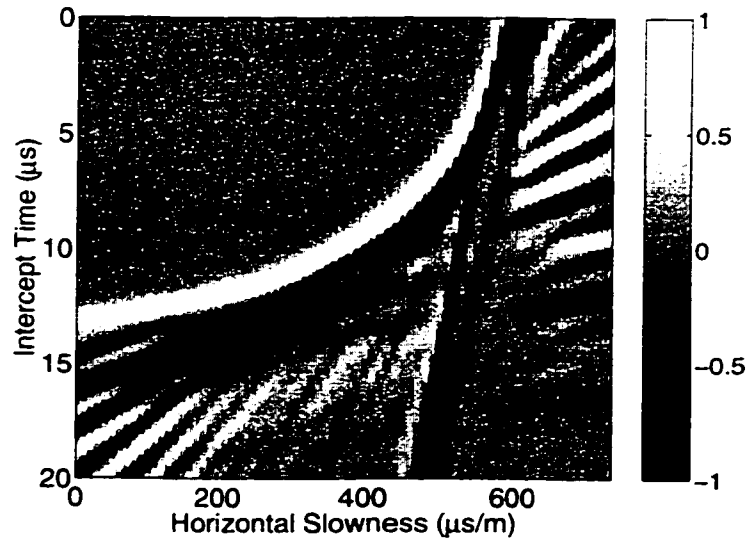


(b) Peak amplitude normalization of the  $\tau - p$  transform via slant-stack of (a).

Figure B.16: SV-polarization results from a 6.0 cm depth source on the phenolic block in the xy-z plane.

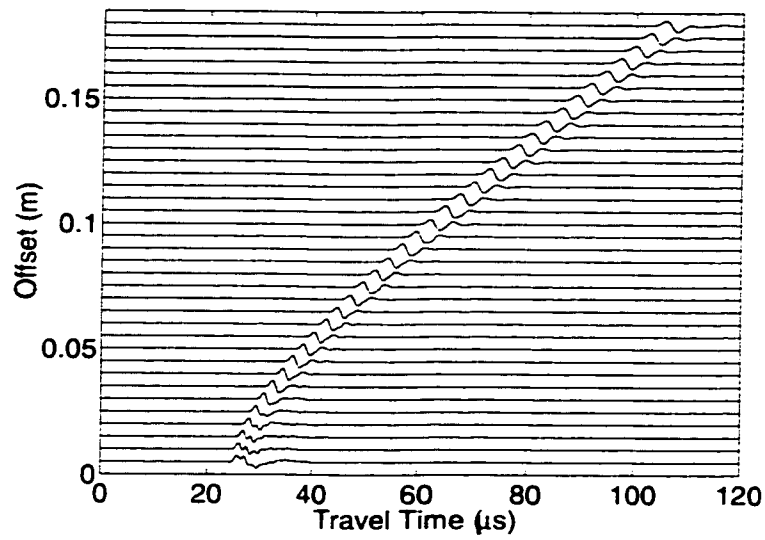


(a) Amplitude versus time traces with offset.

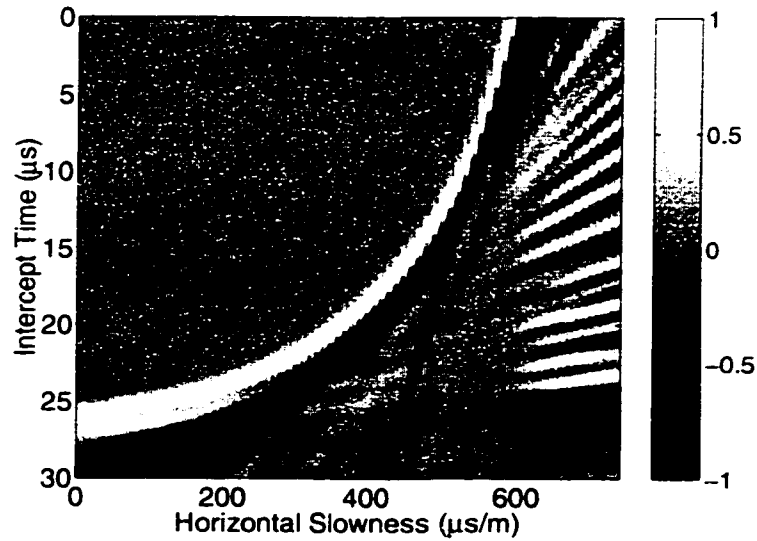


(b) Peak amplitude normalization of the  $\tau - p$  transform via slant-stack of (a).

Figure B.17: SH-polarization results from a 2.0 cm depth source on the phenolic block in the  $xy-z$  plane.



(a) Amplitude versus time traces with offset.

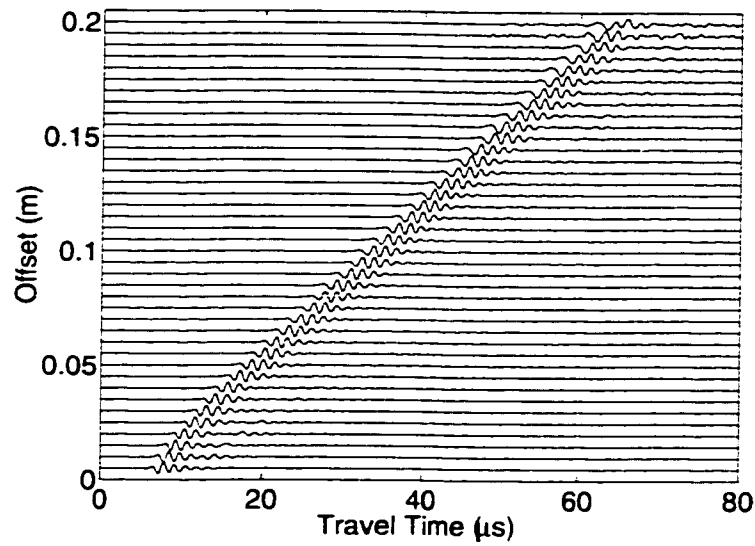


(b) Peak amplitude normalization of the  $\tau - p$  transform via slant-stack of (a).

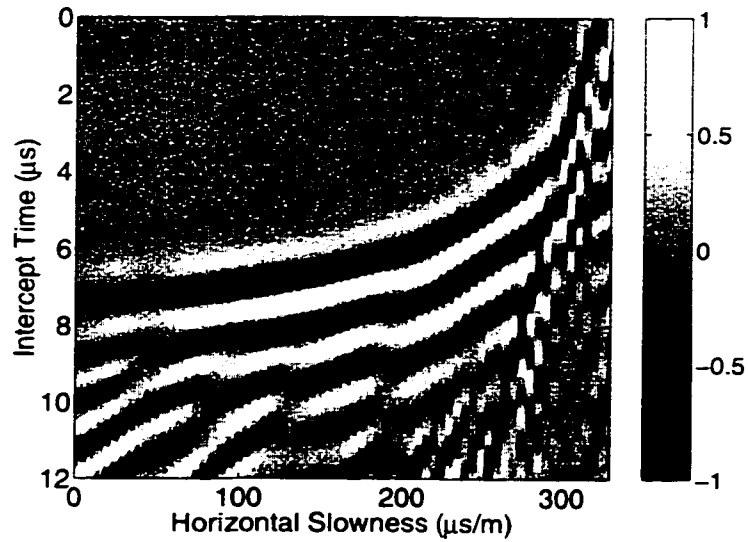
Figure B.18: SH-polarization results from a 4.0 cm depth source on the phenolic block in the  $xy-z$  plane.

## **B.4 x-y plane**



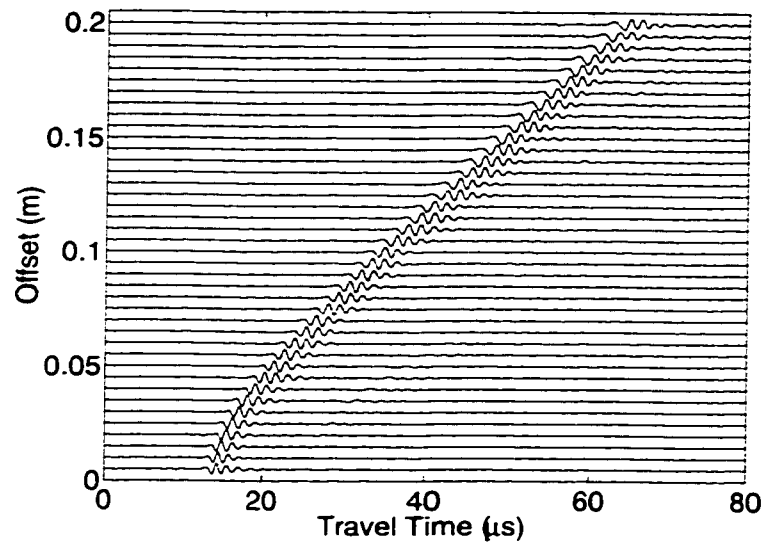


(a) Amplitude versus time traces with offset.

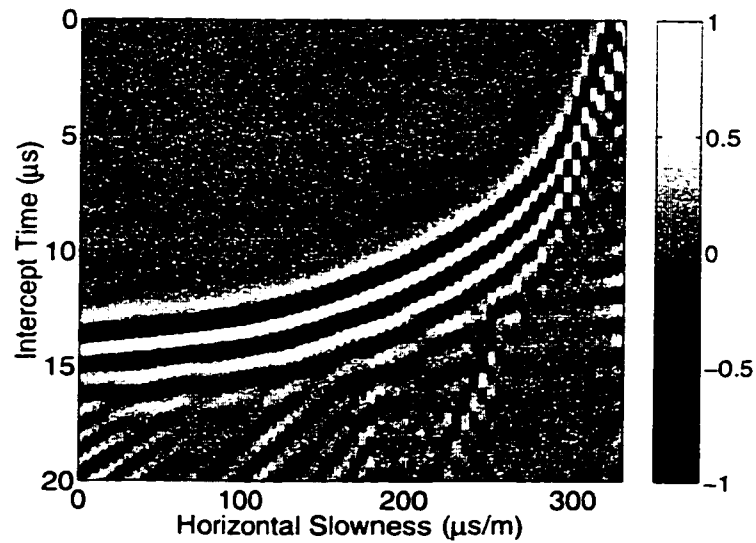


(b) Peak amplitude normalization of the  $\tau - p$  transform via slant-stack of (a).

Figure B.19: P-polarization results from a 2.0 cm depth source on the phenolic block in the x-y plane.

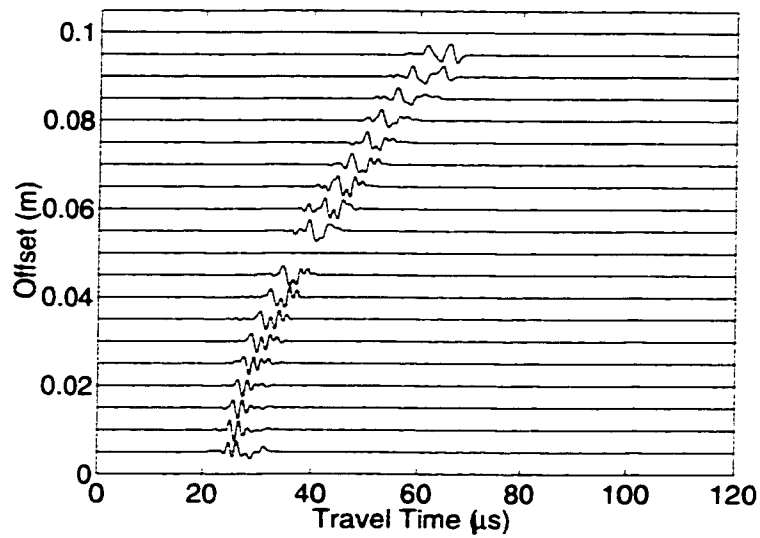


(a) Amplitude versus time traces with offset.

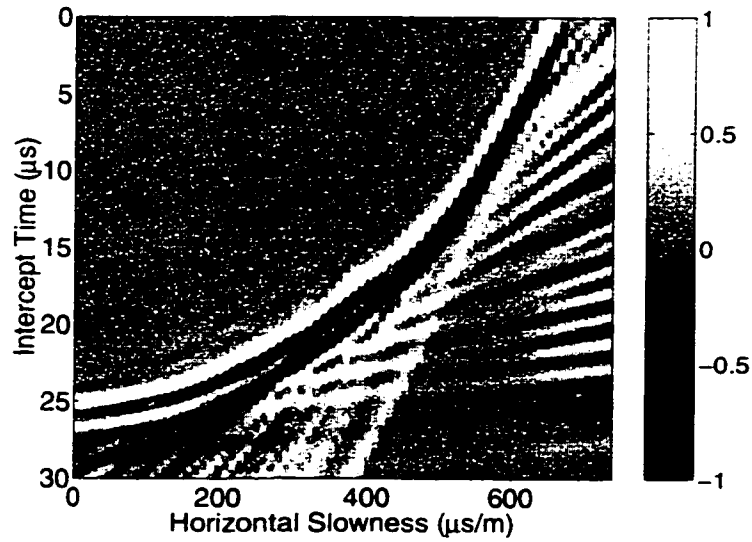


(b) Peak amplitude normalization of the  $\tau - p$  transform via slant-stack of (a).

Figure B.20: P-polarization results from a 4.0 cm depth source on the phenolic block in the x-y plane.

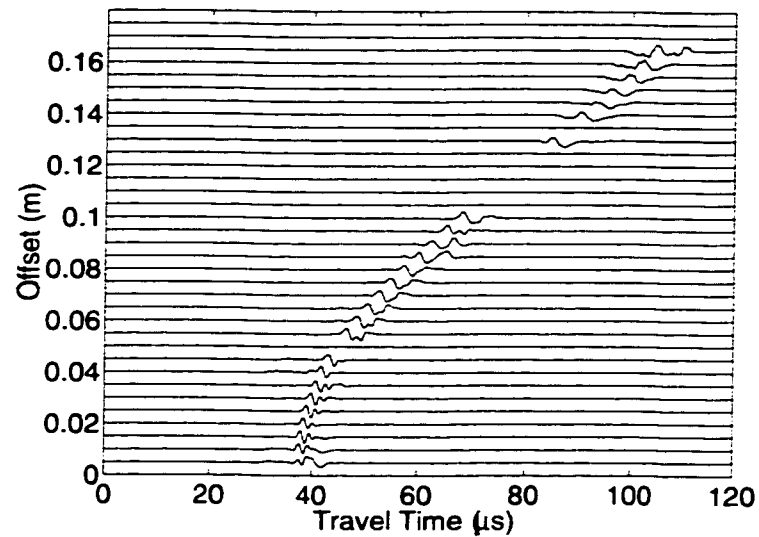


(a) Amplitude versus time traces with offset.



(b) Peak amplitude normalization of the  $\tau - p$  transform via slant-stack of (a).

Figure B.21: SV-polarization results from a 4.0 cm depth source on the phenolic block in the x-y plane.



(a) Amplitude versus time traces with offset.

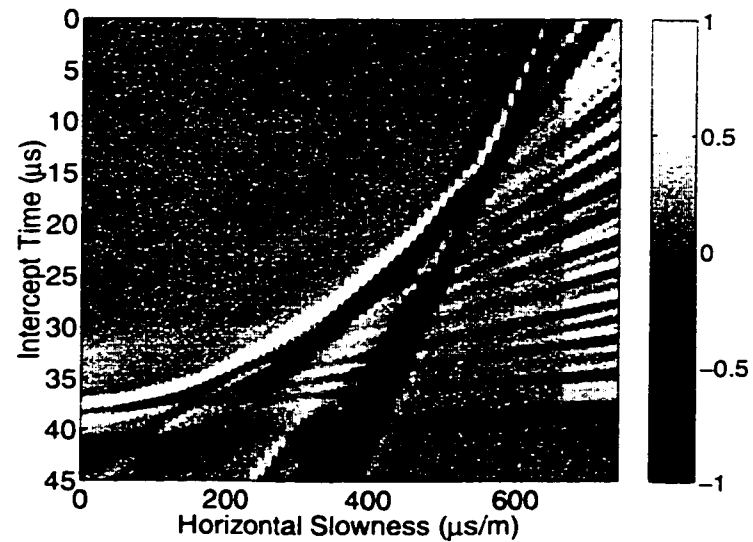
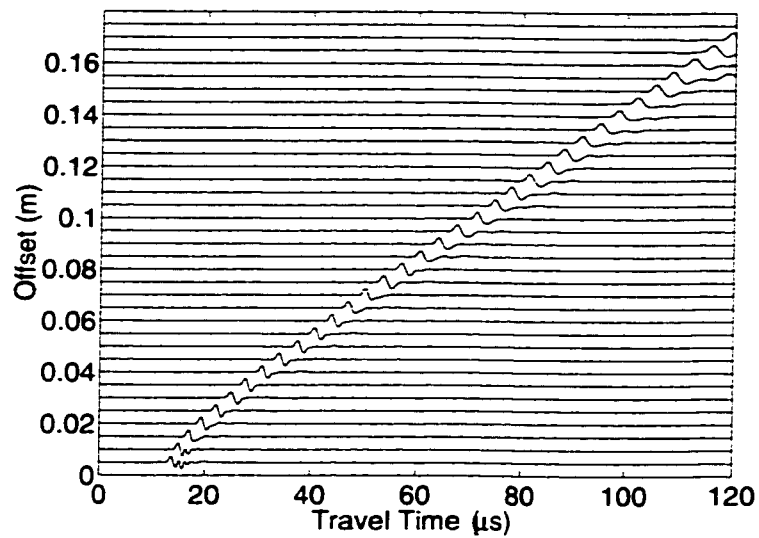
(b) Peak amplitude normalization of the  $\tau - p$  transform via slant-stack of (a).

Figure B.22: SV-polarization results from a 6.0 cm depth source on the phenolic block in the x-y plane.



(a) Amplitude versus time traces with offset.

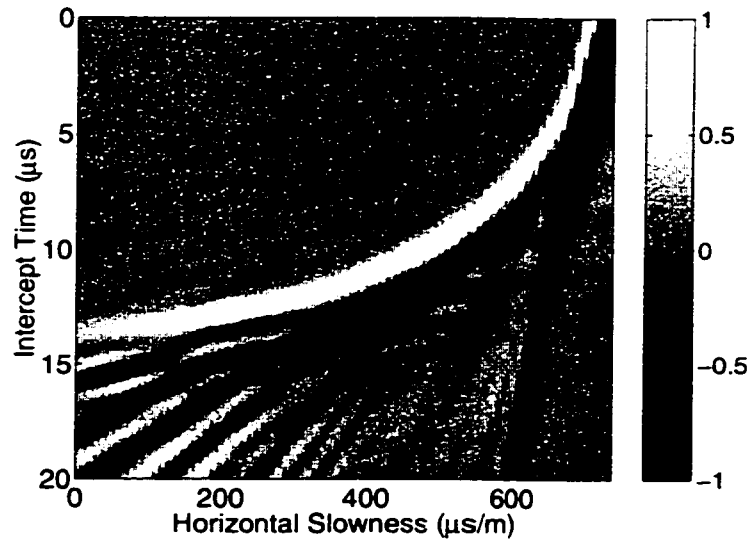
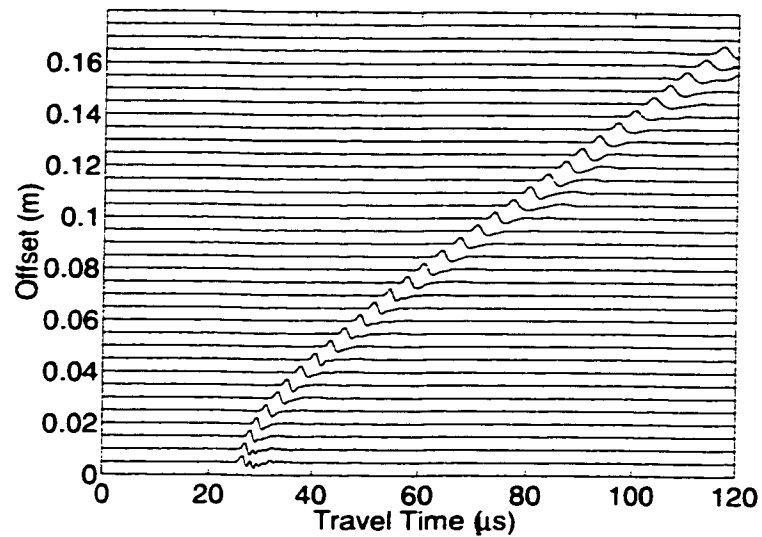
(b) Peak amplitude normalization of the  $\tau - p$  transform via slant-stack of (a).

Figure B.23: SH-polarization results from a 2.0 cm depth source on the phenolic block in the x-y plane.



(a) Amplitude versus time traces with offset.

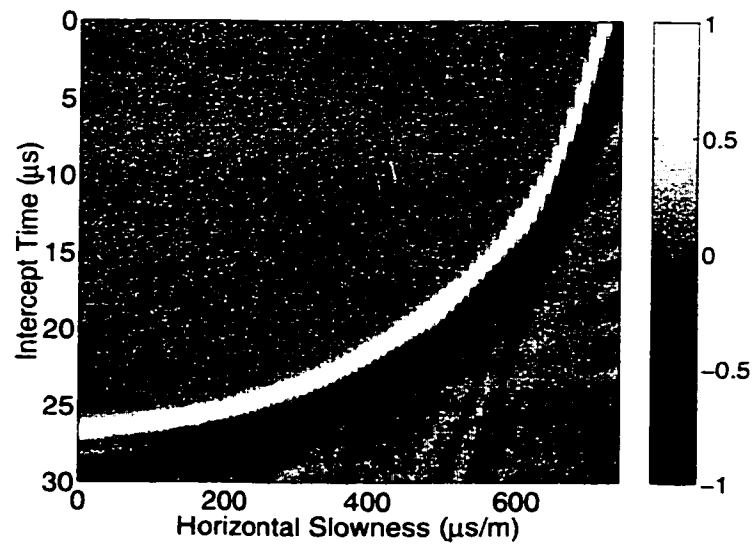
(b) Peak amplitude normalization of the  $\tau - p$  transform via slant-stack of (a).

Figure B.24: SH-polarization results from a 4.0 cm depth source on the phenolic block in the x-y plane.

# Appendix C

## Radon transform and inversion

### C.1 Radon transform

A slant-stack (Radon) transform is a mapping of a two-dimensional function  $f(x, t)$  from the offset-time ( $x, t$ ) domain into the intercept time-horizontal slowness ( $\tau - p$ ) domain. The slant stack (Radon) transform is defined by Robinson (1982) and Tatham (1984):

$$F(\tau, p) = \int_{-\infty}^{\infty} f(x, \tau + px) dx \quad (\text{C.1})$$

where  $F$  is the integration of the amplitudes  $f(x, t)$  along the line  $y = \tau + px$ .

This equation basically means the data is decomposed into different plane wave components where for each  $\tau$  value on a given horizontal slowness  $p$  the amplitudes of all the samples along the line given by the line  $y = \tau + px$  is summed.

The  $\tau - p$  transform used was that described in Equation C.1 where an intercept  $\tau$  and slope  $p$  is chosen and the amplitudes from the  $x - t$  domain along the line  $t = \tau + px$  are summed. No special hyperbolic velocity filtering or ratio filtering was applied (see Kebaili and Schmitt, 1997). The  $\tau - p$  transform program was written in the programming language of Matlab and is shown as

follows:

### C.1.1 Computer program for $\tau - p$ transform

```
% taupeetr.m
% Written by Marko Mah (May 1997)
%
% The purpose of this program is to perform a tau-pee
% transform on the offset-time data.
%
%
% First we must load in the data
% To do this we must determine which files need to be
% loaded in and how many
%
% nfiles is the number of files to be loaded
%
nfiles=input('How many traces are to be loaded?');
%
% the following determines the filename
% count is simply a counter
% filename is the name of the file to be loaded
%
for count = 1:nfiles
    temp=int2str(count);
    if count <= 9
        filename=['or03tr0',temp,'.flow1'];
```



```
    else
        filename=['or03tr',temp,'.flow1'];
    end

    fid=fopen(filename);
    trceloaded=fread(fid,'float');
    fclose(fid);

    % the following puts trceloaded into a matrix
    % where the all the traces will be stored

    if count==1
        data=trceloaded;
    else
        data=[data,trceloaded];
    end
end

clear trceloaded;

% the following figures out the size of the data

[lengthdata,temp]=size(data);

% the following asks for the sampling rate in microsecond (10^-6
secs)
% srate is the sampling rate in seconds
```

```
srate=input('What is the sampling rate in microseconds? ');
srate=srate*0.000001;

% offset1 is the offset at the first trace in metres
% offsetinc is the distance between each trace in metres

offset1=input('What is the offset at the first trace in metres?
');
offsetinc=input('What is the distance between each trace in metres? ');

% The following asks for input parameters for the tau-pee calculations
% taustart is the tau value you wish to start at
% tauinc is how large of an increment you want in tau
% taunum is the number of tau increments you want
% pstart is the p value you wish to start at
% pinc is how large of an increment you want in p
% pnum is the number of p increments you want

taustart=input('At what tau do you want to start at in secs? ');
tauinc=input('How large of an increment in tau do you want in secs? ');
taunum=input('How many increments do you want in tau? ');
```

```
pstart=input('At what p value do you want to start at in secs/metre? ');
pinc=input('How large of an increment in p do you want in secs/metre? ');
pnum=input('How many increments do you want in p? ');

taunum=round(taunum);
pnum=round(pnum);

% tpmatrix is the matrix where all the tau-pee values will be held

tpmatrix=zeros(taunum+1,pnum+1);

% offset is the offset of each trace in metres

offset=[0:1:nfiles-1];
offset=offset*offsetinc+offset1*ones(1,nfiles);

% first we select a tau value and do the tau-pee transform
% for all values of p before doing the next value of tau
% We are going to keep the calculations in the time domain
% as long as possible to prevent round off error.

for count1=0:taunum

    % tau is the tau in seconds
```

```
tau=(taustart+tauinc*count1)*ones(1,nfiles);

for count2=0:pnum
    % p is the p in seconds/metre

    p=pstart+pinc*count2;

    % time is the time in seconds at which the
    % amplitudes will be extracted from the data

    time=tau+p*offset;

    % sample is the sample number at which the
    % amplitudes will be extracted from the data

    sample=round(time/srate+ones(1,nfiles));

    % the following calculates the tau-pee value

    % tpvalue is the tau-pee value for this
    % particular value of tau and pee

    tpvalue=0;

    for count3=1:nfiles

        % the following if statement checks to see if
```

```
% the sample number is less than the length of
% the data and if so extracts the amplitude

    if sample(1,count3) <= lengthdata
        tpvalue=tpvalue+data(sample(1,count3),count3);
    end
end

% now that the tpvalue has been calculated, the
% tpvalue must be put into tpmatrix

    tpmatrix(count1+1,count2+1)=tpvalue;

end

end

% Now that tpmatrix has been created and filled we must now output the data

for count=1:pnum+1
    if count<=9
        temp=int2str(count);
        name=['or03tr0',temp,'.tp'];
    else
        temp=int2str(count);
        name=['or03tr',temp,'.tp'];
    end
end
```

```
    fid=fopen(name,'w');
    fwrite(fid, tpmatrix(:,count), 'float');
    fclose(fid);
end
```

```
time=srate*106*[1:1:lengthdata];
figure
imagesc(offset,time,data);
xlabel('Offset (m)');
ylabel('Time (microseconds)');
title('Offset-Time data');
colormap(gray)
colorbar
```

```
pend=pstart+pinc*pnum;
pvalues=[pstart:pinc:pend];
tauend=taustart+tauinc*taunum;
tauvalues=[taustart:tauinc:tauend];
```

```
figure
imagesc(pvalues,tauvalues,tpmatrix);
xlabel('P (sec/metre)');
ylabel('Tau (sec)');
title('Tau-P data');
colormap(gray)
colorbar
```

This  $\tau - p$  transform was tested on data acquired on a glass block as shown in Figures A.1 to A.6. The average phase velocities calculated from the  $\tau - p$  transform for the glass blocks are  $5724 \pm 64$  m/s,  $3647 \pm 77$  m/s, and  $3467 \pm 15$  m/s for the P, SV, and SH mode transducers respectively. The P and SH velocities match the simple direct pulse transmission P- and S-wave velocities of  $5690 \pm 60$  m/s and  $3440 \pm 26$  m/s respectively to within 1 %. The SV velocities had large errors due to problems with errors in the placement of the source transducers.

## C.2 Inversion

The inversion strategy begins with an initial guess at the elastic coefficients with the assumption that the density is already well known. Phase velocities with propagation angle are calculated from this seed and the residuals of these with those observed are minimized using an L2 norm. An L2 norm is where the square of the differences are used as opposed to an L1 norm where the absolute values of the differences are used. The residual represented by  $\epsilon$  is defined by the following formula:

$$\epsilon = \sum_{i=1}^n (\text{Theoretical Phase Velocity} - \text{Observed Phase Velocity})^2 \quad (\text{C.2})$$

where  $n$  is the number of observed phase velocities.

After this first initial guess, 3 different methods were employed to reduce the residual. The first is a pseudo-least squares method applied iteratively where small increments and decrements to the elastic constants are applied in steps. The second is where pseudo-random increments or decrements to the elastic constants are applied. The random increments or jumps are incorporated in

order to prevent entrapment in localized minima within the residuals. The third is the secant method which is defined by the following formula:

$$x_{n+1} = x_n - f(x_n) \left[ \frac{x_n - x_{n-1}}{f(x_n) - f(x_{n-1})} \right] \quad (\text{C.3})$$

where  $n$  is the position number

In order to try to determine where the function  $f(x_n)$  equals zero, the guess  $x_{n+1}$  is determined by putting a secant line through points  $(x_{n-1}, f(x_{n-1}))$  and  $(x_n, f(x_n))$  and determining where the line intersects zero. This method only works if two points  $f(x_{n-1})$  and  $f(x_n)$  are already calculated. After apply these various methods, a unique solution will more than likely be determined.

The following is a summary of how the inversion works for the orthorhombic case where there are 9 independent elastic constants:

Step 1: Read in data.

Step 2: Calculate residual from initial guess or seed and set as lowest residual case.

Step 3: If there is no change in the elastic constants for 5 iterations or if the residual is small enough, then reduce step size for Step 4.

Step 4: Increase and decrease each independent elastic constant for the lowest residual case by 1 step and calculate residuals.

Step 5: Increase or decrease each independent elastic constant by a pseudo-random step and calculate the residuals.



Step 6: If residuals from Step 4 and Step 5 are less than the lowest residual case, then apply secant method and recalculate residual.

Step 7: Use the elastic constants with the lowest residual as the seed for the next loop.

Step 8: If 500 iterations are performed or residual is lower than set mark, then go to Step 9. If not, go to Step 3.

Step 9: Write out elastic constants and exit.

The inversion was written in the programming language C with the routines `jacobi.c`, `nutil.c` and `nutil.h` being programs based on routines from Numerical Recipes (Press et al. 1989).

## C.2.1 Computer Programs for Inversion.

### Main Inversion Program

```
/* apr28invold.c */
/* written by Marko Mah April 28, 1999 */
/* for the inversion of phase velocities in an orthorhombic mate
rial */

#include <stdlib.h>
#include <stdio.h>
#include <math.h>
#include <string.h>
```

```
#include "nrutil.h"

#define pi 3.1415926535897;

void jacobi(float **a, int nd, float d[], float **v, int *nrot);

void main(int argc, char *argv[])
{
    float rho; /* rho is the density of the material in kg per m3
    */
    double c2d[6][6]; /* c2d is the 2nd order stiffness tensor in
    pascals */
    double c4d[3][3][3][3]; /* c4d is the 4th order stiffness tens
    or in pascals */
    int i,j,k,l,m,n,o,p; /* i,j,k,l,m,n,o,p are counters */
    int nd; /* nd is the size of the dimension */
    double temp[3]; /* temporary variables */
    float planenorm[3][624]; /* contains vector normal to the plan
    e in which data lies */
    float norm[3][624]; /* contains vector describing direction of
    propagation */
    float **ch; /* **ch stores the Christoffel symbols */
    float **partmot; /* **partmot is the matrix which will store t
    he particle motions (eigenvectors) */
    float rhophvelphvel[4]; /* rhophvelphvel is the vector which w
    ill store the eigenvalues */
    int nrot; /* nrot is where the number of jacobi rotations need
    ed is stored */
```

```
float phvel[3]; /* phvel is the vector which will store the phase velocities */
float pwavevel[624], svwavevel[624], shwavevel[624]; /* phase velocities for each polarization */
float fileres[624],filevel[624];
double tempa[3], tempb[3], tempc[3], tempv[3]; /* temporary sorting variables */
double dec1, dec2; /* temporary sorting variables */
char tempname[6];
int wavetype[624];
double seed[9]; /* what values you start the inversion off at */
double guess[29][9];
float stepsize;
int numint;
float randsteplimit;
int repeat0;
int change[28]; /* which elastic constant is being changed */
float epsilon[29]; /* a measure of the discrepancies squared */
int smallest;
float temp1; /* a temporary variable */
float slope, intercept; /* slope and intercept as calculated by the secant method */

int whichint[501]; /* which iteration is it */
int whichsmallest[501]; /* which is the smallest epsilon for this iteration */
float whichepsilon[501]; /* what is the value of this smallest
```

```
epsilon */

FILE *inputfile, *outputfile;

/* the following reads in the data */

inputfile=fopen("realdata.txt", "r");
for (i=0;i<624;i++){
    fscanf(inputfile, "%s\t %f\t %f\t %f\t %f\t %f\t %f\t %f\n",
        tempname,&planenorm[0][i],&planenorm[1][i],&planenorm[2][i],
        &norm[0][i],&norm[1][i],&norm[2][i],&filelevel[i]);
    /*    fprintf(stderr, "%s\t %f\t %f\t %f\t %f\t %f\t %f\t %f\t %f\n",
        tempname,planenorm[0][i],planenorm[1][i],planenorm[2][i],
        norm[0][i],norm[1][i],norm[2][i],filelevel[i]); */
    if (strcmp(tempname,"pwave")==0){
        wavetype[i]=1; /* wavetype=1 is a P-wave */
    }
    else if (strcmp(tempname,"shwave")==0){
        wavetype[i]=2; /* wavetype=2 is a sh-wave */
    }
    else if (strcmp(tempname,"svwave")==0){
        wavetype[i]=3; /* wavetype=3 is a sv-wave */
    }
}
fclose(inputfile);

/* this is where we initialize many of the variables */
```

```
rho=1395; /* sets the density of the material */
printf("rho is %f\n", rho);

nd=3; /* sets the size of the dimension */

stepsize=1E9; /* assigns the initial stepsize */
numint=0; /* initializes the number of iterations the program
has gone through */
randsteplimit=1E9; /* assigns the limit of the random guess */
repeat0=0; /* initializes the number of consecutive repeated r
esults the program has obtained */

/* tells the program which of the 9 (i.e. 0 to 8) elastic cons
tants to change */
change[0]=0;
change[1]=0;
change[2]=0;
change[3]=1;
change[4]=1;
change[5]=2;
change[6]=2;
change[7]=3;
change[8]=3;
change[9]=4;
change[10]=4;
```

```
change[11]=5;
change[12]=5;
change[13]=6;
change[14]=6;
change[15]=7;
change[16]=7;
change[17]=8;
change[18]=8;
change[19]=0;
change[20]=1;
change[21]=2;
change[22]=3;
change[23]=4;
change[24]=5;
change[25]=6;
change[26]=7;
change[27]=8;

epsilon[0]=0.0;

/* the following calculates the residual epsilon for the seed
(start value) as taken from Vestrum(1994)*/
seed[0]=17.522E9;
seed[1]=7.220E9;
seed[2]=6.609E9;
seed[3]=15.777E9;
seed[4]=6.197E9;
```

```
seed[5]=11.751E9;
seed[6]=3.127E9;
seed[7]=3.484E9;
seed[8]=3.804E9;

/* initializes c2d (0->8) with the 9 seed values */
c2d[0][0]=seed[0];
c2d[0][1]=seed[1];
c2d[0][2]=seed[2];
c2d[0][3]=0;
c2d[0][4]=0;
c2d[0][5]=0;
c2d[1][1]=seed[3];
c2d[1][2]=seed[4];
c2d[1][3]=0;
c2d[1][4]=0;
c2d[1][5]=0;
c2d[2][2]=seed[5];
c2d[2][3]=0;
c2d[2][4]=0;
c2d[2][5]=0;
c2d[3][3]=seed[6];
c2d[3][4]=0;
c2d[3][5]=0;
c2d[4][4]=seed[7];
c2d[4][5]=0;
c2d[5][5]=seed[8];
```

```
/* sets c_ij -> c_ji */
c2d[1][0]=c2d[0][1];
c2d[2][0]=c2d[0][2];
c2d[2][1]=c2d[1][2];
c2d[3][0]=c2d[0][3];
c2d[3][1]=c2d[1][3];
c2d[3][2]=c2d[2][3];
c2d[4][0]=c2d[0][4];
c2d[4][1]=c2d[1][4];
c2d[4][2]=c2d[2][4];
c2d[4][3]=c2d[3][4];
c2d[5][0]=c2d[0][5];
c2d[5][1]=c2d[1][5];
c2d[5][2]=c2d[2][5];
c2d[5][3]=c2d[3][5];
c2d[5][4]=c2d[4][5];

/* the following converts the 2nd-order stiffness tensor to a
4th-order stiffness tensor */
for (i=1; i<=3; i++){
  for (j=1; j<=3; j++){
    for (k=1; k<=3; k++){
      for (l=1; l<=3; l++){
        if (i==j)
          m=j;
        else
```



```
        m=9-(i+j);

        if (k==1)
            n=k;
        else
            n=9-(k+1);

        c4d[i-1][j-1][k-1][l-1]=c2d[m-1][n-1];
    }
}
}

/* end of converting the 2nd-order stiffness tensor to a 4th-order
stiffness tensor */

/* ch is the matrix that will contain the christoffel symbols */
/* initialize ch to a 3 by 3 matrix */
ch=dmatrixf(1,3,1,3); /* dmatrixf is a float pointer */

/* initialize partmot to a 3 by 3 matrix */
partmot=dmatrixf(1,3,1,3);

/* start of first loop to initialize many of the values */
for (o=0;o<624;o++){

    /* first must initialize ch */
    for (i=1; i<=3; i++){
```

```

    for (j=1; j<=3; j++){
        ch[i][j]=0.0;
    }
}

/* calculates the christoffel symbols */
for (i=0; i<=2; i++){
    for (j=0; j<=2; j++){
        for (k=0; k<=2; k++){
            for (l=0; l<=2; l++){
                ch[(i+1)][(l+1)]=ch[(i+1)][(l+1)]+c4d[i][j][k][l]*no
                rm[j][o]*norm[k][o];
            }
        }
    }
}

/* Now we must figure out the eigenvalues and eigenvectors */
/* the inputs into jacobi are ch and nd */
/* ch are the christoffel symbols and nd contains length of
a dimension */
/* rhophvelphvel, partmot, and nrot are the outputs */

jacobi(ch, nd, rhophvelphvel, partmot, &nrot);

/* the following determines the phase velocity */
for (i=0; i<=2; i++){

```

```

    phvel[i]=sqrt(rhophvelphvel[i+1]/rho);
}

/* the following normalizes the particle motions */
for (i=1;i<=3;i++){
    temp[i-1]=sqrt(partmot[1][i]*partmot[1][i]+partmot[2][i]*p
    artmot[2][i]+partmot[3][i]*partmot[3][i]);
}
for (i=1;i<=3;i++){
    for (j=1;j<=3;j++){
        partmot[i][j]=partmot[i][j]/temp[j-1];
    }
}
/* end of normalization of particle motions */

/* the following sorts the polarizations */
if ((phvel[0] > phvel[1]) && (phvel[0] > phvel[2])){
    /* case for if P-wave is first entry */
    tempv[0]=phvel[0];
    tempv[1]=phvel[1];
    tempv[2]=phvel[2];
    for (i=0;i<=2;i++){
        tempa[i]=partmot[i+1][1];
        tempb[i]=partmot[i+1][2];
        tempc[i]=partmot[i+1][3];
    }
}

```

```
else if (phvel[1]>phvel[2]){
    /* case for if P-wave is second entry */
    tempv[0]=phvel[1];
    tempv[1]=phvel[0];
    tempv[2]=phvel[2];
    for (i=0;i<=2;i++){
        tempa[i]=partmot[i+1][2];
        tempb[i]=partmot[i+1][1];
        tempc[i]=partmot[i+1][3];
    }
}
else{
    /* case for if P-wave is third entry */
    tempv[0]=phvel[2];
    tempv[1]=phvel[1];
    tempv[2]=phvel[0];
    for (i=0;i<=2;i++){
        tempa[i]=partmot[i+1][3];
        tempb[i]=partmot[i+1][2];
        tempc[i]=partmot[i+1][1];
    }
} /* end of if-elseif-else loop */

pwavevel[0]=tempv[0]; /* sets the P-wave velocity */

/* takes the dot product between the direction of propagation
n and the particle motion */
```

```
for (i=0;i<=2;i++){
    temp[i]=planenorm[i][o]*tempb[i];
}
dec1=fabs(temp[0]+temp[1]+temp[2]);

for (i=0;i<=2;i++){
    temp[i]=planenorm[i][o]*tempc[i];
}
dec2=fabs(temp[0]+temp[1]+temp[2]);

/* determines which of the 2 remaining polarizations are SH-wave
and SV-wave*/
if (dec1 < dec2){
    svwavevel[o]=tempv[1];
    shwavevel[o]=tempv[2];
}
else {
    svwavevel[o]=tempv[2];
    shwavevel[o]=tempv[1];
} /*end of if-else loop */
/* end of sorting out polarizations */

/* determines and calculates the residual squared*/
if (wavetype[o]==1){
    fileres[o]=(pwavevel[o]-filevel[o])*(pwavevel[o]-filevel[o
]);
```

```
    }
    else if (wavetype[o]==2){
        fileres[o]=(shwavevel[o]-filevel[o])*(shwavevel[o]-filevel
        [o]);
    }
    else if (wavetype[o]==3){
        fileres[o]=(svwavevel[o]-filevel[o])*(svwavevel[o]-filevel
        [o]);
    } /* end of if-elseif-elseif loop */

    epsilon[0] += fileres[o]; /* determines the total residual s
    quared for the initial guess */

} /* end of loop for o to initialize many of variables*/

fprintf(stderr,"epsilon[0] is %f\n",epsilon[0]);

/* the following stores some data to be written out later */
whichint[0]=0;
whichsmallest[0]=0;
whichepsilon[0]=epsilon[0];

/* stop criterion to be used*/
while ((epsilon[0]>10) && (numint <500)){

    numint += 1; /* number of iterations plus 1 */
```

```
fprintf(stderr, "\nnumint is %d\n", numint);

/* adjusts the step size */
if (stepsize > 1E8){
    if ((epsilon[0]<5000000) || (repeat0>3)){
        stepsize=1E8;
    }
}

/* adjusts the step size */
if (repeat0>5){
    if (epsilon[0]<3000000){
        stepsize=1E7;
    }
    if (epsilon[0]<2000000){
        stepsize=1E6;
    }
    if (epsilon[0]<1000000){
        stepsize=1E5;
    }
}

/* initialize your guesses with the seed */
for (i=0; i<29; i++){
    for (j=0; j<9; j++){
        guess[i][j]=seed[j];
    }
}
```

```
}

/* initializes epsilon which holds the residual squared*/
for (i=1; i<29; i++){
    epsilon[i]=0.0;
}

/* guess[0][:] contains the original guess */
/* guess[1][0] will be increased by stepsize and guess[1][1-
8] will remain unchanged */
/* guess[2][0] will be decreased by stepsize and guess[2][1-
8] will remain unchanged */
/* guess[3][1] will be increased by stepsize and guess[3][0,
2-8] will remain unchanged */
/* guess[4][1] will be decreased by stepsize and guess[4][0,
2-8] will remain unchanged */
/* ... etc ... */
/* guess[18][8] will be decreased by stepsize and guess[18][
0-7] will remain unchanged */

/* change guesses[1-18][:] */
for (i=0; i<9; i++){
    k=i*2+1;
    l=i*2+2;

    guess[k][i]+=stepsize; /* guess */
    fprintf(stderr, "guess[%d] [%d]=%f\n", k, i, guess[k][i]);
```



```
    guess[1][i]-=stepsize;
    fprintf(stderr,"guess[%d][%d]=%f\n",1,i,guess[1][i]);
}

/* initialize the random guesses */
/* guess[19][0] will be increased or decreased by a random s
tep and guess[19][1-8] will remain unchanged */
/* guess[20][1] will be increased or decreased by a random s
tep and guess[20][0,2-8] will remain unchanged */
/* ... etc ... */
/* guess[27][8] will be increased or decreased by a random s
tep and guess[27][0-7] will remain unchanged */

for (i=0; i<9; i++){
    temp1=((rand())/32767.0)-0.5;
    guess[19+i][i] += randsteplimit*temp1;
    fprintf(stderr,"random guess[%d][%d] is %f\n",19+i,i,guess
[19+i][i]);
}

/* calculates the epsilons for guess[1-27][:] */
for (p=1; p<28; p++){

    /* the following initializes c2d with the guesses */
    c2d[0][0]=guess[p][0];
    c2d[0][1]=guess[p][1];
```

```
c2d[0][2]=guess[p][2];
c2d[0][3]=0;
c2d[0][4]=0;
c2d[0][5]=0;
c2d[1][1]=guess[p][3];
c2d[1][2]=guess[p][4];
c2d[1][3]=0;
c2d[1][4]=0;
c2d[1][5]=0;
c2d[2][2]=guess[p][5];
c2d[2][3]=0;
c2d[2][4]=0;
c2d[2][5]=0;
c2d[3][3]=guess[p][6];
c2d[3][4]=0;
c2d[3][5]=0;
c2d[4][4]=guess[p][7];
c2d[4][5]=0;
c2d[5][5]=guess[p][8];

/* the following sets c_ij->c_ji */
c2d[1][0]=c2d[0][1];
c2d[2][0]=c2d[0][2];
c2d[2][1]=c2d[1][2];
c2d[3][0]=c2d[0][3];
c2d[3][1]=c2d[1][3];
c2d[3][2]=c2d[2][3];
```

```

c2d[4][0]=c2d[0][4];
c2d[4][1]=c2d[1][4];
c2d[4][2]=c2d[2][4];
c2d[4][3]=c2d[3][4];
c2d[5][0]=c2d[0][5];
c2d[5][1]=c2d[1][5];
c2d[5][2]=c2d[2][5];
c2d[5][3]=c2d[3][5];
c2d[5][4]=c2d[4][5];

```

```

/* the following converts the 2nd-order stiffness tensor t
o a 4th-order stiffness tensor */

```

```

for (i=1; i<=3; i++){
  for (j=1; j<=3; j++){
    for (k=1; k<=3; k++){
      for (l=1; l<=3; l++){
        if (i==j)
          m=j;
        else
          m=9-(i+j);

        if (k==1)
          n=k;
        else
          n=9-(k+1);

        c4d[i-1][j-1][k-1][l-1]=c2d[m-1][n-1];

```

```

        }
    }
}

for (o=0;o<624;o++){
    /* first must initialize ch */
    for (i=1; i<=3; i++){
        for (j=1; j<=3; j++){
            ch[i][j]=0.0;
        }
    }

    /* calculates the christoffel symbols */
    for (i=0; i<=2; i++){
        for (j=0; j<=2; j++){
            for (k=0; k<=2; k++){
                for (l=0; l<=2; l++){
                    ch[(i+1)][(l+1)]=ch[(i+1)][(l+1)]+c4d[i][j][k][l]
                    *norm[j][o]*norm[k][o];
                }
            }
        }
    }

    /* Now we must figure out the eigenvalues and eigenvectors */

```

```
/* the inputs into jacobi are ch and nd */
/* ch are the christoffel symbols and nd contains length
of a dimension */
/* rhophvelphvel, partmot, and nrot are the outputs */

jacobi(ch, nd, rhophvelphvel, partmot, &nrot);

/* the following determines the phase velocity */
for (i=0;i<=2;i++){
    phvel[i]=sqrt(rhophvelphvel[i+1]/rho);
}

/* the following normalizes the particle motions */
for (i=1;i<=3;i++){
    temp[i-1]=sqrt(partmot[1][i]*partmot[1][i]+partmot[2][
    i]*partmot[2][i]+partmot[3][i]*partmot[3][i]);
}
for (i=1;i<=3;i++){
    for (j=1;j<=3;j++){
        partmot[i][j]=partmot[i][j]/temp[j-1];
    }
}
/* end of normalization of particle motions */

/* the following sorts the polarizations */
if ((phvel[0] > phvel[1]) && (phvel[0] > phvel[2])){
    /* case for if P-wave is first entry */
```

```
    tempv[0]=phvel[0];
    tempv[1]=phvel[1];
    tempv[2]=phvel[2];
    for (i=0;i<=2;i++){
        tempa[i]=partmot[i+1][1];
        tempb[i]=partmot[i+1][2];
        tempc[i]=partmot[i+1][3];
    }
}
else if (phvel[1]>phvel[2]){
    /* case for if P-wave is second entry */
    tempv[0]=phvel[1];
    tempv[1]=phvel[0];
    tempv[2]=phvel[2];
    for (i=0;i<=2;i++){
        tempa[i]=partmot[i+1][2];
        tempb[i]=partmot[i+1][1];
        tempc[i]=partmot[i+1][3];
    }
}
else{
    /* case for if P-wave is third entry */
    tempv[0]=phvel[2];
    tempv[1]=phvel[1];
    tempv[2]=phvel[0];
    for (i=0;i<=2;i++){
        tempa[i]=partmot[i+1][3];
```

```
        tempb[i]=partmot[i+1][2];
        tempc[i]=partmot[i+1][1];
    }
} /* end of if-elseif-else loop */

pwavevel[o]=tempv[0]; /* sets the P-wave velocity */

/* takes the dot product between the direction of propagation
and the particle motion */

for (i=0;i<=2;i++){
    temp[i]=planenorm[i][o]*tempb[i];
}
dec1=fabs(temp[0]+temp[1]+temp[2]);

for (i=0;i<=2;i++){
    temp[i]=planenorm[i][o]*tempc[i];
}
dec2=fabs(temp[0]+temp[1]+temp[2]);

/* determines which of the 2 remaining polarizations are
SH-wave and SV-wave*/
if (dec1 < dec2){
    svwavevel[o]=tempv[1];
    shwavevel[o]=tempv[2];
}
else {
```

```
        svwavevel[o]=tempv[2];
        shwavevel[o]=tempv[1];
    } /*end of if-else loop */
    /* end of sorting out polarizations */

    /* determines and calculates the residual squared*/
    if (wavetype[o]==1){
        fileres[o]=(pwavevel[o]-filevel[o])*(pwavevel[o]-filevel[o]);
    }
    else if (wavetype[o]==2){
        fileres[o]=(shwavevel[o]-filevel[o])*(shwavevel[o]-filevel[o]);
    }
    else if (wavetype[o]==3){
        fileres[o]=(svwavevel[o]-filevel[o])*(svwavevel[o]-filevel[o]);
    } /* end of if-elseif-elseif loop */

    epsilon[p] += fileres[o]; /* determines the total residual squared for the initial guess */

}
/* end of loop for o */

fprintf(stderr,"epsilon[%d] is %f\n",p,epsilon[p]);
```



```
}
/* end of loop for p which checks over guess[1-27][:] */

/* now to choose the smallest epsilon */
smallest=0;
for (i=1;i<28;i++){
    if (epsilon[i]<epsilon[smallest]){
        smallest=i;
    }
}

/* the following determines a guess using the secant method
based on the smallest epsilon and then calculates an epsilon
*/
if (smallest != 0){
    slope=(epsilon[smallest]-epsilon[0])/(guess[smallest][change[smallest]]-guess[0][change[smallest]]);
    fprintf(stderr,"slope is %f\n", slope);
    intercept=epsilon[smallest]-slope*guess[smallest][change[smallest]];
    fprintf(stderr,"intercept is %f\n",intercept);
    guess[28][change[smallest]]=(-intercept/slope);
    fprintf(stderr,"guess[28][%d] is %f\n",change[smallest],guess[28][change[smallest]]);

    c2d[0][0]=guess[28][0];
    c2d[0][1]=guess[28][1];
```

```
c2d[0][2]=guess[28][2];
c2d[0][3]=0;
c2d[0][4]=0;
c2d[0][5]=0;
c2d[1][1]=guess[28][3];
c2d[1][2]=guess[28][4];
c2d[1][3]=0;
c2d[1][4]=0;
c2d[1][5]=0;
c2d[2][2]=guess[28][5];
c2d[2][3]=0;
c2d[2][4]=0;
c2d[2][5]=0;
c2d[3][3]=guess[28][6];
c2d[3][4]=0;
c2d[3][5]=0;
c2d[4][4]=guess[28][7];
c2d[4][5]=0;
c2d[5][5]=guess[28][8];

c2d[1][0]=c2d[0][1];
c2d[2][0]=c2d[0][2];
c2d[2][1]=c2d[1][2];
c2d[3][0]=c2d[0][3];
c2d[3][1]=c2d[1][3];
c2d[3][2]=c2d[2][3];
c2d[4][0]=c2d[0][4];
```

```

c2d[4][1]=c2d[1][4];
c2d[4][2]=c2d[2][4];
c2d[4][3]=c2d[3][4];
c2d[5][0]=c2d[0][5];
c2d[5][1]=c2d[1][5];
c2d[5][2]=c2d[2][5];
c2d[5][3]=c2d[3][5];
c2d[5][4]=c2d[4][5];

/* the following converts the 2nd-order stiffness tensor t
o a 4th-order stiffness tensor */
for (i=1; i<=3; i++){
  for (j=1; j<=3; j++){
    for (k=1; k<=3; k++){
      for (l=1; l<=3; l++){
        if (i==j)
          m=j;
        else
          m=9-(i+j);

        if (k==l)
          n=k;
        else
          n=9-(k+l);

        c4d[i-1][j-1][k-1][l-1]=c2d[m-1][n-1];
      }
    }
  }
}

```

```
    }
  }
}

for (o=0;o<624;o++){

  /* first must initialize ch */
  for (i=1; i<=3; i++){
    for (j=1; j<=3; j++){
      ch[i][j]=0.0;
    }
  }

  /* calculates the christoffel symbols */
  for (i=0; i<=2; i++){
    for (j=0; j<=2; j++){
      for (k=0; k<=2; k++){
        for (l=0; l<=2; l++){
          ch[(i+1)][(l+1)]=ch[(i+1)][(l+1)]+c4d[i][j][k][l]
            *norm[j][o]*norm[k][o];
        }
      }
    }
  }

  /* Now we must figure out the eigenvalues and eigenvecto
rs */
```

```
/* the inputs into jacobi are ch and nd */
/* ch are the christoffel symbols and nd contains length
of a dimension */
/* rhophvelphvel, partmot, and nrot are the outputs */

jacobi(ch, nd, rhophvelphvel, partmot, &nrot);

/* the following determines the phase velocity */
for (i=0;i<=2;i++){
    phvel[i]=sqrt(rhophvelphvel[i+1]/rho);
}

/* the following normalizes the particle motions */
for (i=1;i<=3;i++){
    temp[i-1]=sqrt(partmot[1][i]*partmot[1][i]+partmot[2][
    i]*partmot[2][i]+partmot[3][i]*partmot[3][i]);
}
for (i=1;i<=3;i++){
    for (j=1;j<=3;j++){
        partmot[i][j]=partmot[i][j]/temp[j-1];
    }
}
/* end of normalization of particle motions */

/* the following sorts the polarizations */
if ((phvel[0] > phvel[1]) && (phvel[0] > phvel[2])){
    /* case for if P-wave is first entry */
```

```
    tempv[0]=phvel[0];
    tempv[1]=phvel[1];
    tempv[2]=phvel[2];
    for (i=0;i<=2;i++){
        tempa[i]=partmot[i+1][1];
        tempb[i]=partmot[i+1][2];
        tempc[i]=partmot[i+1][3];
    }
}
else if (phvel[1]>phvel[2]){
    /* case for if P-wave is second entry */
    tempv[0]=phvel[1];
    tempv[1]=phvel[0];
    tempv[2]=phvel[2];
    for (i=0;i<=2;i++){
        tempa[i]=partmot[i+1][2];
        tempb[i]=partmot[i+1][1];
        tempc[i]=partmot[i+1][3];
    }
}
else{
    /* case for if P-wave is third entry */
    tempv[0]=phvel[2];
    tempv[1]=phvel[1];
    tempv[2]=phvel[0];
    for (i=0;i<=2;i++){
        tempa[i]=partmot[i+1][3];
```

```
        tempb[i]=partmot[i+1][2];
        tempc[i]=partmot[i+1][1];
    }
} /* end of if-elseif-else loop */

pwavevel[o]=tempv[0]; /* sets the P-wave velocity */

/* takes the dot product between the direction of propaga
tion and the particle motion */

for (i=0;i<=2;i++){
    temp[i]=planenorm[i][o]*tempb[i];
}
dec1=fabs(temp[0]+temp[1]+temp[2]);

for (i=0;i<=2;i++){
    temp[i]=planenorm[i][o]*tempc[i];
}
dec2=fabs(temp[0]+temp[1]+temp[2]);

/* determines which of the 2 remaining polarizations are
SH-wave and SV-wave*/
if (dec1 < dec2){
    svwavevel[o]=tempv[1];
    shwavevel[o]=tempv[2];
}
else {
```

```
        svwavevel[o]=tempv[2];
        shwavevel[o]=tempv[1];
    } /*end of if-else loop */
    /* end of sorting out polarizations */

    /* determines and calculates the residual squared*/
    if (wavetype[o]==1){
        fileres[o]=(pwavevel[o]-filevel[o])*(pwavevel[o]-filevel[o]);
    }
    else if (wavetype[o]==2){
        fileres[o]=(shwavevel[o]-filevel[o])*(shwavevel[o]-filevel[o]);
    }
    else if (wavetype[o]==3){
        fileres[o]=(svwavevel[o]-filevel[o])*(svwavevel[o]-filevel[o]);
    } /* end of if-elseif-elseif loop */

    epsilon[28] += fileres[o];

}
/* end of loop for o */

fprintf(stderr,"epsilon[28] is %f\n",epsilon[28]);

if (epsilon[28]<epsilon[smallest]){
```



```
        smallest=28;
    }

    fprintf(stderr,"epsilon[28] is %f\n",epsilon[28]);
}
else {
    epsilon[28]=epsilon[0];
}
/* end of epsilon determined by secant method */

/* the following counts how many times the seed HAS NOT cha
nged */
if (smallest==0){
    repeat0 += 1;
}
else {
    repeat0=0;
}

fprintf(stderr,"smallest is %d\n", smallest);

/* the following initializes the new seed */

for (i=0; i<9; i++){
    seed[i]=guess[smallest][i];
    fprintf(stderr,"seed[%d]=%f\n",i,seed[i]);
}
```

```
    epsilon[0]=epsilon[smallest];

    /* the following stores some data to be written out later */
    whichint[numint]=numint;
    whichsmallest[numint]=smallest;
    whichepsilon[numint]=epsilon[0];

}

/* end of while loop */

/* now to write out whichint, whichsmallest, and whichepsilon */
outputfile=fopen("apr28invold.epsilon","w");
for (i=0; i<501; i++){
    fprintf(outputfile,"%d\t %d\t %f\n",whichint[i],whichsmallest[i],whichepsilon[i]);
}
fclose(outputfile);

/* now to write out the seeds */
outputfile=fopen("apr28invold.seed","w");
for (i=0; i<9; i++){
    fprintf(outputfile,"seed[%d]=%f\n",i,seed[i]);
}
fclose(outputfile);

}
```

**Subsidiary Computer Programs**

```
/* jacobi.c (Modified from Numerical Recipes) */
#include <math.h>
#include <stdio.h>
#include "nrutil.h"
#define ROTATE(a,i,j,k,l) g=a[i][j]; h=a[k][l]; a[i][j]=g-s*(h+g
*tau); a[k][l]=h+s*(g-h*tau);
void jacobi(float **a, int n, float d[], float **v, int *nrot)
{
    int j,iq,ip,i;
    float tresh, theta, tau, t, sm, s, h, g, c, *b, *z;
    b=vector(1,n);
    z=vector(1,n);
    for (ip=1;ip<=n;ip++){
        for (iq=1;iq<=n;iq++){
            v[ip][iq]=0.0;
        }
        v[ip][ip]=1.0;
    }
    for (ip=1; ip<=n;ip++){
        b[ip]=d[ip]=a[ip][ip];
        z[ip]=0.0;
    }
    *nrot=0;
    for (i=1;i<=50;i++){
        sm=0.0;
        for (ip=1;ip<=n-1;ip++){
```

```
    for (iq=ip+1;iq<=n;iq++)
        sm += fabs(a[ip][iq]);
}
if (sm==0.0){
    free_vector(z,1,n);
    free_vector(b,1,n);
    return;
}
if (i<4)
    tresh=0.2*sm/(n*n);
else
    tresh=0.0;
for (ip=1;ip<=n-1;ip++){
    for (iq=ip+1;iq<=n;iq++){
        g=100.0*fabs(a[ip][iq]);
        if (i>4 && (float)(fabs(d[ip])+g)==(float)fabs(d[ip])
            && (float)(fabs(d[iq])+g)==(float)fabs(d[iq]))
            a[ip][iq]=0.0;
        else if (fabs(a[ip][iq])> tresh){
            h=d[iq]-d[ip];
            if ((float)(fabs(h)+g)==(float)fabs(h))
                t=(a[ip][iq])/h;
            else {
                theta=0.5*h/(a[ip][iq]);
                t=1.0/(fabs(theta)+sqrt(1.0+theta*theta));
                if (theta < 0.0) t = -t;
            }
        }
    }
}
```

```
    c=1.0/sqrt(1+t*t);
    s=t*c;
    tau=s/(1.0+c);
    h=t*a[ip][iq];
    z[ip] -= h;
    z[iq] += h;
    d[ip] -= h;
    d[iq] += h;
    a[ip][iq]=0.0;
    for (j=1;j<=ip-1;j++){
        ROTATE(a,j,ip,j,iq)
    }
    for (j=ip+1;j<=iq-1;j++){
        ROTATE(a,ip,j,j,iq)
    }
    for (j=iq+1;j<=n;j++){
        ROTATE(a,ip,j,iq,j)
    }
    for (j=1;j<=n;j++){
        ROTATE(v,j,ip,j,iq)
    }
    ++(*nrot);
}
}
for (ip=1;ip<=n;ip++){
    b[ip] += z[ip];
```

```
        d[ip]=b[ip];
        z[ip]=0.0;
    }
}
nrerror("Too many iterations in routine jacobi");
}

/* nrutil.c */
#include <stdio.h>
#include <stddef.h>
#include <stdlib.h>
#define FREE_ARG char *
#define NR_END 0
/* a modification of the nrutils.c as found in Numerical Recipes
*/
void nrerror(char error_text[])
/* Numerical Recipes standard error handler */
{
    fprintf(stderr,"Numerical Resipes run-time error...\n");
    fprintf(stderr,"%s\n",error_text);
    fprintf(stderr,"...now exiting to system...\n");
    exit(1);
}

float *vector(long nl, long nh)
/* allocate a float vector with subscript range v[nl...nh] */
{
    float *v;
    v=(float *)malloc((size_t) ((nh-nl+1-NR_END)*sizeof(float)));
}
```

```

    if (!v) nrerror("allocation failure in vector()");
    return v-nl+NR_END;
}

double **dmatrix(long nrl, long nrh, long ncl, long nch)
/* allocate a double matrix with subscript range m[nrl...nrh][nc
1...nch] */
{
    long i, nrow=nrh-nrl+1, ncol=nch-ncl+1;
    double **m;
    /* allocate pointers to rows */
    m=(double **) malloc((size_t)((nrow+NR_END)*sizeof(double*)));
    if (!m) nrerror("allocation failure 1 in matrix()");
    m+=NR_END;
    m-=nrl;
    /* allocate rows and set pointers to them */
    m[nrl]=(double *) malloc((size_t)((nrow*ncol+NR_END)*sizeof(do
uble)));
    if (!m[nrl]) nrerror("allocation failure 2 in matrix()");
    m[nrl]+=NR_END;
    m[nrl]-=ncl;
    for(i=nrl+1; i<=nrh;i++) m[i]=m[i-1]+ncol;
    /* return pointer to array of pointers to rows */
    return m;
}

float **dmatrixf(long nrl, long nrh, long ncl, long nch)
/* allocate a float matrix with subscript range m[nrl...nrh][nc1
...nch] */

```

```
{
    long i, nrow=nrh-nrl+1, ncol=nch-ncl+1;
    float **m;
    /* allocate pointers to rows */
    m=(float **) malloc((size_t)((nrow+NR_END)*sizeof(float*)));
    if (!m) nrerror("allocation failure 1 in matrix()");
    m+=NR_END;
    m-=nrl;
    /* allocate rows and set pointers to them */
    m[nrl]=(float *) malloc((size_t)((nrow*ncol+NR_END)*sizeof(float)));
    if (!m[nrl]) nrerror("allocation failure 2 in matrix()");
    m[nrl]+=NR_END;
    m[nrl]-=ncl;
    for(i=nrl+1; i<=nrh;i++) m[i]=m[i-1]+ncol;
    /* return pointer to array of pointers to rows */
    return m;
}

void free_vector(float *v, long nl, long nh)
/* free a float vector allocated with vector() */
{
    free((FREE_ARG) (v+nl-NR_END));
}

void free_dmatrixf(float **m, long nrl, long nrh, long ncl,
long nch)
/* free a float matrix allocated by dmatrixf() */
{
```



```

    free((FREE_ARG) (m[nr1]+ncl-NR_END));
    free((FREE_ARG) (m+nr1-NR_END));
}

/* nrutil.h (Modified from Numerical Recipes) */
#ifndef _NR_UTILS_H_
#define _NR_UTILS_H_
float *vector(long nl, long nh);
double **dmatrix(long nrl, long nrh, long ncl, long nch);
float **dmatrixf(long nrl, long nrh, long ncl, long nch);
void free_vector(float *v, long nl, long nh);
void nrerror(char error_text[]);
void free_dmatrixf(float **m, long nrl, long nrh, long ncl,
long nch);
#endif /* _NR_UTILS_H_ */

```

### C.2.2 Testing of inversion program

A number of synthetic results in which the phase velocities were first forward modeled on hypothetical isotropic and orthorhombic materials were gathered. The inversion was then performed on these synthetic, noise-free results. The elastic coefficients for both materials were determined to better than 0.01 % as shown in Tables C.1 and C.2. In the real world, effects such as random electrical noise and transducer misplacement are present. This noise was modeled by the addition of the random noise to the synthetic data. The results of the inversion of this synthetic data are shown in Table C.1 and Tables C.3 to C.12.

For Table C.1, the elastic constants  $\lambda$  and  $\mu$  are Lamé's constants where the compressional and transverse wave velocities are defined by Equations C.4 and C.5 respectively.

$$V_p = \left( \frac{\lambda + 2\mu}{\rho} \right)^{1/2} \quad (\text{C.4})$$

$$V_s = \left( \frac{\mu}{\rho} \right)^{1/2} \quad (\text{C.5})$$

Instead of Lamé's constants, the compressional and transverse wave velocities may also be expressed in terms of the bulk modulus  $k$  and Poisson's ratio  $\sigma$  in Equations C.6 and C.7 respectively.

$$V_p = \left( \frac{3(k - \sigma)}{(1 + \sigma)\rho} \right)^{1/2} \quad (\text{C.6})$$

$$V_s = \left( \frac{3k}{2\rho} \left( \frac{1 - 2\sigma}{1 + \sigma} \right) \right)^{1/2} \quad (\text{C.7})$$

In an orthorhombic medium, the material can be described by 9 independent constants represented by letters  $a$  to  $i$  which are arranged as follows in the 2-dimensional stress-strain tensor:

$$C_{ij} = \begin{bmatrix} a & b & c & 0 & 0 & 0 \\ b & d & e & 0 & 0 & 0 \\ c & e & f & 0 & 0 & 0 \\ 0 & 0 & 0 & g & 0 & 0 \\ 0 & 0 & 0 & 0 & h & 0 \\ 0 & 0 & 0 & 0 & 0 & i \end{bmatrix} \quad (\text{C.8})$$

For the orthorhombic medium, noise was added to the phase velocities and the corresponding elastic constants are calculated and summarized in Tables C.3 to C.12. From analysis of Table C.1 and Tables C.3 to C.12, it was found that for the noise-free case the elastic constants can be determined with an accuracy of better than 0.01 % and that for random errors in velocity of up to 10 % the elastic constants can be determined with average errors of less than 3 %.

This inversion method was then performed on data acquired on an isotropic glass block. There were 131 phase velocities calculated for the glass block which when inverted and the corresponding statistical analysis yielded the following results for the elastic constants:  $\lambda = 19.225 \pm 0.961$  GPa and  $\mu = 32.780 \pm 0.221$  GPa. These elastic constants can be similarly expressed in terms of bulk modulus  $k$  and Poisson's ratio  $\sigma$  as  $41.1 \pm 1.1$  GPa and  $0.184 \pm 0.013$  respectively. These results compare fairly well with the constants of  $\lambda = 22.643 \pm 3.584$  GPa and  $\mu = 30.767 \pm 1.648$  GPa as calculated from direct pulse transmission measurements. For an isotropic medium such as glass, the elastic constants can be calculated with an error of less than 5 %. The inversion converged quickly in the first 20 iterations and then converged much more slowly before stabilizing at 170 iterations (Figure C.1).

The same inversion method was performed on data acquired on an orthorhombic phenolic block. There were 624 phase velocities calculated for the phenolic block which when inverted and the corresponding statistical analysis yielded the elastic constants as seen in Table 2.1. For an orthorhombic medium such as phenolic, the elastic constants can be calculated within an error of 2 % based upon comparison with an ideal case where errors are added. The inversion converged quite quickly in the first 20 iterations and then converged much more slowly before stabilizing at 450 iterations (Figure C.2).

Noise Added	$\lambda$ (GPa)	$\mu$ (GPa)	$\delta\lambda$ (GPa)	$\delta\mu$ (GPa)
0 %	19.22472	32.77794	0.00004	0.00004
1 %	18.954	32.841	0.270	0.061
2 %	18.673	32.905	0.552	0.125
3 %	18.393	32.972	0.832	0.192
4 %	18.107	33.036	1.118	0.256
5 %	17.817	33.103	1.407	0.323
6 %	17.534	33.169	1.691	0.388
7 %	17.271	33.227	1.953	0.447
8 %	16.969	33.300	2.256	0.521
9 %	16.696	33.361	2.528	0.581
10 %	16.435	33.423	2.790	0.643

Table C.1: Inverted elastic constants for an isotropic material as noise is added.

Elastic Constant	Inverted Value (GPa)	Difference from Theoretical Value (Gpa)	Difference from Theoretical Value (%)
a	15.9796	0.0001	0.0006
b	7.16869	0.00001	0.0001
c	7.19554	0.00006	0.0008
d	15.5980	0.00002	0.0001
e	7.31445	0.00006	0.0008
f	11.57869	0.00001	0.00009
g	3.40242	0.00002	0.0006
h	3.00035	0.00004	0.00001
i	3.85498	0.00002	0.0005

Table C.2: Inverted elastic constants for an orthorhombic material with 0 % noise added.

Elastic Constant	Inverted Value (GPa)	Difference from Theoretical Value (Gpa)	Difference from Theoretical Value (%)
a	16.031	0.051	0.3
b	7.191	0.022	0.3
c	7.240	0.044	0.6
d	15.600	0.002	0.01
e	7.278	0.036	0.5
f	11.555	0.024	0.2
g	3.408	0.006	0.2
h	2.993	0.007	0.2
i	3.853	0.002	0.05

Table C.3: Inverted elastic constants for an orthorhombic material with 1 % noise added.

Elastic Constant	Inverted Value (GPa)	Difference from Theoretical Value (Gpa)	Difference from Theoretical Value (%)
a	16.078	0.099	0.6
b	7.213	0.044	0.6
c	7.282	0.087	1.2
d	15.607	0.009	0.06
e	7.246	0.068	0.9
f	11.534	0.045	0.4
g	3.413	0.010	0.3
h	2.985	0.015	0.5
i	3.852	0.003	0.08

Table C.4: Inverted elastic constants for an orthorhombic material with 2 % noise added.

Elastic Constant	Inverted Value (GPa)	Difference from Theoretical Value (Gpa)	Difference from Theoretical Value (%)
a	16.128	0.148	0.9
b	7.241	0.072	1.0
c	7.323	0.128	1.7
d	15.616	0.018	0.1
e	7.211	0.104	1.4
f	11.505	0.073	0.6
g	3.418	0.016	0.5
h	2.979	0.021	0.7
i	3.851	0.004	0.1

Table C.5: Inverted elastic constants for an orthorhombic material with 3 % noise added.

Elastic Constant	Inverted Value (GPa)	Difference from Theoretical Value (Gpa)	Difference from Theoretical Value (%)
a	16.183	0.203	1.3
b	7.262	0.093	1.3
c	7.368	0.173	2.3
d	15.612	0.014	0.1
e	7.173	0.141	2.0
f	11.487	0.092	0.8
g	3.424	0.022	0.6
h	2.970	0.030	1.0
i	3.848	0.007	0.2

Table C.6: Inverted elastic constants for an orthorhombic material with 4 % noise added.

Elastic Constant	Inverted Value (GPa)	Difference from Theoretical Value (Gpa)	Difference from Theoretical Value (%)
a	16.240	0.260	1.6
b	7.288	0.120	1.6
c	7.413	0.217	2.9
d	15.616	0.018	0.1
e	7.138	0.176	2.5
f	11.464	0.115	1.0
g	3.431	0.028	0.8
h	2.961	0.040	1.4
i	3.845	0.010	0.3

Table C.7: Inverted elastic constants for an orthorhombic material with 5 % noise added.

Elastic Constant	Inverted Value (GPa)	Difference from Theoretical Value (Gpa)	Difference from Theoretical Value (%)
a	16.284	0.304	1.9
b	7.313	0.144	2.0
c	7.451	0.255	3.4
d	15.620	0.021	0.1
e	7.103	0.212	3.0
f	11.438	0.141	1.2
g	3.433	0.031	0.9
h	2.958	0.043	1.5
i	3.844	0.011	0.3

Table C.8: Inverted elastic constants for an orthorhombic material with 6 % noise added.

Elastic Constant	Inverted Value (GPa)	Difference from Theoretical Value (Gpa)	Difference from Theoretical Value (%)
a	16.337	0.358	2.2
b	7.335	0.166	2.3
c	7.492	0.296	4.0
d	15.623	0.025	0.2
e	7.068	0.246	3.5
f	11.421	0.158	1.4
g	3.439	0.037	1.1
h	2.946	0.054	1.8
i	3.840	0.015	0.4

Table C.9: Inverted elastic constants for an orthorhombic material with 7 % noise added.



Elastic Constant	Inverted Value (GPa)	Difference from Theoretical Value (Gpa)	Difference from Theoretical Value (%)
a	16.383	0.403	2.5
b	7.359	0.190	2.6
c	7.532	0.337	4.5
d	15.630	0.032	0.2
e	7.034	0.281	4.0
f	11.393	0.186	1.6
g	3.445	0.042	1.2
h	2.943	0.057	1.9
i	3.842	0.013	0.4

Table C.10: Inverted elastic constants for an orthorhombic material with 8 % noise added.

Elastic Constant	Inverted Value (GPa)	Difference from Theoretical Value (Gpa)	Difference from Theoretical Value (%)
a	16.443	0.463	2.8
b	7.386	0.217	2.9
c	7.575	0.380	5.0
d	15.626	0.028	0.2
e	6.993	0.321	4.6
f	11.372	0.207	1.8
g	3.450	0.048	1.4
h	2.931	0.069	2.4
i	3.840	0.015	0.4

Table C.11: Inverted elastic constants for an orthorhombic material with 9 % noise added.

Elastic Constant	Inverted Value (GPa)	Difference from Theoretical Value (Gpa)	Difference from Theoretical Value (%)
a	16.490	0.510	3.1
b	7.411	0.242	3.3
c	7.613	0.418	5.5
d	15.635	0.037	0.2
e	6.957	0.357	5.1
f	11.348	0.230	2.0
g	3.455	0.053	1.5
h	2.921	0.079	2.7
i	3.837	0.018	0.5

Table C.12: Inverted elastic constants for an orthorhombic material with 10 % noise added.

## References

- Kebaili, A., and Schmitt, D. R., 1997. Ultrasonic anisotropic phase velocity determination with the Radon transformation: *J. Acoust. Soc. Am.*, **101**, 3278-3286.
- Press, W. H., Flanner, B. P., Teukolsky, S. A., and Vetterling, W. T., 1989. *Numerical Recipes in C*: Cambridge University Press.
- Robinson, E. A., 1982. Spectral approach to geophysical inversion by Lorentz, Fourier, and Radon transforms: *Proc. of the IEEE*, **70**, 1039-1054.
- Tatham, R. H., 1984. Multidimensional filtering of seismic data: *Proc. of the IEEE*, **72**, 1357-1369.
- Vestrum, R. W., 1994. Group and phase-velocity inversions for the general anisotropic stiffness tensor. M.Sc. thesis. Univ. of Calgary.

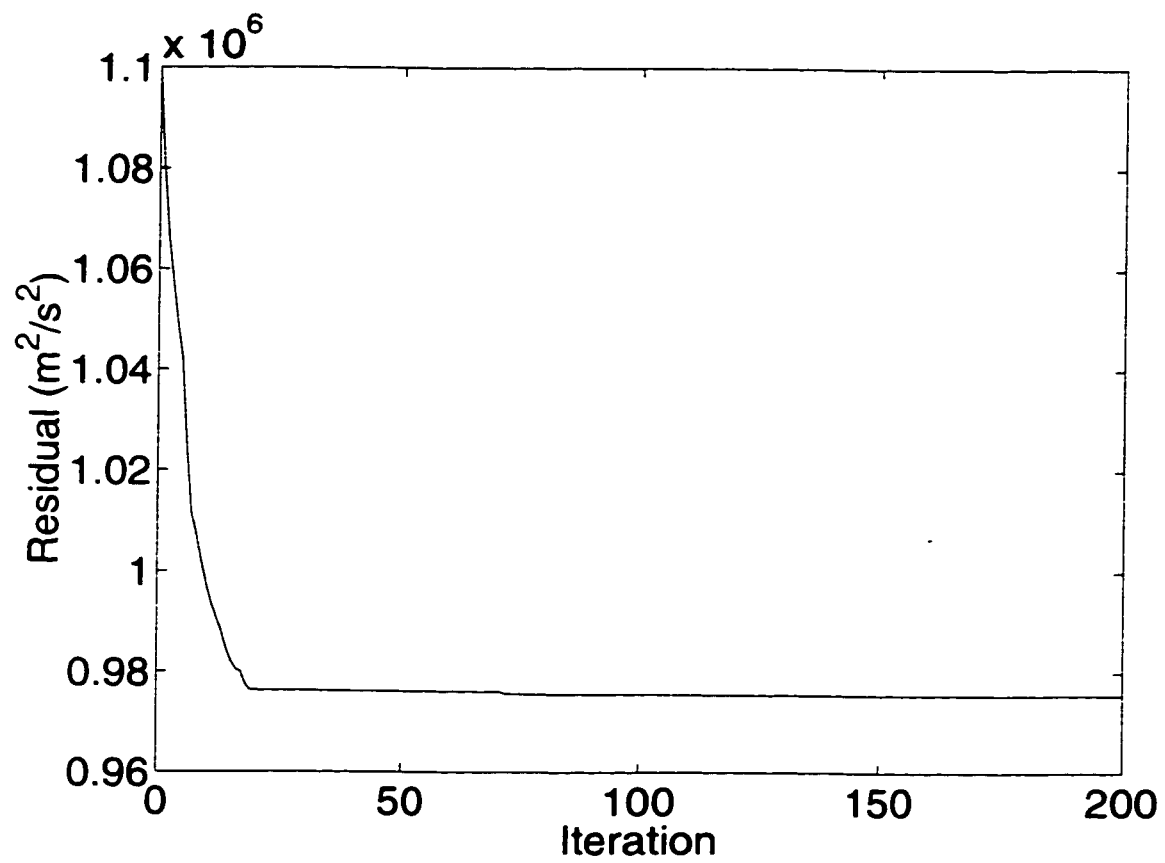


Figure C.1: Inversion residuals on data acquired on a glass block.

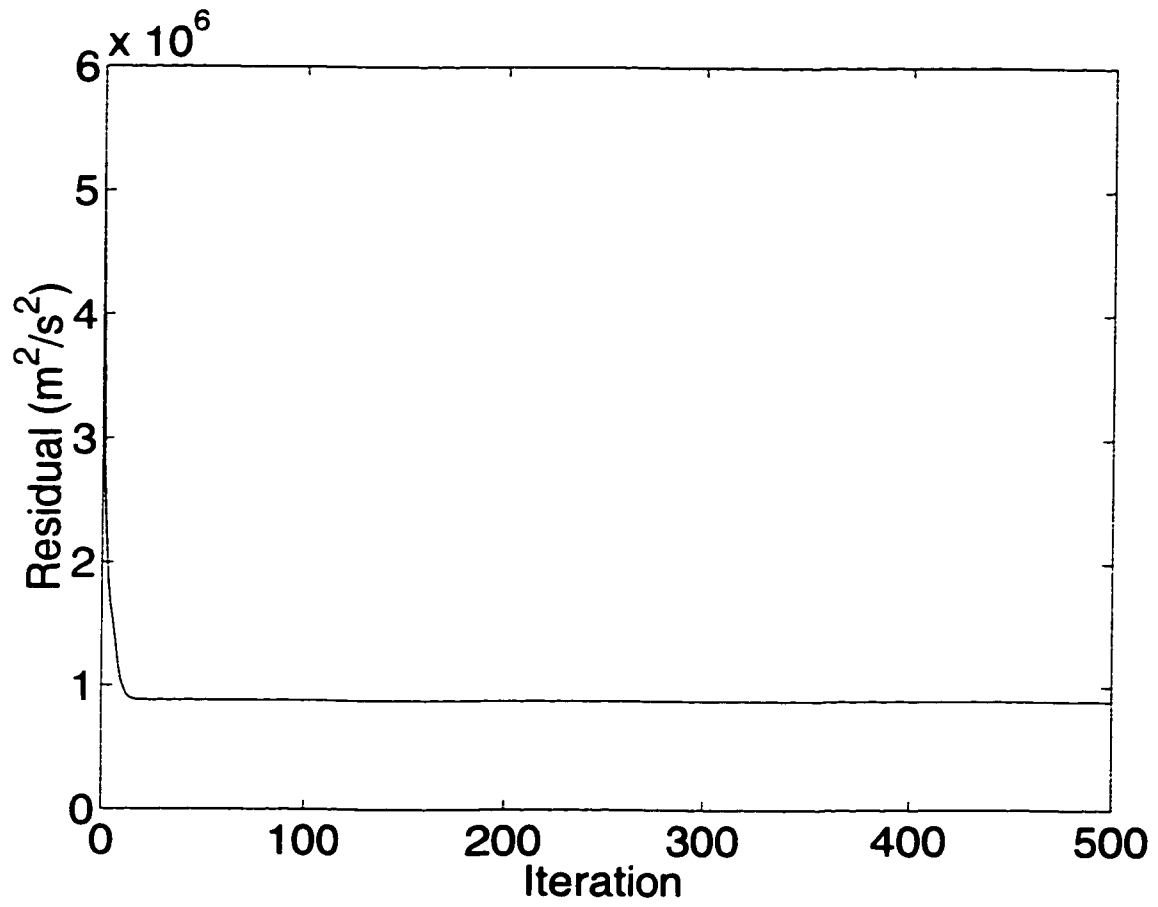


Figure C.2: Inversion residuals on data acquired on a phenolic block.